

# **Micron Diamond Processing of Advanced Ceramics**

**Lounis Ait Ouarab**

A thesis Submitted in Partial Fulfilment of the Requirement of Liverpool John  
Moore's University Faculty of Engineering and Technology for the Degree of Doctor  
of Philosophy

This research programme was carried out in collaboration with Element Six limited

February 2020



## **Abstract**

Grinding is one of the most complex manufacturing processes in industry and understanding its physics is difficult due to the stochastic nature of the process. In this thesis, the influence of the abrasive grit's shape and size on the grinding process is considered. A number of parameters are investigated to set a classification of the abrasives based on the grit's shape and size. These parameters are determined according to image analyses of a large number of abrasive grits. Based on this investigation, the shapes of the abrasive grits could be classified into 21 groups. Typical grit shapes will fall into only few categories dominating the shape population. These dominant shapes are ellipsoid, sphere, quadrilateral frustrum, quadrilateral pyramid and tetrahedron pyramid.

After the abrasives are assessed, a test rig for multiple grit scratching and wire saw cutting rig were developed and a series of multiple grit grinding tests are performed. For this purpose, series of scratching tests have been conducted with five different diamond abrasives. The cutting forces and the acoustic emission were used to characterize the grinding mechanism during this experiment. The machining performances of the abrasive grits are evaluated in consideration of the effect of different grit shapes on the grinding process outputs including force and acoustic emission. The experimental results show a high influence of the proportion of different grit shapes on grinding force: abrasive grits with rounded shape imply high cutting forces, while grits with pyramidal shape generate low cutting forces. Furthermore, based on the proportion of the dominant shapes in an abrasive sample a force model of the cutting force and the shape proportion of the abrasives was established. The force model and the experimental results emphasised the importance of taking into consideration the abrasive's shape as a significant parameter that influences the grinding process.

The online grinding surface creation monitoring was carried out by processing the acoustic emission signals. The acoustic emission signals are analysed in both the time and frequency domains. The results show that the signal feature extraction in the frequency domain gives excellent indication in correlation to the surface creation with different abrasive geometrical characteristics.

## **Publications**

Chen, Y., Chen, X., AIOuarab, L. et al. Morphology Analysis and Characteristics Evaluation of Typical Super Abrasive Grits in Micron Scale. *J. Superhard Mater.* 41, 189–200 (2019)

E. G. Plaza, X. Chen and L. A. Ouarab, "Abrasive Feature Related Acoustic Emission in Grinding" 25th International Conference on Automation and Computing (ICAC), Lancaster, United Kingdom, 2019, pp. 1-6.

E. G. Plaza, X. Chen and L. A. Ouarab, " Grinding Acoustic Emission Features in relation to Abrasive Scratch Characteristics" The 22nd International Symposium on Advances in Abrasive Technology (ISAAT), Shenzhen, China, 2019

## **Acknowledgments**

My sincere gratitude goes to my supervisor Prof. Xun Chen for his continuous support during my PhD. Many thanks for his efforts and patience.

I would like also to thank Dr Tahsin Opoz, Dr Yong Chen, Dr Eustaquio Garcia and Dr Andre Batako for their advice and suggestions.

I wish to thank the manufacturing technical teams in the General Engineering Research Institute for their time, support and advice to accomplish my experiments in a good condition.

I would like to extend my gratitude to all members of the Faculty of Engineering and Technology, the staff, the technician, the secretaries and my fellow students.

I would like to gratefully acknowledge Liverpool John Moores University and Element Six limited for providing full scholarship during my PhD study.

I would like to thank Wayne Leah, Luiz Franca, Amanda McKie and Nastja Macerol staff members of Element Six limited for their contribution to this thesis.

I wish to thank my parents, my brothers, my sisters and my nephews and nieces for their patience, and endless support.

## Nomenclature

Symbol	Description	Units
$V_s$	Wheel speed	m/s
$V_w$	Workpiece speed	mm/min
$D$	Wheel diameter	mm
$a_e$	Cutting depth	$\mu\text{m}$
$r$	Ratio of chip width to average undeformed chip thickness	
$T$	Wheel torque	N.m
$\omega$	Rotation speed	rpm
$F_c$	Cutting force	N
$u$	Specific cutting force	$\text{N}/\text{mm}^2$
$F_n$	Normal force	N
$F_t$	Tangential force	N
$A_{mi}$	Cross section area of the chip	$\text{mm}^2$
$k_c$	Grinding force coefficient	$\text{N}/\text{mm}^2$
$K_{IC}$	Fracture toughness	$\text{MPa}\cdot\text{m}^{1/2}$
$\mu$	Friction coefficient	
$\alpha$	Rake angle	$^\circ$
$\beta$	Friction angle	$^\circ$
$\phi$	Shear angle	$^\circ$
$\sigma_n$	Normal stress	MPa
$k$	Directional stress	MPa
$C$	Material critical strain	
$\delta$	Shear strain	
$\sigma_1$	First principal stress	MPa
$\sigma_c$	Critical tensile strength	MPa
$\tau_{max}$	Maximum shear stress	MPa
$\tau_c$	Critical shear strength	MPa
$a_{gmax}$	Maximum undeformed chip thickness	$\mu\text{m}$
$A$	Contact area	$\text{mm}^2$
$\gamma$	Grain cone apex half angle	$^\circ$
UTS	Ultimate Tensile Strength	MPa
MRR	Material Removal Rate	$\text{mm}^3/\text{s}$
rpm	Round per minute	rpm

# Contents

Abstract	III
Publications	IV
Acknowledgments	V
Nomenclature	VI
Contents	VII
List of Figures	XII
List of Tables	XVI
List of Equations	XVIII
Chapter 1 Introduction	1
1.1 Background	1
1.2 Project's Aim and Objectives	2
1.3 Research methodology	3
1.4 Thesis outline	4
Chapter 2 Literature review	5
2.1 Introduction	5
2.2 Background on grinding process technology	5
2.2.1 Abrasives material	7
2.2.2 Grinding force	8
2.3 Abrasive assessment	11
2.3.1 Based on Occurrence	12

2.3.2	Based on Grit Size	13
2.3.3	Based on Grit Shape	14
2.4	Literature on the mechanism of material removal by abrasive	15
2.4.1	Material removal mechanism in grinding	18
2.5	Abrasive cutting of ductile materials	21
2.5.1	Rubbing Mechanism	21
2.5.2	Ploughing Mechanism	22
2.5.3	Cutting Mechanism	22
2.6	Abrasive cutting of brittle materials	22
2.6.1	Abrasion Mechanisms of Brittle Materials	23
2.6.2	Research Focus in Brittle Region	23
2.6.3	Brittle to ductile transition during ultra-precision grinding	24
2.7	Literature on modelling and Simulation of the Grinding Process	25
2.7.1	Introduction	25
2.7.2	Slip line model	26
2.7.3	Finite element method approach for modelling material removal	28
2.8	Literature on diamond wire saw cutting	35
2.8.1	Principal parameters and properties that affect performance.	36
2.8.2	Diamond wire sawing in monocrystalline silicon ingots.	37
2.8.3	Diamond wire sawing in sapphire	39
2.8.4	Performance similarities of the variants of the process.	40

2.9 AE feature and analysis	41
2.10 Summary and literature key gap	43
Chapter 3 Abrasive grits characterisation and shape classification	44
3.1 Geometrical grit's shape classification approach	44
3.2 Initial work: assessment of loose abrasives	47
3.2.1 Sample preparation process	47
3.2.2 Microscopy Measurement Process	48
3.2.3 Grit shape and size distribution of loose abrasives	49
3.2.4 Aspect ratio	53
3.2.5 Aspect ratio distribution	53
3.3 Assessment of bonded abrasives	56
3.4 Abrasive assessment on diamond wire saw	64
3.5 Summary	66
Chapter 4 Theoretical model of abrasive machining mechanics	67
4.1 Introduction	67
4.2 Grit geometry and workpiece design	67
4.3 Workpiece material and properties	69
4.4 Materials and elastic-plastic behaviour	69
4.5 Simulation approach	70
4.6 Simulation results and discussion	71
4.6.1 Stress and force analysis	71

4.6.2	Analysis of the grit shape influence	79
4.6.3	Proposed grinding force model	80
4.7	Summary	83
Chapter 5	Experimental investigation set up	84
5.1	Introduction	84
5.2	Multiple grits scratching experimental tests	84
5.2.1	Cutting tool	85
5.2.2	Workpiece materials	85
5.2.3	Experimental test set-up and procedure	86
5.2.4	Cutting marks inspection	89
5.2.4.1	Force and acoustic emission during scratching tests	90
5.2.4.2	Scratching marks surface formation inspection	91
5.3	Diamond wire saw cutting test	93
5.4	Summary	97
Chapter 6	Cutting force results and model validation	98
6.1	Introduction	98
6.2	Effect of grit's shape on specific cutting force	98
6.2.1	Sapphire	98
6.2.2	Zirconia	102
6.2.3	Cutting performance comparison on sapphire and zirconia	103
6.2.4	Wire saw cutting	105
6.3	Force model validation: experimental and theoretical results comparison	108

6.4 Summary	112
Chapter 7 Acoustic emission feature extraction and analysis	113
7.1 Introduction	113
7.2 Methodology	113
7.3 Results and discussion	115
7.3.1 Time domain analysis (TDA)	115
7.3.2 Frequency analysis (FFT)	116
7.3.2.1 Analysis of frequency range 0-600 kHz:	118
7.3.2.2 Analysis of frequency range 0-200kHz:	120
7.4 Summary	122
Chapter 8 Conclusion, recommendations and future work	124
8.1 Conclusion	124
8.2 Contribution to knowledge	126
8.3 Recommendations and future work	127
References	128
Appendixes	144

## List of Figures

Figure 1-1: Research methodology .....	3
Figure 2-1: Grinding forces of single grain .....	10
Figure 2-2: SEM image of an abrasive grits .....	11
Figure 2-3: Classification of abrasive materials based on occurrence .....	13
Figure 2-4: Circularity is parameter used to assess the grain shape of abrasives [38] .....	15
Figure 2-5: Three stages of single grit grinding. [41] .....	16
Figure 2-6. Single grit mark profile. [40].....	16
Figure 2-7. Spiral single grit grinding. [42] .....	17
Figure 2-8. Interference pattern on single grit grinding. [42] .....	17
Figure 2-9: Basic material removal mode for grinding.....	18
Figure 2-10: Surface grinding model [2] .....	19
Figure 2-11: (a) Side view of the initial impression, (b) Top view of the initial impression and (c) Propagation of the crack below the impression after the indentation is loaded [47] .....	23
Figure 2-12: Slip line abrasion mechanism [63] .....	26
Figure 2-13. Slip line field for mild wear [64].....	28
Figure 2-14: Geometric model with mesh for FEA [66] .....	29
Figure 2-15. Tangential force as a function for wheel speed. [66] .....	30
Figure 2-16. Tangential force as a function of feed speed. [66] .....	30
Figure 2-17. Tangential force as a function of grinding depth. [66].....	30
Figure 2-18. Ductile and Brittle fracture modes on grinding. [67].....	31

Figure 2-19. Equivalent Plastic Strain Criterion. [67] .....	32
Figure 2-20. Single grain grinding model [67] .....	33
Figure 2-21. Finite element model for single grain grinding [67] .....	33
Figure 2-22. FEA results with different fracture criteria [67].....	34
Figure 2-23. Surface morphology at different grinding depths. [67].....	35
Figure 2-24. Sapphire ingot wire cut [70].....	36
Figure 2-25. SEM photograph of a cutting wire .....	38
Figure 2-26. Crystallographic directions of sapphire [75].....	40
Figure 3-1: Leica microscope .....	48
Figure 3-2: Leica images (a) synthesized M2030, (b) synthesized M 4060 (c) CDA M1530, (d) MDA M0510, (e) MDA M1225, (f) MDA B, (g) MDA A, (h) MDA C, (i) PD M0510.....	49
Figure 3-3: Grit shape and size distribution for nine diamond abrasives samples .....	52
Figure 3-4: Major and minor axes (dashed lines), length (red) and width (blue).....	53
Figure 3-5: Aspect ratio distribution for the group of nine samples of loose abrasives .....	55
Figure 3-6: Average diameter distribution for the group of nine samples of loose abrasives .....	55
Figure 3-7: Cutting tool with bonded abrasives.....	57
Figure 3-8: Shape distribution of five different abrasives bonded to cutting tools.....	62
Figure 3-9: Dominant shapes in the five abrasives samples .....	63
Figure 3-10: Shape distribution on the three diamond wires .....	65
Figure 4-1: Stress-strain curve for brittle material illustrating elastic plastic behaviour and brittle fracture .....	70
Figure 4-2: Workpiece and grit body (Pyramidal shape) modelled in SolidWorks.....	71

Figure 4-3: Stress distribution for different grit shapes .....	75
Figure 4-4: The results for the spherical shape .....	76
Figure 4-5: The results for the pyramidal shape .....	77
Figure 4-6: The results for the truncated shape.....	78
Figure 4-7: Effect of the grit shape on force level .....	80
Figure 4-8: Force vs cutting depth regression model.....	82
Figure 5-1: Cutting tool.....	85
Figure 5-2: Workpiece material: (a) zirconia and (b) sapphire.....	86
Figure 5-3: XR 610 CNC machine .....	88
Figure 5-4: Experimental test set up .....	88
Figure 5-5: cutting marks inspection: depth and width measurements.....	90
Figure 5-6: cutting marks inspection: force and acoustic emission .....	91
Figure 5-7: SEM images of scratching marks obtained in Sapphire cutting .....	92
Figure 5-8: Conceptual design of the diamond wire saw rig .....	94
Figure 5-9: Diamond wire saw test rig.....	95
Figure 5-10: Sapphire workpiece bar with wire cut kerf loss .....	96
Figure 6-1: Measured specific force on multiple grit cutting test. Workpiece: sapphire.....	99
Figure 6-2: SEM images of the abrasive grits before and after scratching test .....	100
Figure 6-3: Measured specific force on multiple grit cutting test. Workpiece: zirconia .....	102
Figure 6-4: Cutting force comparison for Sapphire and Zirconia.....	104
Figure 6-5: Grits engagement in sapphire and zirconia materials .....	104

Figure 6-6: Measured forces during the wire saw cutting tests .....	106
Figure 6-7: SEM images of the wire wear after the cutting tests.....	107
Figure 6-8: Measured and modelled force in the case of cutting with the abrasive A.....	109
Figure 6-9: Measured and modelled force in the case of cutting with the abrasive B.....	110
Figure 6-10: Measured and modelled force in the case of cutting with the abrasive C.....	110
Figure 6-11: Measured and modelled force in the case of cutting with the abrasive D.....	111
Figure 6-12: Measured and modelled force in the case of cutting with the abrasive E.....	111
Figure 6-13: Comparison of the specific force at 1 $\mu\text{m}$ depth for the model and the experiment results .....	112
Figure 7-1: AE signal feature extraction methodology.....	114
Figure 7-2: Estimated values vs experimental values of the parameter W/D for TDA method. a) Sapphire, b) Zirconia.....	116
Figure 7-3: Frequency ranges for AE signal analysis .....	118
Figure 7-4: Estimated values vs experimental values of the parameter W/D for FFT method in 0-600 kHz. a) Sapphire, b) Zirconia.....	120
Figure 7-5: Estimated values vs experimental values of the parameter W/D for FFT method in 0-200 kHz. a) Sapphire. b) Zirconia.....	122

## List of Tables

Table 2-1: Categorization of abrasive grits depending on their sizes, using designation number system [32].....	14
Table 2-2: Mechanical properties of the grinding system [66].....	29
Table 3-1: Classification shape criteria.....	45
Table 3-2: Grit's shape classification .....	46
Table 3-3: Description of statistic measurements associated to the distribution of Aspect Ratio .....	56
Table 3-4: Classification of the abrasive shapes into three main dominant shapes and their proportions .....	64
Table 3-5: Geometrical grit shapes proportion in each wire and the associated total measured force .....	64
Table 4-1: Workpiece and grit shapes modelled in SolidWorks .....	68
Table 4-2: Material properties.....	69
Table 4-3: Applied cutting depth for each of the three shapes configuration of the simulation.....	71
Table 4-4: Force simulation results.....	79
Table 5-1: Material properties.....	86
Table 5-2: Grinding test parameters.....	89
Table 5-3: Diamond wire cutting test conditions.....	96
Table 6-1: Geometrical grit shapes proportion in each abrasive and the associated total measured force. Workpiece: sapphire .....	101
Table 6-2: Geometrical grit shapes proportion in each abrasive and the associated total measured force. Workpiece: zirconia.....	103

Table 6-3: Geometrical grit shapes proportion in each wire and the associated total measured force  
..... 106

Table 7-1: statistical feature extraction of acoustic emission signal..... 115

Table 7-2: Significant parameters of the sapphire and zirconia predictive models for the TDA method  
..... 116

Table 7-3: Significant parameters of the sapphire and zirconia predictive models for the FFT method  
in 0-600 kHz..... 119

Table 7-4: Significant parameters of the sapphire and zirconia predictive models for the FFT method  
in 0-200 kHz..... 121

## List of Equations

(2-1).....	9
(2-2).....	9
(2-3).....	9
(2-4).....	9
(2-5).....	9
(2-6).....	10
(2-7).....	10
( 2-8).....	18
( 2-9).....	19
( 2-10).....	19
( 2-11).....	20
(2-12).....	20
(2-13).....	20
(2-14).....	20
(2-15).....	21
(2-16).....	27
(2-17).....	27
(2-18).....	32
(2-19).....	32
(2-20).....	38

(2-21).....38

(3-1).....54

(3-2).....54

(3-3).....54

(3-4).....54

(4-1).....72

(4-2).....81

(4-3).....81

(6-1).....108

(6-2).....108

(7-1).....113

(7-2).....117

# Chapter 1 Introduction

## 1.1 Background

Grinding is an abrasion process in which irregularly shaped abrasive grits on a wheel surface penetrate into a workpiece and remove the material away in the form of minute chips. It is the one of the manufacturing processes which is utilized for a number of applications and can be employed to different workpiece materials [1]. Abrasive machining is used in several forms, from the common shop level manual grinding, industrial grinding, to lapping, buffing, and polishing [2]. The abrasive machining process is not only useful for achieving high surface quality of a workpiece as a finishing process but also for removal of material at a higher rate. The required properties of a grinding tool are defined before grinding by the capabilities of the machine tool and properties of the workpiece. Grinding wheels are mostly used for this purpose which are designed for specific machining operations as a complex high precision tool [3]. From simple and efficient material removal to the precision surface finishing of high responsibility mobile parts, grinding processes are at the core of manufacturing. However, this process is not without flaws; abrasive dullness, surface burns, excessive cutting depth, or even abrasive wheel breaking are situations that must be prevented to avoid scrapping a workpiece or putting the operator at risk [2]. Therefore, it is important to understand how grinding works, which are the most important parameters to achieve a successful process, and how the part quality is affected by the variations of the process. The grinding process has extended to many industries for its versatility. It is used in the metal mechanics industry for the production of precision parts; it is used in the aerospace industry to achieve smooth moving assemblies; the mining industry uses this process for the cutting of very demanding materials; the semiconductors industry uses this process to achieve dimensional accuracy of silicon wafer for microelectronics circuits. The shape of the abrasives has an important effect on the grinding process outcome parameters. This thesis is studying the abrasives shape and its influence on the grinding operations.

## **1.2 Project's Aim and Objectives**

### **Aim:**

The main aim of the thesis is to determine the influence of the abrasive's shape on the grinding process. More specifically, how the shape properties of the abrasives affect the performances of the grinding process operations

### **Objectives**

This research work is in collaboration with Element Six Limited and will consist of the following objectives:

- Refining the definition of shape and size of the abrasives in order to surround complex shapes that are difficult to characterise
- Grit's shape classification through image analysis
- Modelling different abrasive's shapes and performing simulations to evaluate the influence of grit's shape on grinding force and stress.
- Developing a grinding test rig to perform multiple scratching tests and understanding the cutting behaviour of diamond abrasives and material removal characteristics under various operating conditions.
- Developing a wire saw test rig to evaluate the cutting forces on diamond wire saw cutting.
- Using of acoustic techniques for monitoring the grinding process in relation to surface creation.

### 1.3 Research methodology

Figure 1-1 shows the diagram representing the methodology of this study. The chart has been drawn to explain the chapter's sequences and to explain how the entire thesis has been developed and managed from the literature review stage up to the final results and conclusion.

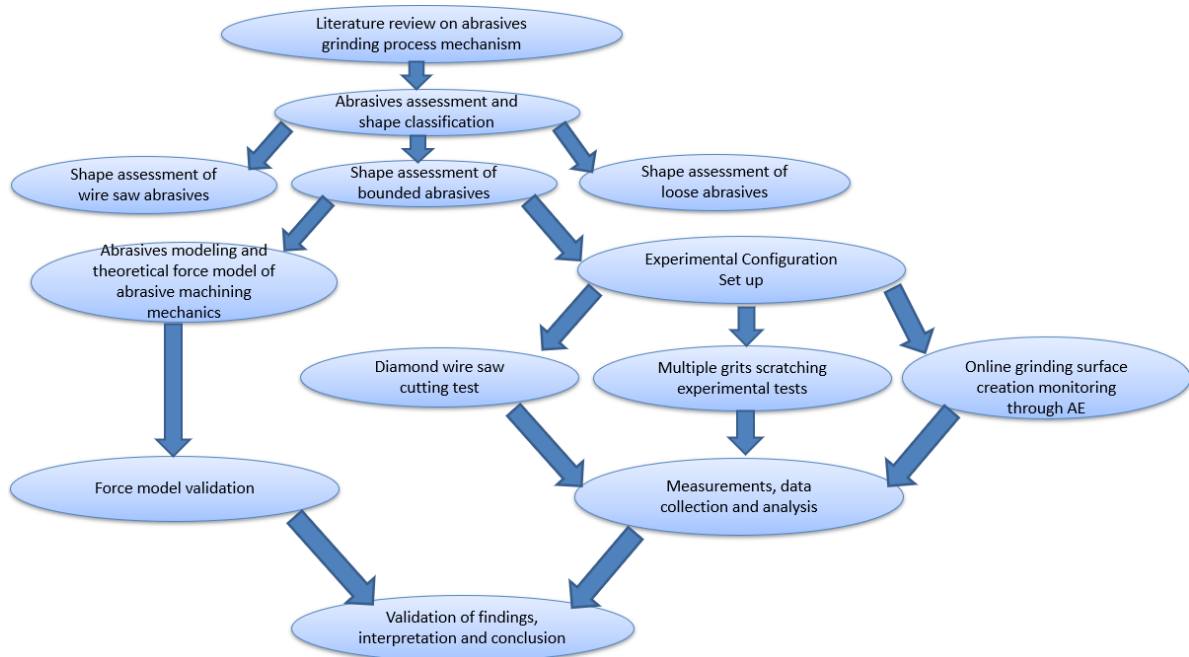


Figure 1-1: Research methodology

## **1.4 Thesis outline**

The thesis is structured in eight chapters including the introduction chapter.

Chapter 2 outline the fundamentals for grinding process, the importance of the grinding tool and its required characteristics. It contains as well a literature review on mechanics of the process are covered.

In chapter 3, abrasive grits characterisation and shape classification of the abrasive grits was reported. In this chapter, loose diamond abrasives, bonded diamond abrasives and diamond abrasives on wire saw were assessed.

Chapter 4 describes a theoretical model for abrasive machining process and a simulation procedure for the cutting force calculation.

Chapter 5 describes the materials and the experimental investigation including experimental set-up, workpiece definition and process monitoring system.

Chapter 6 presents the results of the experimental tests and analysis on the effect of the grit shape's on the cutting forces.

Chapter 7 covers the use of acoustic emission techniques for monitoring the surface creation during the grinding process. And finally, chapter 8 presenting the conclusions and suggestions for future work.

## **Chapter 2 Literature review**

### **2.1 Introduction**

A grinding process is classified as a machining process. The machining process requires removing material from a blank of material until reaching the required geometry and accuracy. The different grinding processes available are an essential part of the success of many industries. From simple and efficient material removal to the precision surface finishing of high responsibility mobile parts, grinding processes are at the core of the manufacture. However, this process is not without flaws; abrasive dullness, surface burns, excessive cutting depth, or even abrasive wheel breaking are situations that must be prevented to avoid scrapping a workpiece or putting the operator at risk [4]. Therefore, is important to understand how grinding works, which are the most important parameters to achieve a successful process, and how the part is affected by the variations of the process.

In this work, the most important process parameters and considerations for grinding are covered from a literature review perspective. First the fundamentals for grinding manufacture are established, secondly, the importance of the grinding tool and its required characteristics are reviewed. After that, the mechanics of the process are covered. Going in-depth into the process, a few models for the grinding process that have been developed in academic works are mentioned, following the topic of the mechanics of the process. Computer simulation studies of the process are also mentioned as an important tool for understating grinding. More advanced modelling and simulation of the process follows, where the process is modelled for its interactions of single and multiple abrasives. Finally, this work covers the use of acoustic techniques used for monitoring the grinding process.

### **2.2 Background on grinding process technology**

The grinding process is one of the abrasive machining processes, commonly used for finishing operations to give dimensional accuracy or a high surface roughness to the part [5]. In addition, it is used to remove material on hard materials, which are not efficient to work with the cutting machining processes.

An abrasive is used as a machining tool for the grinding process. The abrasives characteristics will be later described. Some variants of the process are lapping, buffing, and polishing, and for each different application, the abrasive is different [2]. Other common applications are

finishing of ceramic materials, cutting materials to length, removing weld excess and deburring of parts, and surface cleaning.

The applications for grinding include surface grinding, cylindrical grinding, internal grinding, creep-feed grinding, and heavy stock removal [2]. Each one has its unique perks to consider.

Surface grinding is the most common industrial operation and has the objective of obtaining flat surfaces with low roughness. The workpiece is clamped or held to the machine worktable, while the abrasive travels in traverse or plunge motion to achieve flat surfaces and grooves.

Cylindrical grinding or centre-type grinding uses a spinning abrasive wheel and a spinning work part, which spin at different speeds. The abrasive can move in a transverse or plunge type of grinding. In the traverse grinding, the abrasive moves in a direction along the part and the plunge grinding is when the abrasive moves radially towards the part.

In internal grinding, an abrasive wheel is rotated at high speeds inside a work part. It can traverse or plunge inside the part. The workpiece either can rotate or be fixed in place.

Creep-feed grinding is used for material removal. This operation can have a cut depth of up to 6 mm at a time. However, this process requires a lot of power, a very stiff and resistant machine, high damping capacity, and ample capacity for grinding fluids.

Heavy stock removal, as its name implies, is also meant for material removal. In this variant, the process parameters are increased, to compete with the performance of process such as milling and turning.

It is also important to note, that the grinding process produces a high amount of friction, and therefore, an important increase in temperature. This needs to be considered for the effect it can have on the workpiece material properties. Grinding fluids are usually water-based emulsions for general grinding process, and oil-based for heavy and specialized variants. Those fluids can be applied by flood, stream, or mist. It will be important to note that specialized nozzles must be used, to direct the fluid directly to the grinding surface. Otherwise, the fluid might not reach its destination because of the airstream on the periphery of the high-speed abrasive and part motion.

Since grinding is usually used to achieve high dimensional accuracy of parts, uniform work part temperature must be maintained [1]. The fluid objectives are to reduce the temperature of both the workpiece and the abrasive, lubricate the work area to increase efficiency, and remove the residues that might interfere with the process, thus increasing the quality of the surface finish.

Grinding chatter also needs to be reduced to achieve the best possible surface finish. Chatter

can be attributed to bearing condition on the machine spindles, non-uniformities on the abrasive tool, uneven abrasive wear or an unbalanced abrasive wheel. Chatter marks can be found on the workpiece under these conditions and will negatively affect the part [2].

### **2.2.1 Abrasives material**

As mentioned before, an abrasive tool is required for grinding. An abrasive is a small and hard grit, with sharp edges and irregular shapes. The friction between the abrasive and the workpiece material will cause chipping and material removal [2]. The most common industrial abrasives used are:

- Aluminium oxide ( $\text{Al}_2\text{O}_3$ ). Used on carbon steels and ferrous alloys.
- Silicon Carbide (SiC). For non-ferrous metals, cast irons and ceramics.
- Cubic boron nitride (CBN). For grinding steels and cast irons with hardness superior to 50 HRC.
- Diamond. For ceramics, carbides and some hardened steels.

Those materials are used because they are harder than common cutting materials, and because of their friability. Friability is the ability of a grit to fracture into smaller pieces, leaving a smaller grit with sharp edges, which is essential for material removal. High material friability indicates that low stress is required to fracture the grit. A material with a shape and size that allows for easy fracture leaving a small and sharp residue is also considered as highly friable. Abrasives materials are also selected based on their compatibility with the workpiece material. Using diamond on steel can be detrimental to the abrasive tool life because the increased temperature can cause the diamond to dissolve into the steel. The less reactive the materials are, the better the process performance is. The grinding performance also effected by the ability to produce efficient cutting edges when the abrasive grits are dressed [6].

The abrasive tools are usually identified for their grit number. This indicates the general size of the abrasive grits in the tool, the smaller the grit size, the larger the grit number. A 500-grit size is made of fine grits, for smooth surface finishes.

The most common abrasive tool is the grinding wheel, which is made of abrasives bonded together onto a wheel shape. The bonding material provides adhesion to the abrasive grits, and causes porosity on the wheel. Porosity provides clearance for the material removed, room for cooling, and an irregular surface of the abrasive tool necessary for material removal. Without porosity, the tool would be dense and solid, without room for chips to form.

Abrasive tools are usually identified with a code, provided by the manufacturer and standardized, to identify the type of abrasive, grain size, grade, structure and bond type.

The bonding material also plays an important role in the process. The most common bonding materials are resinoids, reinforced wheels, thermoplastics, rubber and metal [2].

The selection of the appropriate abrasives for different grinding operations was widely investigated in the literature. Jackson and Mills [6] reported the effect of material removal rate on the choice of abrasives in terms of wear and power consumption during grinding. A selecting of new abrasive materials based on the size and shape of abrasives, and the grinding operations for a particular application was suggested. Hitchiner et al. [7] studied the influence of grit size distribution and toughness of CBN abrasives on the standard and newly developed vitrified bond systems. It was found that tougher grits require stronger bonds to attain economic benefit. Maity and Chakraborty [8] applied fuzzy technique for order performance by similarity to ideal solution (TOPSIS) for grinding wheel abrasive material selection while considering different fuzzy evaluation criteria. A complete ranking of the most suitable abrasive material for a grinding wheel was achieved.

### **2.2.2 Grinding force**

Grinding forces are the main factor which affect the grinding system deformation and generates heat and also the vibrations by grinding. These forces directly affect the final quality of surface and accuracy of dimensions in workpiece. The grinding forces are linked to grinding parameters and are the main factor to evaluate the materials grinding performances [9]. Many research and studies have conducted on grinding forces with theoretical and experimental analysis. Jing et al. [10] reported a model of improved blister field for the scratch processes and a model of expanding cylindrical cavity for the estimation of size of plastic zone that surrounds the scratch grooves. Li et al. [11] developed a model of grinding forces for silicon based ceramics with the focus on plastic flow, rubbing and removal of brittle fracture method. Shavva et al. [12] developed a method of cutting forces calculation for diamond grinding of brittle materials in which the cutting forces were calculated as fracture, normal and tangential forces acting on the single grain. Chen [13] considered a single grit as a cutting tool and reported that the average cutting force in a single grit is proportional to the section area of the removed chip.

$$F_{ti} = k_c A_{mi} \quad (2-1)$$

Where  $F_{ti}$  is the tangential force on the grit,  $A_{mi}$  cross section area of the chip and  $k_c$  is a grinding force coefficient and is given by Ono [14] as an empirical expression as:

$$k_c = k_0 A_{mi}^{-\eta} \quad (2-2)$$

Where  $k_0$  and  $\eta$  are constants. By the summation of the forces generated by each individual grit, the total tangential force could be expressed as:

$$F_t = \sum_i F_{ti} = \sum_i k_0 A_{mi}^{1-\eta} \quad (2-3)$$

Lijun Li [15] reported a prediction model of the cutting force as represented the friction force and deforming force. The deforming force and friction force in Figure 2-1 as a major research objective in prediction model is as follows:

$$F_n = F_{nc} + F_{ns} \quad (2-4)$$

$$F_t = F_{tc} + F_{ts} \quad (2-5)$$

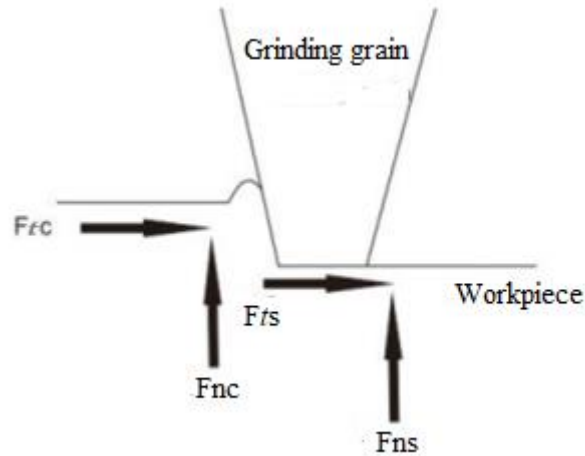


Figure 2-1: Grinding forces of single grain

Where

$F_n$  = Normal force

$F_t$  = Tangential force

$F_{nc}$  = Chip deformation normal force

$F_{ns}$  = Frictional normal force

$F_{tc}$  = Chip deformation tangential force

$F_{ts}$  = Frictional tangential force

Malkin [16] reported the normal and tangential force as:

$$F_n = K * (\text{Material Removal Rate}) + Ap \tag{2-6}$$

$$F_t = \frac{\pi K}{4 \tan \gamma} * (\text{Material Removal Rate}) + \mu Ap \tag{2-7}$$

Where:

$K$  = Unit cutting force

$A$  = Contact area

$p$  = Unit pressure

$\gamma$  = grain cone apex half angle

$\mu$  = Coefficient of friction

## 2.3 Abrasive assessment

The grit characterisation is the measurement of grit properties, which are key factors for its performance. Grits used as abrasives must possess suitable size and shape attributes that improve material removal [17]. Furthermore, a single parameter is insufficient to describe the geometrical qualities of such grits. Discussions about geometrical properties lead to the conclusion that a single parameter only characterises a limited part of grits' geometrical qualities. For an entire description of grit shape, an infinite number of parameters are required. However, in practice only a few parameters are useful [18]. Some of those parameters are diameter (minimum, median and maximum), aspect ratio, circularity etc. These parameters represent a basis for characterization and quality control of diamond grit shape and size used in the fabrication of grinding wheels [19]. Although, the shape of the abrasive grits has a large impact on the grain strength, grinding performance, and packing characteristics that impact wheel formation and manufacture [20], few attempts have been made to limit the gap between the description of real grit shape and the assumptions (relating to shape) employed in the development of abrasion models. In fact, grit shapes consist of irregular and multiple geometries and often a simplified description as conical, elliptical, or spherical is used in wheel modelling applications [21]. Figure 2-2 shows an SEM image of diamond abrasive grits. It is clear from the image that the actual shape of the grains is more complex than generally assumed. It comes into sight that one of the major reasons for this deficiency derives from the difficulties associated with measuring and quantifying the abrasive grits' shape.

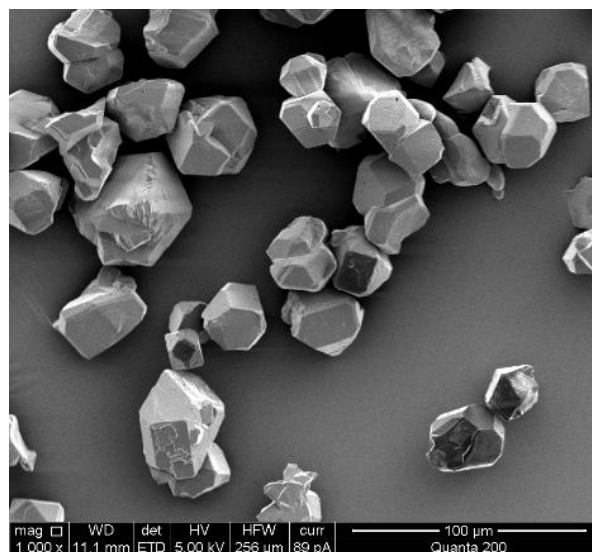


Figure 2-2: SEM image of an abrasive grits

Grits suitable for use as abrasives must be significantly harder (by at least 20%) than the workpiece material [22], and they must possess size and shape attributes that improve material removal [23]. Abrasives can be basically characterised over the material hardness, grit shape, material density, material diameter [24]. The hardness of the abrasive material is mostly compared with the hardness of the work piece; it requires a difference between the hardness of the two materials in order to be abraded. Hardness of the abrasive materials is commonly expressed in Mohs Scale which gives ratings for the materials according to their hardness. Toughness of the material also has to be taken into consideration as the material should have strength enough to withstand the shock when it is rubbed over another metal or workpiece without failing or breaking.

The abrasive machining process utilises abrasive grits as a cutting tool to remove materials from workpiece. Characterisation of the morphology of the grits (shape and size) is of great utility to analyse and improve the grinding performances. In the literature, the main previous researches regarding the grit characterisation consider the shape of the grits to be as a single particular shape: sphere or ellipsoid [25] [26], pyramid with a certain angle or cone shape [27]. Moreover, many abrasive shape models were built based on the aforementioned geometries. While in fact, the grits shapes present a large variety of geometries and are arbitrarily distributed over the abrasive tool. Hence, a precise shape and size description of the grits at a micron level is required in order to better evaluate its influence on the grinding process. The shape of the abrasive is also a critical parameter which affects the functionality of an abrasive. Grits with angular shape are much faster and sharper in grinding or polishing whereas rounded grits are slower in processing [28]. Grit size distribution is a very important parameter of abrasives as it defines the sharpness, working speed and the amount removed from the workpiece. Generally, abrasives with larger grit size will remove large metal pieces from the workpiece and vice versa. In abrasives of crystalline form, distribution of grains and grain sizes also affect the performance of abrasive material [29].

### **2.3.1 Based on Occurrence**

Abrasives are classified into two major categories as naturally existing and synthetic. Some of the naturally existing abrasives are diamonds, talc, sandstone, quartz, corundum etc. In the current context, synthetic abrasives are widely used due to their advanced performance compared to natural abrasives [30].

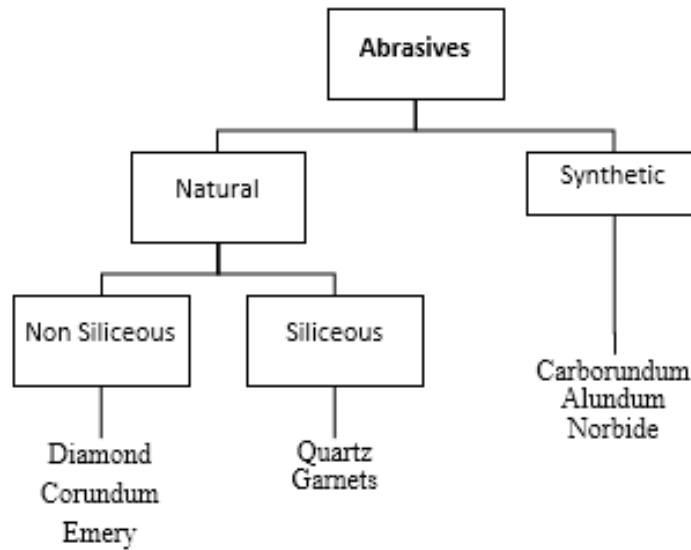


Figure 2-3: Classification of abrasive materials based on occurrence

### 2.3.2 Based on Grit Size

Abrasive grit size is a critical factor in grinding wheel design and usage. Grit size is related to the average diameter of the abrasive grits bonded to the grinding tool. The average diameter of the abrasive grits is determined using a sieving process. Sieving is a regular process performed either by manual work or by machine to separate abrasive grits from uniform sieves in different mesh size grades. Coarse abrasive grits are definitely classified in terms of sieving mesh size. Finer or powder grits are classified by sedimentation process in terms of multiple national and international standards, such as ANSI, FEPA, FEPA, GB/T ISO, etc. [31].

Grit size is important because the requirements of both the production process and final component are commanded by the condition of the abrasives and the grinding parameters employed. The fraction of the abrasive grain size that penetrates and cuts the material during a grind is small, but proportionately the material removed is linked to the cut depth of the abrasive grain. Therefore, larger abrasive grains cut deeper and attain higher material removal rates for a given workpiece material and set of machining parameters.

Various standards exist to classify abrasive on the dimensional basis. Normally, abrasive grits range from small to large. Large grits are identified as coarse and smaller grits as fine.

In order to categorize abrasive types under grit sizes, a grit designation number system is used (Table 2-1) [32].

Table 2-1: Categorization of abrasive grits depending on their sizes, using designation number system [32]

<i>Designation number</i>	<i>Fineness</i>	<i>Application</i>
12,16,20	<i>super coarse</i>	<i>For extra deep and coarse cutting</i>
24,30,36	<i>extra coarse</i>	<i>For coarse cutting</i>
40,50,60	<i>coarse</i>	<i>For cutting and sanding uneven surfaces</i>
80,100	<i>medium</i>	<i>For sanding marks and unevenness</i>
120,150,180	<i>fine</i>	<i>For fine-sanding, and use between and after final surface treatment</i>
220,240,280,320	<i>extra fine</i>	<i>For final sanding where there is a particular requirement for a smooth surface</i>
400,500,600	<i>super fine</i>	<i>For final sanding where there is a particular requirement for an extra smooth surface</i>
800, 1200 and finer	<i>ultra-fine</i>	<i>For final sanding where there is a particular requirement for and extremely smooth surface</i>

### 2.3.3 Based on Grit Shape

The shape of the abrasive grits has a large impact on the grit strength, grinding performance, and packing characteristics that affect wheel formation and manufacture. Grits can be found in many different shapes, which results in different abrasion mechanisms. The final surface finish of a material that has undergone abrasion is highly dependent on the grit shape. However, the problem of shape assessment is one of the most difficult problems in powder technology. The number of approaches to assess the shape of grits usually utilised approaches such as the measurement of circularity, Feret elongation ratio, or aspect ratio [33]. Head and Harr [34] reported a degree of roundness as a shape parameter for characterising grits in relation to erosion. It is based on the selection and determination of the protrusion radii. Petasyuk [35] utilised a method of geometric shape identification of the projection of abrasive grits based on a system-analogue approach. For analogues the two-dimensional geometric figures, i.e. circles, ellipses, triangles, canonical forms of tetragons, regular pentagons, hexagons, and octagons have been taken. Verspui et al. [36] developed boundary angularity methods and measured the curvature as a function of displacement along the grit boundary. The peaks representing the corners of the grits profile were sorted to form the mean angle of the grit. Cone-fit analysis (CFA) is another technique was developed for a better understanding of the nature of grit shape [37]. This technique implicated estimating two-dimensional grits outlines by a series of cones.

The ratio of two grit areas, namely groove area, and projected penetration area was utilised as a measure of grit angularity. In [38], the circularity is used to characterize the abrasive grits shapes and it was defined as it is shown in Figure 2-4. When the circularity decreases, grit becomes closer to sharp, long shape. Associated with other parameters, grit shape is a main factor for determining abrasive model.

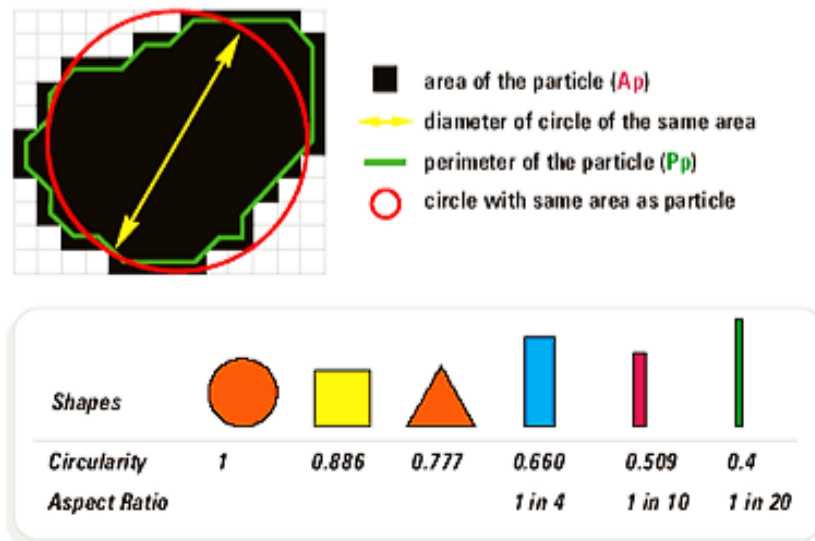


Figure 2-4: Circularity is parameter used to assess the grain shape of abrasives [38]

## 2.4 Literature on the mechanism of material removal by abrasive

Grinding process is the mechanism of material removal from a workpiece material. The mechanics involved in the process includes three main stages: rubbing, ploughing and chip formation as it was described by Hahn [39]. Rubbing has no effect on the grinding process because the abrasive grit only deforms elastically the material surface. Ploughing occurs when plastic deformation is induced on the material, and chip formation is when the fracture occurs [40]. The three stages occur as the cutting depth increases; shown in Figure 2-5, rubbing occurs between cutting depths  $\delta_r < \delta_p$ ; ploughing in depths  $\delta_p < \delta_c$ ; and cutting at depths major than  $\delta_c$ , where  $\delta_r$ ,  $\delta_p$  and  $\delta_c$  are critical rubbing, ploughing and cutting depths. It can be observed that during ploughing, the material is deformed plastically and displaced to the front and sides. The deformed material forms a ploughed lip that is then cut when chip removal occurs.

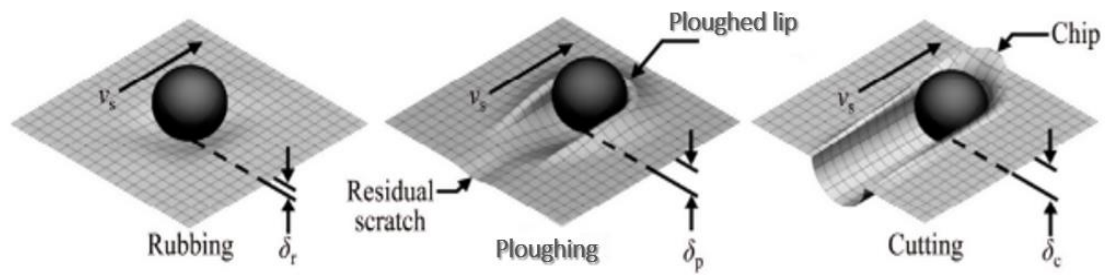


Figure 2-5: Three stages of single grit grinding. [41]

Single grit experimental set-ups have been tested to observe this effect on the workpiece material. Using a high-speed spindle (over 20,000 rpm) and steel wheel of 34.8 mm diameter with a single diamond abrasive on it, tests were conducted. The workpiece material ground was Inconel 718 and force was measured on it using a 3-axis force sensor. Several tests were made on the material, measuring force and observing the effect on the material. Figure 2-6 shows the obtained profiles after grinding tests. It can be observed that the material has piled up around the edges of the ground groove, consistent with the plastic deformation and material displacement observed in the ploughing stage [40].

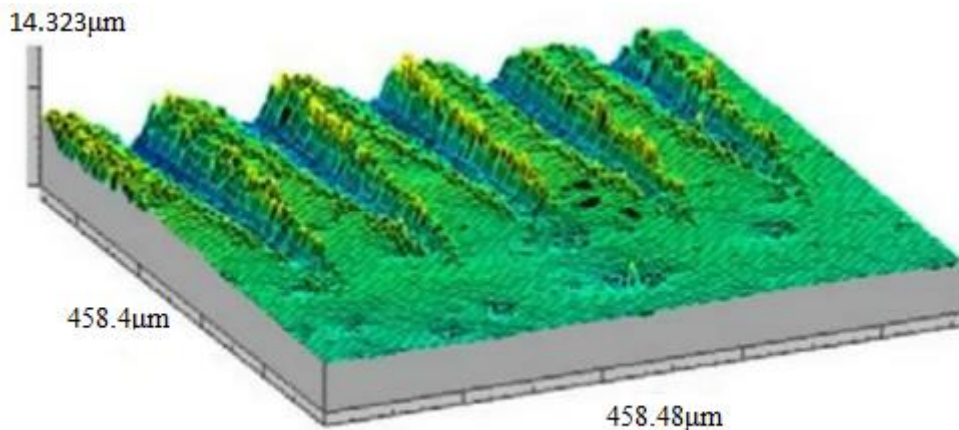


Figure 2-6. Single grit mark profile. [40]

A similar study was conducted in [41], where a single grit grinding experiment was designed and simulated using FEA. The workpiece material was martensitic stainless steel, and the abrasive used was diamond. Force and temperatures were measured in the study mentioned. The result of this work confirms a linear relationship between normal force and tangential force with cutting speed and grinding depth. Finally, it was found that the maximum stress and strain

in the workpiece material is located under the grit tip.

To observe the traces caused by other abrasives, a single grit experiment was designed with a spiral pattern. The setup proposed in [42] includes an additional motion direction, as shown in Figure 2-7. Tangential cutting speed occurs due to the rotating speed  $V_s$ , the part is feed in the Y direction, and part is also moved along the X-direction. The effect of this motion array can be observed in Figure 2-8. Additional material is plastically deformed as the single grit passes along the already deformed region, as it can be seen in the increasing dimension of the wedge chips.

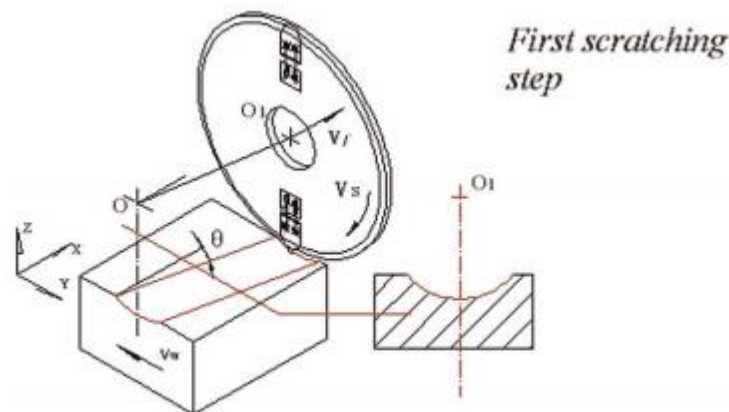


Figure 2-7. Spiral single grit grinding. [42]

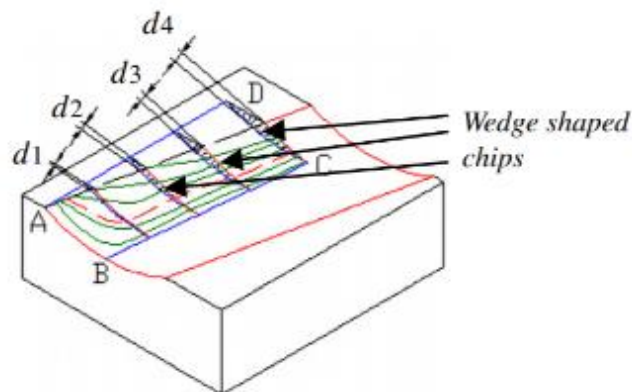


Figure 2-8. Interference pattern on single grit grinding. [42]

Chuang et al. [43] developed a 2D finite element model of the grinding forces and the associated stress and deformation fields generated in a ceramic workpiece during plunge surface grinding. In the model, the grinding parameters and the mechanical properties of the workpiece were utilised as input variables. It was found that the depth of the subsurface shear failure zone increases with an increase in maximum undeformed chip thickness or the wheel

depth of cut. The resulting local grinding force vector, maximum stress and damage zone sizes were predicted as a function of maximum undeformed chip thickness.

### 2.4.1 Material removal mechanism in grinding

The grinding process is analysed by the action of a single abrasive grit, repeated along the contact surface on a specific moment in time. The abrasive grains have irregular shapes and are distributed randomly on the contact surface. Grinding cutting speeds are usually high, from 20 to 30 m/s and up to 150 m/s for special processes. In Figure 2-9 the material removal model is shown. A single abrasive grit moves along the surface at a  $V_s$  speed (tangential speed), and the workpiece moves (or is at rest) in the opposite direction at a speed  $V_w$ . The penetration of the grit into the workpiece causes chip formation, at a shear angle  $\phi$  that depends the grain rake angle  $\alpha$  and the friction angle  $\beta$  and is related to the coefficient of friction  $\mu$  as  $\mu = \tan \beta$ . The expression of  $\phi$  is given by the equation 2-1 [2].

$$\phi = 45^\circ + \frac{\alpha}{2} - \frac{\beta}{2} \quad (2-8)$$

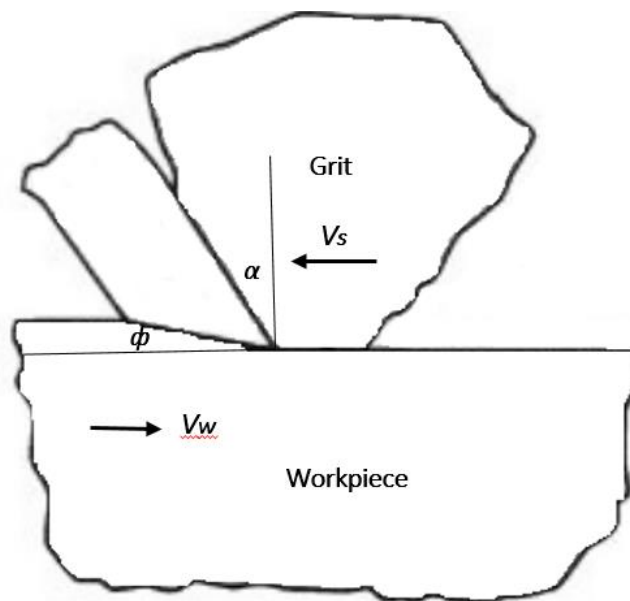


Figure 2-9: Basic material removal mode for grinding

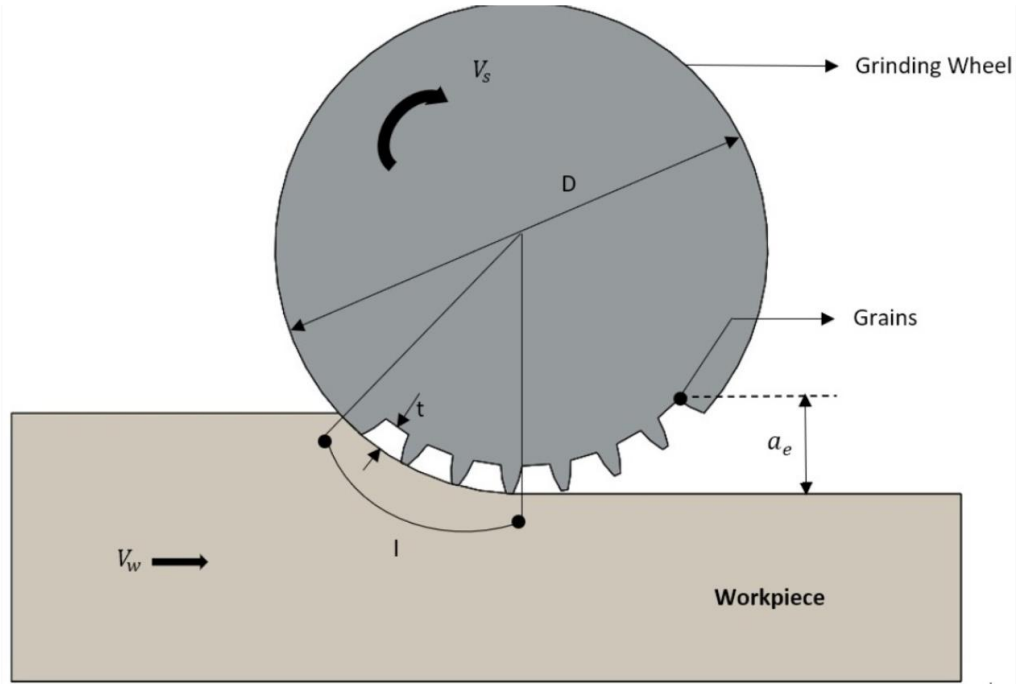


Figure 2-10: Surface grinding model [2]

A surface grinding model can be observed in Figure 2-10. In this model, a wheel with diameter  $D$  is grinding at a cutting depth  $d$  on the material. An undeformed chip length  $l$  and undeformed chip thickness is produced by this process. The following expressions are approximations of the undeformed chip length and thickness [2].

$$l = \sqrt{Da_e} \quad (2-9)$$

$$t = \sqrt{\left(\frac{4V_w}{V_s N r}\right) \sqrt{\frac{a_e}{D}}} \quad (2-10)$$

$N$  is the number of abrasive grits per unit area, usually ranging from 0.1 to 10 /  $\text{mm}^2$ , depending on the grit size;  $r$  is the ratio of chip width to average undeformed chip thickness and is estimated to be between 10 and 20.

It is worth noting that the actual size of the chip, when measured, will be different from the calculated value using the previous expressions, because of the plastic deformation that the chips will incur previous to their fracture.

Similar to other machining processes, grinding parameters such as material removal rate, the

power required, torque, and cutting force can be calculated. The material's specific energy to grind is used as an input for these calculations. Expressions found for this process are [2]:

$$MRR = a_e w V_w \quad (2-11)$$

$$Power = u * (MRR) \quad (2-12)$$

$$Power = T\omega \quad (2-13)$$

$$T = F_c \frac{D}{2} \quad (2-14)$$

Where:

$MRR$  = Material Removal Rate.

$a_e$  = cutting depth.

$w$  = width of cut.

$V_w$  = part moving speed.

$u$  = Specific cutting force.

$T$  = Wheel torque.

$\omega$  = Rotation speed.

$F_c$  = Cutting force.

$D$  = Wheel diameter.

Temperature rise due to friction is another important process parameter to consider during the grinding operation. The heat generated at the interface of the wheelwork because of the plastic deformation leads to the chip formation and frictional sliding. The chips then travel along the grain rake face and produce further heat at the contact zone. These temperatures can induce metallurgical changes on the workpiece, induce internal stresses, and as mentioned before, make it difficult to control dimensional accuracy of the part. An experimental relation of the temperature rises to the process parameters have been identified in [2] as:

$$\Delta T \propto D^{1/4} a_e^{3/4} \left( \frac{V_s}{V_w} \right)^{1/2} \quad (2-15)$$

From the previous equation it can be noted that to decrease the temperature rise, the work speed  $V_w$  should be increased, and the grinding depth  $d$  should be reduced.

## 2.5 Abrasive cutting of ductile materials

Abrasive machining of ductile materials is not as complex as that of brittle materials. The machining process is easy to control since ductile materials are less likely to undergo catastrophic failure. As the probability of crack formation is less, ductile materials can be ground with high cutting speeds and high cutting forces; resulting in high material removal rates. There are abrasive materials specifically designed to grind ductile materials [44].

- Aluminium oxide for ductile ferrous variations, high-tensile-strength alloys
- Zirconia alumina can be used when depth of cut is larger. Larger depth of cuts results in high torques on grinding wheels. Zirconia alumina abrasive wheels can withstand high torques. Optimal to use against ductile ferrous variations, high-tensile-strength alloys
- Silicon carbide can be used against nonferrous metals such as aluminium, bronze and copper, and are also optimal for low-tensile-strength ferrous materials such as cast iron and ductile iron.

### 2.5.1 Rubbing Mechanism

- When the material being machined is softer and ductile, the rubbing model of abrasive wear happens at the very beginning of interaction. The rubbing mechanism causes the material to deform elastically [45].
- As an abrasive grit slides on the workpiece surface for a small distance at the initial stage, the grit-workpiece interaction does not cause any permanent change on the surface topography, where the interaction only occurs in the elastic range and recovers due to the elastic spring back effect after the interaction ends.

### **2.5.2 Ploughing Mechanism**

- Unlike the rubbing mechanism, the ploughing mechanism involves interacting with the material on depths from the surface. When the depth of cut is involved with the grinding operation, abrasives plastically deform all the material they come into contact with. The deformed materials chip away in different shapes, based on cutting parameters like coolant type, depth of cut, cutting apex and material type.
- The ploughing stage is initiated with increasing penetration of the grit into the workpiece while the abrasive grit travels forward simultaneously. At this stage, the interaction occurs in both the elastic and plastic regions, but no real material removal occurs.

### **2.5.3 Cutting Mechanism**

- When the material is peeled off from the surface and gets removed by means of chips then the removal material is considered as the cutting mechanism [46].

## **2.6 Abrasive cutting of brittle materials**

Unlike ductile materials, abrasive cutting mechanisms of brittle materials result in completely different outcomes due to many factors. Grain sizes of brittle materials are finer than those of ductile ones. Thus, dislocation movements are restricted along the grain boundaries, which makes brittle materials more likely to crack. When applied upon stresses, cracks drastically propagate prior to the catastrophic failure in brittle materials [47]. When brittle materials are subjected to grinding actions, propagations of numerous small-scale cracks cause their surfaces to chip away. Technically, infinitesimal failures occur along the cutting surface when brittle materials are under abrasive grinding operations. These chipping mechanisms are highly uncontrollable, thus abrasive grinding of brittle materials is somewhat more complex than that of ductile materials. In order to maintain a steady operation in abrasive grinding operations of brittle material, ductile behaviour of brittle materials, chip formation mechanism, friction characteristics of abrasive grains and many variables should be closely studied [48], [49]. In abrasive grinding and cutting operations, friction between surfaces has a great significance, thus controlling the cutting force is important as well. Metals like cast iron and high carbon steel are known as brittle materials. Also, all the types of ceramics, advanced ceramics (silicon carbide, zirconium oxide, aluminium oxide) glass and many hard-plastic variations are considered as brittle materials [50].

### 2.6.1 Abrasion Mechanisms of Brittle Materials

The material removal in brittle materials is characterised by chip fracturing and cracks on the workpiece surface [47], [51]:

- Chip fracturing is the most common brittle abrasion mechanism. Chip fracturing occurs when infinitesimal fractures on the contact surface of the grinding grain and material cause tiny chips to break away.
- The mechanism can be modelled by dragging a sharp indent along the brittle material. When the indent is pressed against the brittle surface, chips can be seen parting away and a permanent impression can be seen along the path after the indentation is removed.
- When the indentation is loaded heavily against the brittle surface, cracks starts to propagate below the impression (Figure 2-11). Because of the fine grains, the crack can propagate deep into the material if allowed. This phenomenon can be explained through the elevated fracture toughness values ( $K_{IC}$ ) of brittle materials.
- When the indentation force is further increased, lateral cracks starts to appear, in addition to the deep crack at the bottom.

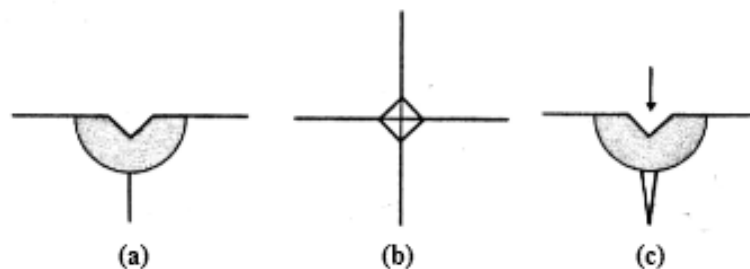


Figure 2-11: (a) Side view of the initial impression, (b) Top view of the initial impression and (c) Propagation of the crack below the impression after the indentation is loaded [47]

### 2.6.2 Research Focus in Brittle Region

In this research, scope is aimed to analyse the behaviour of abrasion of brittle materials sapphire and zirconia. In [52], a detailed explanation about the grinding process of sapphire wafers is reported. Diamond abrasives were used to grind single crystallized sapphire wafers. Switching the grinding process between the lapping and grinding process was done through controlling the grinding wheel speed. In the research, the grinding process was the main focus since it results in better surface roughness. Sapphire wafers of 150 mm diameter were ground using

diamond cup wheels attached to a high precision SGR-700 grinding machine. The diamond grinding wheel was rotated at about 25 RPM and fed against the sapphire wafer at 40 m/min rate. After the grinding process, surface topology of sapphire wafers was inspected by a 3D laser microscope. It was discovered that the grinding process result in less aspirates than the lapping mechanism. Dislodging of diamond grains on the grinding wheel was also observed in the research. The very high hardness of sapphire causes the diamond grits to dislodge.

A paper about assessing the grinding quality of sapphire surfaces using laser imaging can be seen from 2010 [53]. The main purpose of the research was to initiate a modernized grinding process for sapphire, as there were not efficient and quality preserving processes developed. The process was tested on sapphire wafers using several grinding wheel specifications. The main objective of the introduced grinding method was to increase the machining rates, preventing scratch marks on the surfaces and improving the overall surface quality.

The grinding of zirconia using resin bonded diamond wheel was reported in [54]. An evaluation of final ground outcomes with different grinding variables was described. The chipping phenomenon of brittle zirconia was observed to be affecting the controllability of the experimental process. It was observed that, the grinding mechanism of pre-sintered zirconia used in the research was dominated by brittle fracture. The conclusion was derived after observing the chip morphology.

### **2.6.3 Brittle to ductile transition during ultra-precision grinding**

During the brittle material machining, the transition of brittle to ductile cutting mode is considered as a significant phenomenon. When the thickness of un-deformed chip is decreased to be adequately small value normally at submicron level then the machining of the brittle material can be done in the ductile modes [55]. The brittle materials have ductile behavior below the indenter which can be because of the mechanism of phase transformation in which the brittle solid characteristic phase transforms into the metallic phase with the effect of hydrostatic pressure. The theories with the preexisting micro-defects assumed that there could be some defects exist in the cutting stress field zone and the stress field size decreases with the machining scale. The defect concentration in the stress fields also decreases with the machining scale and removes the brittle fracture and enhances the fracture toughness [56]. The cutting in ductile mode is typically a periodic process and comprised on a two stage cycle, such that the elastic deformation dominated stage and the plastic deformation dominated stage During the

elastic deformation stage, the tool constricts elastically the workpiece for increasing the shear or compressive stress until the critical shear or compressive stress has appeared. After the elastic stage, plastic stage appears with the critical stresses and the plastic flow would occur at this level to allow the formation of chips. The plastic flow will also result in to the strain energy release and as a result the shear or compressive stresses decreases until the plastic flow could not be sustained by shear or compressive stresses. In the brittle mode cutting, after the elastic stage the brittle fracture stage occurs when the critical tensile stresses for brittle fracture have appeared [55].

## **2.7 Literature on modelling and Simulation of the Grinding Process**

### **2.7.1 Introduction**

There are different methods for modelling and studying the forces and parameters critical to the grinding process. Simulation of the grinding process using a well-designed model could solve complex problems in the grinding process behaviour in relation to the machined part quality, tool failure, workpiece deformation and cutting mechanics. In addition, numerical simulations, such as finite element method (FEM), are good techniques to describe machining aspects such as stresses, strains, strain rates, and temperature gradients within the materials that are difficult to determine only experimentally. Finite element analysis and molecular dynamic analysis are utilised for the modelling and simulation of abrasive grit-workpiece interaction. molecular dynamic analysis is a reliable tool for atomistic level while FEA can be applied to macro and micro scale simulations [57] [58]. Another useful method for modelling the grinding process is the Smooth Particle Hydrodynamic method. This method approximates material properties and stated variables as a discrete set of disordered points, or Smooth Particle Hydrodynamic particles [59]. Other successful empirical methods have been published, based on pre-existing force models. The Warner's Force Model was tested for optimizing other high-productivity grinding processes. The Warner's model utilizes empirical constants, derived from the specific scenario. It was found that under specific conditions and environment suitable for a grinding process, the accuracy of this model is acceptable [60]. Slip-line field theory were also used as a method for modelling the forces in the grinding process [61]. The state of the art in modelling and simulation of grinding process is highlighted in the review paper by Brinksmeier et al. [57] in a review paper, highlighted the state of the art in modelling and simulation of grinding process.

## 2.7.2 Slip line model

The abrasion mechanism in the grinding process has been studied by several authors. Grinding has been modelled using planar stress distribution, based on the Mohr circle. Further analysis in the model has been derived into a slip line model. Slip-line field approach is a method for machining analysis, which is used to model plastic deformation in plane strain for a solid that can be considered as a rigid-plastic body. Slip line field theory can provide analytical solutions to a number of metal forming processes, and it utilises plots showing the directions of maximum shear stress in a rigid-plastic body which is deforming plastically in plane strain.

Challen and Oxley [62] utilised a slip-line analysis to describe the forces generated in the abrasive machining process and has illustrated the friction effect in the contact region of the abrasive and the workpiece. Considering the differences in material behaviour, three models were proposed. A ‘wave of asperity deformation’ model related to rubbing, a ‘wave removal’ model related to ploughing and a ‘chip formation’ model related to cutting.

A slip line field model for indentation has been proposed in [63]. The indentation model is shown in Figure 2-12, and it can be observed that the abrasive grain has been modelled as a spherical indenter. As the abrasive penetrates the workpiece material, several stresses are built up on the material surface, displacing it and deforming it plastically. Shear is caused along the shown slip lines, which are lines of maximum shear stress, causing the material to flow sideways and upwards. It can be observed that the slip lines meet the material surface at 45 degrees, and each other at 90 degrees, also, slip lines meet the indenter at a friction angle  $\gamma$ .

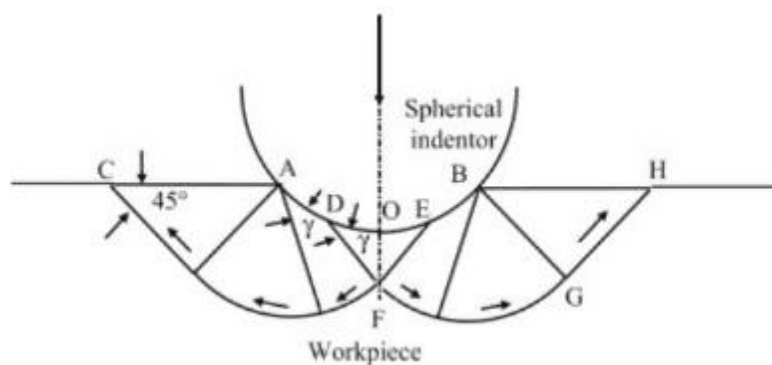


Figure 2-12: Slip line abrasion mechanism [63]

This friction angle is useful when calculating slip line field analysis, to identify stresses directions. The angle is given by the following expression:

$$\gamma = \frac{1}{2} \cos^{-1} \frac{\mu \sigma_n}{k} \quad (2-16)$$

Where:

$\mu$  = Friction coefficient.

$\sigma_n$  = Normal stress on indentation.

$k$  = directional stress.

A dead zone appears between DEF points in Figure 2-12. This zone goes strain hardening as it is displaced, acting as a punch together with the indenter. When a low friction interface is achieved, the friction angle is 45 degrees, and the energy required to indent is greatly reduced [63]. The second abrasive material removal mechanism is caused by tangential motion. A different slip line field study has been conducted in [64]. In this case, tangential motion is the cause of wear of the material surface, as shown in Figure 2-13. The abrasive grit will penetrate the material with an attack angle  $\alpha$ . A plastic wave is pushed ahead causing the slip lines. In this model, fracture is not caused by a single abrasive penetration, rather, for a number of repetitions, or several of the grains penetrating the same region. The number of cycles  $N_f$  to cause fracture is given by the expression bellow.

$$N_f = \left( \frac{2C}{\delta} \right)^2 \quad (2-17)$$

Where:

$C$  = Material critical strain.

$\delta$  = Shear strain.

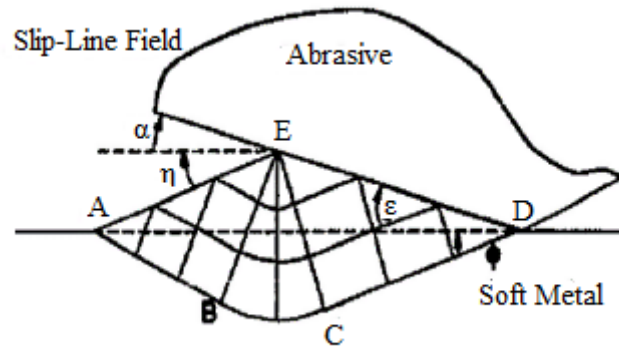


Figure 2-13. Slip line field for mild wear [64]

### 2.7.3 Finite element method approach for modelling material removal

Finite Element Method is a mathematical tool developed to solve complex equation systems. A complex system can be modelled using equations, differential or otherwise, that describe its behaviour. By dividing an object into smaller objects, each one with descriptive equations and boundary conditions, an equation system can be developed and solved using FEM [65]. The finite element method (FEM) is the collection of numerical methods to solve the equation systems that arise from dividing a problem on a finite number of elements. On the other hand, Finite Element Analysis (FEA) is the practical application of FEM. Once data has been generated by solving equations, other engineering equations, principles and data (such as material strength, strain, thermal expansion, etc) can be used to form a more complex solution of the given problem. Fractures, expansion, deformation can be observed in the FEA simulation of the object, and engineering decisions can be made.

The slip line model previously studied has been used to model the shearing mechanism of fracture for grinding. Finite Element Analysis studies have been developed as another approach to model the interface of the abrasive tool and the material by numerical means.

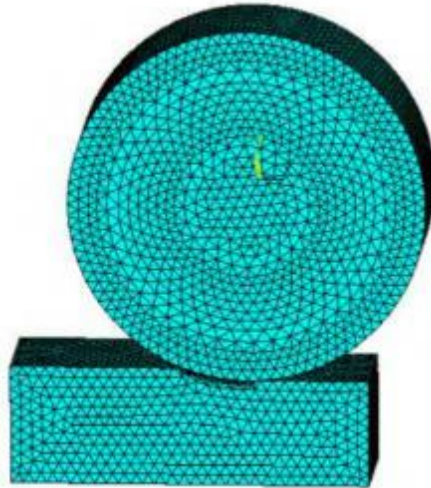


Figure 2-14: Geometric model with mesh for FEA [66]

The simulation referenced in [66], proposes a diamond grinding wheel and a SiC/Al composite workpiece material. The grinding wheel is restrained to move in all directions and allowed to spin only around the direction of its axis, as it is expected in real life. The material block is restrained to move and spin in all directions, except in the horizontal direction towards the grinding wheel, consistent with a worktable feed motion of a grinding machine. The material properties used in the proposed simulation are shown in Table 2-2.

Table 2-2: Mechanical properties of the grinding system [66]

	<i>Young Modulus (GPa)</i>	<i>Poisson's ratio</i>	<i>Density (Kg/m<sup>3</sup>)</i>
<i>Diamond grinding wheel.</i>	<i>1147</i>	<i>0.07</i>	<i>3000</i>
<i>SiC/Al composites</i>	<i>213</i>	<i>0.23</i>	<i>2940</i>

Several simulations were run under different conditions, to build data results. Wheel speed was simulated from 2,500 to 3,500 rpm, feed speed of the material was from 5 to 25 m/min, and grinding depth was simulated from 0.02 to 0.1 mm. The resulting tangential force from the simulations is plotted and shown in Figure 2-15, Figure 2-16, Figure 2-17.

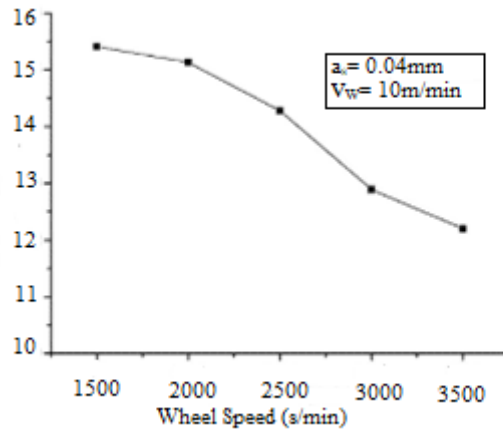


Figure 2-15. Tangential force as a function for wheel speed. [66]

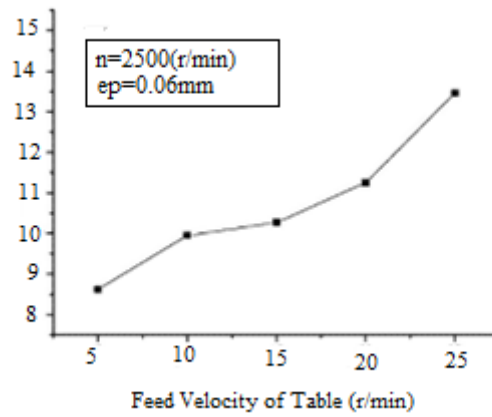


Figure 2-16. Tangential force as a function of feed speed. [66]

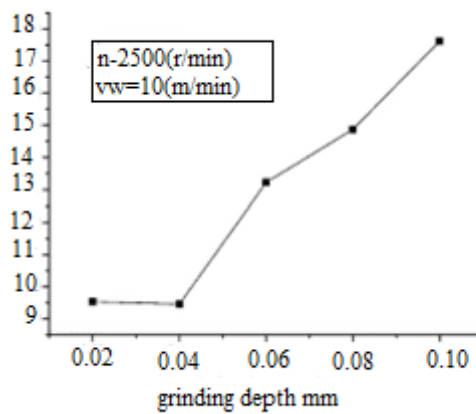


Figure 2-17. Tangential force as a function of grinding depth. [66]

As observed in the figures, the required tangential force is inversely proportional to the rotational speed, directly proportional to feed speed and grinding depth. The results were

validated in [66], comparing them to measurements under the simulated conditions, and observing the same trend and similar numeric results. This study exemplifies the process parameters as observed on a macroscopic scale, in a machine. However, the grinding effect on the part material is not analysed.

As explained in [67], FEA simulations need to have their behaviour characterized, as well as specific criteria to meet for a corresponding effect. In this case, a model of the chip formation and removal was proposed and validated. The study used the ductile and brittle fracture regimes for material removal in grinding on a hard and brittle material, Silicon Carbide using diamond abrasives.

As previously mentioned, an abrasive grit can cause diverse effects on the material. Ductile fracture occurs when the abrasive causes an elastic deformation on the material, followed by plastic deformation, and finally material removal by material failure along the abrasive path, similar to metal cutting on other machining processes. Brittle fracture occurs when the material is removed by the propagation of micro-cracks on the surface, which can extend to the subsurface of the material. Subsurface cracks can have a negative effect on the morphology of the material surface as well as on their mechanical properties [67]. Figure 2-18 shows both modes and their effect on the material.

The fracture mode occurring on the grinding process simulation will depend on the criteria programmed into the FEA. The Effective Plastic Strain criterion is commonly used for modelling material fracture in grinding processes. Under this criterion, the material chip is considered to be removed once the strain on the material chip has exceeded the Failure Strain, as shown in Figure 2-19.

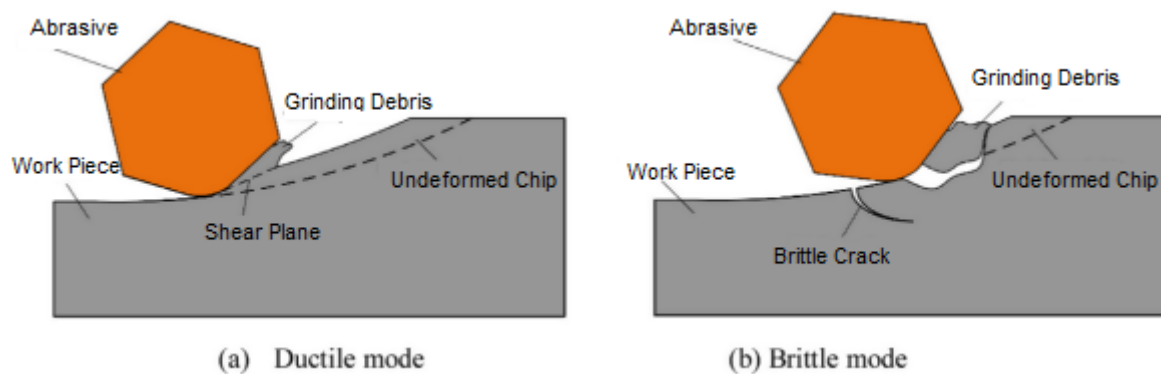


Figure 2-18. Ductile and Brittle fracture modes on grinding. [67]

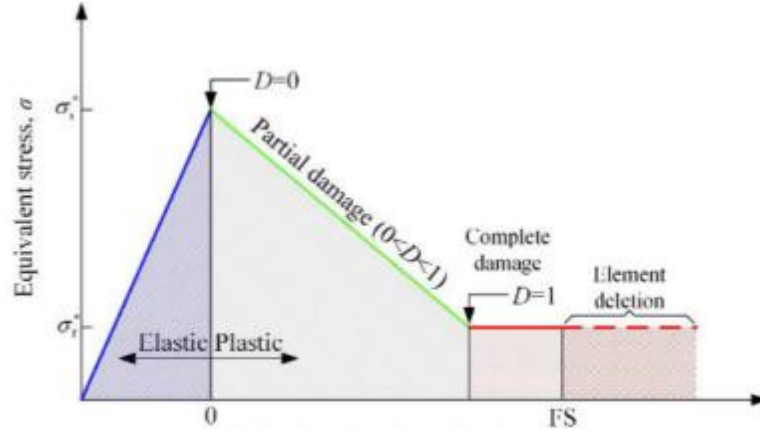


Figure 2-19. Equivalent Plastic Strain Criterion. [67]

The EPS criterion uses equivalent tension stress as the main contributor to achieve strain. However, materials such as Silicon Carbide, and other strong and hard materials, do not behave in this manner. For this reason, the study referenced in [67] couples a Tensile Strength fracture criterion with a Maximum Shear Strength criterion. It is proposed that the material will be removed in ductile mode when the following condition is satisfied:

$$\begin{cases} \sigma_1 < \sigma_c \\ \tau_{max} > \tau_c \end{cases} \quad (2-18)$$

Where:

$\sigma_1$  = First principal stress due to grinding.

$\sigma_c$  = Critical tensile strength.

$\tau_{max}$  = Maximum shear stress.

$\tau_c$  = Critical shear strength.

Similarly, a brittle fracture will occur when the following condition is met:

$$\sigma_1 > \sigma_c \quad (2-19)$$

For reference, for silicon carbide, the material studied,  $\sigma_c = 0.37$  GPa and  $\tau_c = 0.142$  Gpa. A single grain grinding process is used in the proposed FEA, which is shown in Figure 2-20.

Several process variables can be observed, such as the maximum undeformed chip thickness  $a_{gmax}$ , the depth of cut  $a_p$ , the workpiece feed speed  $v_w$ , the grinding wheel speed  $v_s$ , and the equivalent grinding wheel diameter  $d_{eq}$ .

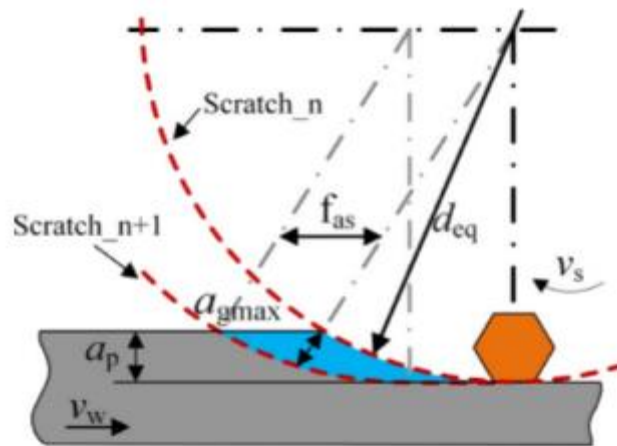


Figure 2-20. Single grain grinding model [67]

This model was constructed with the mesh shown in Figure 2-21. As it can be observed, there are elements for the grinding diamond grain, shown in red, and many more elements for the workpiece shown in grey. The diamond is displaced along the  $X$  direction, through the uncut chip as a tangential motion. The workpiece has dimensions  $H$  height and  $L$  length;  $a_{gmax}$ , is set to 1  $\mu\text{m}$ . The diamond speed is programmed to be 20  $\text{m/s}$ .

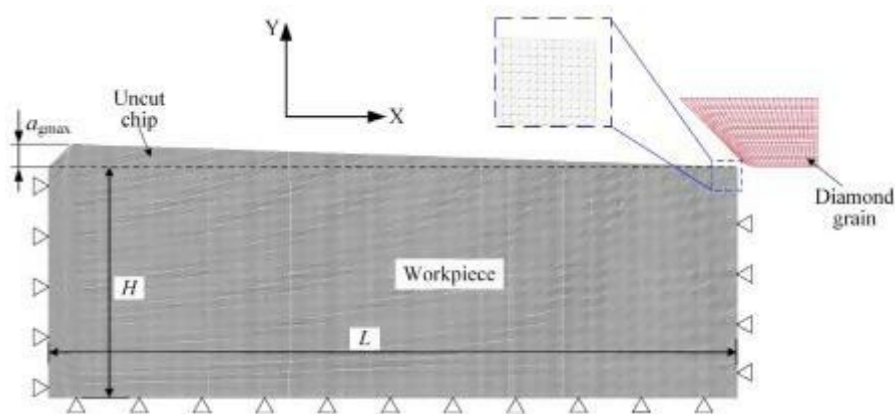


Figure 2-21. Finite element model for single grain grinding [67]

The model was simulated with EPS and TSC fracture criteria. The graphic representations of the results are shown in Figure 2-22.

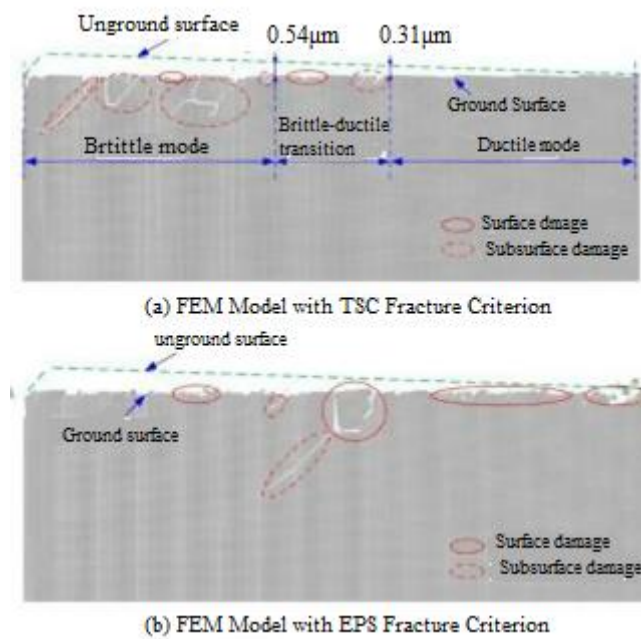


Figure 2-22. FEA results with different fracture criteria [67]

Comparing the simulation results, it can be observed that under the EPS criterion, deep fracture damage is observed randomly on the material surface, with subsurface cracks concentrated in the middle. While the simulation using the TSC criterion, shows three more defined regions, an initial ductile mode region, a transition region, and a brittle fracture region. The fracture mode is dependant of the grinding depth of the process.

The simulation results were validated with an experimental set-up. A single abrasive was bound using an Ag-Cu-Ti allow, on a 400 mm diameter wheel. Data was collected using force sensors and a data capture system. Silicon carbide was ground, and data collected for the validation experiment. Afterwards, the surface morphology of the ground specimen was observed using an electron microscope. Figure 2-23 shows the different morphologies at different grinding depths; it can be observed that with chip thickness less than 0.1  $\mu\text{m}$ , the resulting surfaces are smooth with plastic deformation grooves along the cutting direction. With chip thickness of 0.3  $\mu\text{m}$ , several cracking pits are observed, as well as plastically deformed grooves, stablishing 0.3  $\mu\text{m}$  as the critical undeformed chip thickness. Greater thickness, yields a rough surface with cracking pits, corresponding to brittle fracture removal.

It can be observed that the morphologies correspond to the results of the TSC simulation, where the surface is observed to have ductile fracture with small cutting depths, and changes to brittle fracture as the grinding depth increases. This is the same conclusion reached in [67].

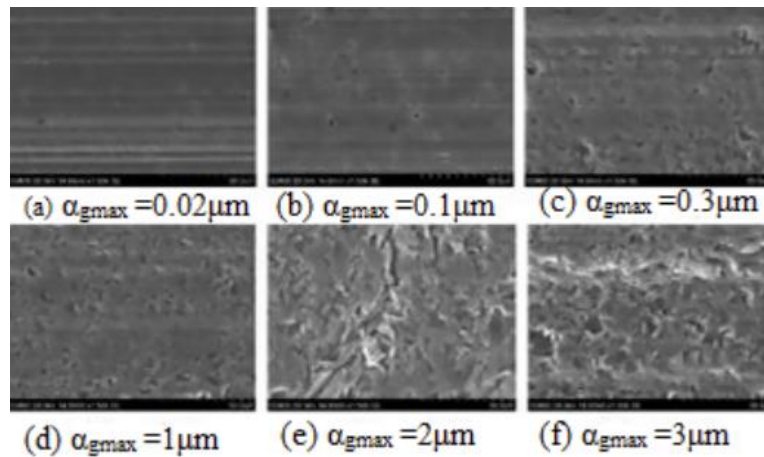


Figure 2-23. Surface morphology at different grinding depths. [67]

## 2.8 Literature on diamond wire saw cutting

The Diamond Wire Sawing (DWS) cutting process has gained popularity in recent years, especially in difficult and demanding industries that have special cutting requirements. This process uses a flexible wire with embedded abrasive diamonds as the cutting tool, which is driven along a surface to cut, gradually removing the material. The wire flexibility is the principal advantage of this process, allowing it to cut irregular geometries. Another important advantage is the reduction of cutting waste material using a wire of minuscule diameter. For the advantages and the versatility to adapt to different working conditions, this process is widely used in the semiconductor, marble and oil and gas industries.

- **Silicon**

In the semiconductor industry, this process is used to produce silicon wafers, cut from an ingot of silicon carbide. Wafers are critical for the process because growing and cutting a silicon ingot represents 28% of the total cost of production of solar panels [68]. The wire used in this industry is thin, from 0.3 to 0.7 mm in diameter, usually made of steel. The abrasive diamonds are bonded to the wire, by electroplating, sintering, or mechanical incrustation [69].

- **Sapphire**

Another use in the semiconductor industry. Sapphire has gained popularity in Light Emitting Diode (LED) manufacturing, due to its transparency and thermal stability [70]. The ingot and cut are shown in Figure 2-24. This process is very similar to silicon carbide cutting.

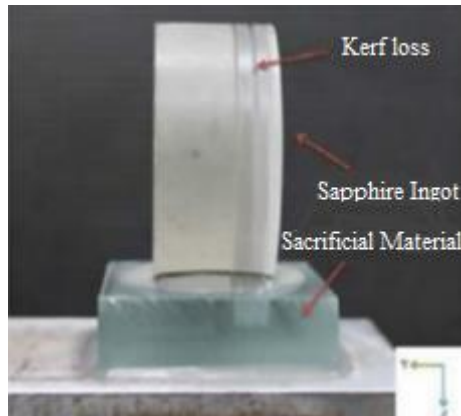


Figure 2-24. Sapphire ingot wire cut [70].

- **Rock**

Diamond wire saw cutting is used in the marble extraction industry. Marble and stone are hard and brittle materials. The desired qualities of the cutting process are similar since the wasted material needs to be reduced to increase inversion recovery. [71]

### 2.8.1 Principal parameters and properties that affect performance.

The performance of the diamond wire sawing process depends on several factors, including machine parameters, material properties, and operator skill. The principal parameters that are identified as affecting performance [72] are:

- Machine parameters.
  - Machine power.
  - Wire speed.
  - Structure of diamond bead.
  - Dimensions of cut.
  - Geometry of wire during cutting.
  - Vibration of the machine.
  - Water/coolant consumption.

- Material properties.
  - Hardness.
  - Strength.
  - Water content.
  - Geometry and texture.
  - Discontinuities
  - Composition.
- Operating conditions.
  - Technical personnel.
  - Techniques used.

### **2.8.2 Diamond wire sawing in monocrystalline silicon ingots.**

Performance of the diamond wire saw cutting process is dependent on process parameters, such as cutting force, wire speed, feed rate, wire bow, wire tension and wire wear. Properties of the material impact the process performance as importantly. For the cutting process of silicon ingots, a model is described in [73]. The study presents a cutting wire with embedded diamonds, as shown in Figure 2-25. This Scanning Electron Microscope image shows different sizes, shapes and distributions of diamonds. It was reported in [73] that the cutting wire moves tangentially along the material surface, with a speed  $V_s$ . This speed is determined by a driving pulley diameter and its rotational speed. There are forces opposing motion, noted as  $F_{at1}$  and  $F_{at2}$ , which need to be compensated by the wire force, also determined by the machine motor torque and the cutting area [73].

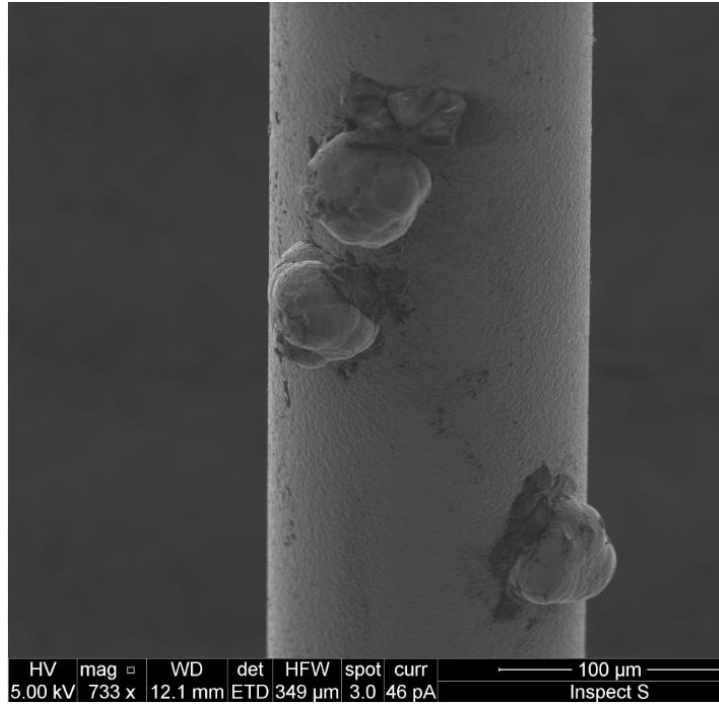


Figure 2-25. SEM photograph of a cutting wire

The principal cutting mechanism on the ingot is micro-fracturing, and the chips cut are removed from the material surface dragged by the moving wire. For each diamond, chip deformation forces  $F_{an1}$  and  $F_{an2}$ , can be considered as a single force  $F_{an}$ . The same can be applied for friction  $F_{at1}$  and  $F_{at2}$  into a force  $F_{at}$ . To take into account the contribution of all of the cutting diamonds on the wire, expressions for the wire tangential force  $F_t$  and normal force  $F_n$  have been proposed in [73]:

$$F_n = K_n \frac{V_x}{V_s} L_c R_w \quad (2-20)$$

$$F_t = K_t \frac{V_x}{V_s} L_c R_w \quad (2-21)$$

Where:

$F_n$ : Wire normal force.

$F_t$ : Wire tangential force.

$K_n$ : Coefficient of normal force ( $N/mm^2$ ).

$K_t$ : Coefficient of tangential force ( $N/mm^2$ ).

$V_x$ : Part feed rate (mm/min).

$V_s$ : Wire saw velocity (mm/min).

$L_c$ : Contact length between wire and part (mm).

$R_w$ : Wire saw radius (mm).

Both coefficients of normal and tangential forces are determined experimentally in [73]. The coefficient of normal force is  $1.52 \times 10^6$  MPa and the coefficient of tangential force is  $4.53 \times 10^5$  MPa. With common process parameters of wire speed of 96,000 mm/min, feed rate of 0.025 mm/min, contact length of 10 mm and wire radius of 0.11 mm, wire normal force is 0.43 N and tangential force is 0.13 N, which are normal magnitudes found in the real process.

Yet another performance indicator for this process, is the surface roughness of the resulting cut. This is especially important in the semiconductor industry because there is the risk of cracks or fractures on the wafer, or more finishing operations required, such as an extended lapping operation. Tangential speed and feed speed during cutting can cause surface damage during the cut. Based on different experiments cutting silicon wafers, [74] concludes that the tangential speed is the main cause of the surface roughness, decreasing roughness as speed increases. Additionally, [74] concludes that cutting forces, normal and tangential, have a direct effect on the surface roughness.

### **2.8.3 Diamond wire sawing in sapphire**

Similar to silicon cutting, sapphire cutting is based on a thin wire to reduce material loss during cutting. It has been proved that for higher forces and bigger abrasives, deeper grooves are created in the sapphire surface. Higher wire speed to feed speed ratio is preferred for cutting sapphire. This is because of the C-plane structure of the sapphire ingot used; a brittle fracture regime is more likely to occur. Ductile cutting has also been observed in sapphire cutting, occurring in higher temperature conditions that should be avoided with proper cooling and lubrication [70].

However, machinability on different crystal orientations differs greatly, as their properties. A-plane sapphire machinability under diamond wire saw cutting has been studied in [75]. It was found that tangential and normal cutting forces vary greatly according to the crystal orientation where it was cut while cutting at speeds of 200 m/min. On the other hand, the forces were more stable at higher speeds, up to 600 m/s.

Moreover, it was found that the optimal direction for cutting A-plane sapphire is the A-M direction (Figure 2-26). This direction yields the minimal sawing forces, lowest material removal energy, and lower fracture strength. In this direction, productivity can be increased by increasing feed rate.

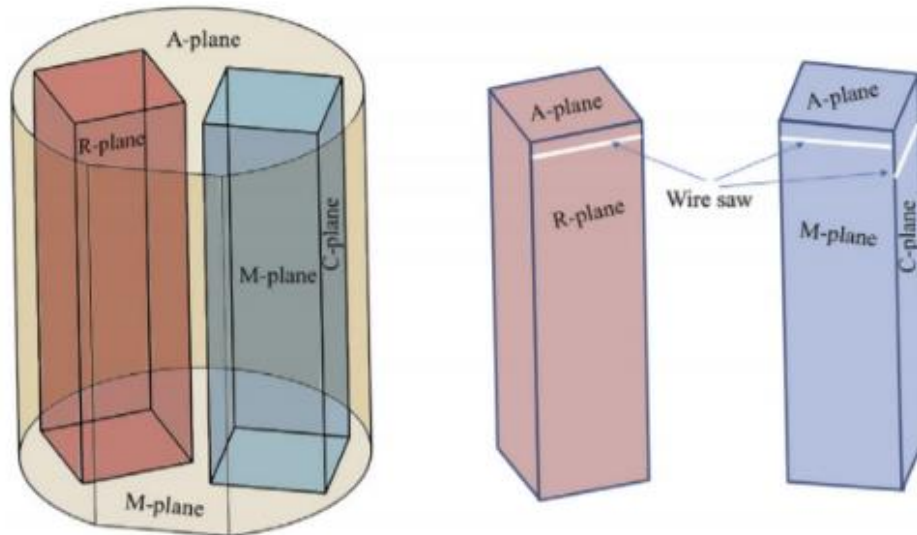


Figure 2-26. Crystallographic directions of sapphire [75].

#### 2.8.4 Performance similarities of the variants of the process.

Having reviewed the performance of different cutting processes with diamond wire, many similarities can be observed. The most evident is the mechanics of the cut. Different authors point out that the cutting occurs by a grinding process, as well as material fracture. Depending on the properties of the material, the fracture will be brittle or ductile.

This type of ductile fracture has been studied in cutting different materials, silicon and sapphire. It has been identified as beneficial for removal or reduction of the formation of microcracks and deep damage in the material, therefore increasing the resultant material strength. On the other hand, brittle fracture has been observed to be more productive, with greater throughput. Switching between the brittle and ductile manufacture can be achieved in the same process, by carefully controlling the process parameters [76].

Wire abrasive morphology has been observed to have a great impact on morphology of the cut part, affecting roughness and strength. While ductile cut on brittle materials has been observed under specific cutting conditions, [77] has shown that the wire morphology plays an important

role in achieving the desired effect. This study compares the effect of cutting with a new wire against a used one. The diamond grit characteristics have been changed by wear and therefore, the part morphology is affected. Using a cutting speed of 18 m/s, feed speed of 0.8 mm/min and a wire with 8-12  $\mu\text{m}$  diamond grits, silicon wafers were cut. The experiment analyzed two conditions, a new wire, and a worn wire. The first effect of wear on the abrasive diamonds has been observed in the surface finish of the part. The measured surface roughness of a part cut with a new wire was higher than a part cut with a worn wire [77]. Subsurface damage is reported to be more evident with a new wire. The effect is that the brittle fracture propagates to below the surface of the workpiece. Cutting with a new wire resulted in 9 of every 10 locations presenting microcracks of subsurface damage. Contrary to this, using a worn wire to cut resulted in only 4 out of 10 locations presenting this damage.

## **2.9 AE feature and analysis**

Grinding monitoring enables the online supervision of crucial aspects of the process, such as tool state, surface quality, and dimensional accuracy; and possesses a great advantage over traditional post-process quality control techniques by reducing costs and inspection times. Such an advantage relies on a good interpretation of monitored signals in relation to grinding behaviours. This section presents an experimental study on acoustic emission (AE) features in abrasive grinding scratch experiments.

An online monitoring system for machining processes could have remarkable impacts on a CNC machine tools system in reducing manufacturing cost and time in the product inspections, and avoiding the need for post-process quality control [78] [79]. Online monitoring techniques allow the real time evaluation of crucial aspects of the machining processes, such as tool condition [80] [81], chatter [82], surface finish [83] [84], chip formation [85], surface damage [86] [87], and so on. In order to provide effective information with online monitoring techniques, the selection of adequate sensors, signal processing methods together with predictive techniques should be optimised according to the specific parameters under analysis. A broad range of sensors have been used in machining process monitoring, including dynamometers, accelerometers and acoustic emission sensors [79]. For online process monitoring, different signal processing methods in the time domain and frequency domain have been applied, i.e., time direct analysis (TDA) [83], singular spectrum analysis (SSA) [88], Fourier transform [83], wavelet transform [89], and so on. Considering correlating features of

the parameters under study, several predictive techniques have been applied in many researches, i.e., the multivariate regression [90], the artificial neural networks [83] and the support vector machines (SVM) [81].

Of all machining processes, grinding is one of commonly used processes for finishing operations that produce workpieces with close tolerance and high surface quality. In grinding, the wheel surface topography is an important aspect to evaluate due to the abrasive grain shapes changing continuously, which directly affects the ground component quality. In recent years, online monitoring techniques have been extensively applied to grinding processes to monitor important aspects, such as tool wear [91], surface finish [92], surface damage [86], and so on. Nguyen et al. [92] developed a model to predict the abrasive wear and the surface finish using cutting force signals. The signals were processed in time and frequency domain and the wear and the surface finish were predicted using adaptive neural fuzzy inference system, Gaussian process regression and Taguchi methods. Similarly, Tang et al. [93] developed a mathematical model of grinding forces to characterise the surface topography of the workpieces.

One of the most important signals used in grinding process monitoring has been acoustic emission (AE), which is defined as an elastic wave propagation in the bandwidth between 20 and 2,000 kHz due to material molecular displacements under stresses [94]. In grinding, the AE signal represents many important aspects of grinding, such as: grain and bounding ruptures in the wheel, workpiece chipping, cracks, elastic and plastic deformation, phase transformation, and so on. Thus, AE signal has been used to characterise different physical performances of grinding processes. Boaron and Weingaertner [80] analysed acoustic emission signals in both the time and frequency domain for evaluation of the topographic characteristics of a fused aluminium oxide grinding wheel. The method was based on the detection of the effective width of the grinding wheel with an instrumented diamond tip. Rameshkumar et al. [81] registered the acoustic signal in grinding operations to predict the wear level of the grinding wheel. The acoustic emission was analysed in the time domain using different features such as root mean square, amplitude, ring-down count, average signal level. By using machine-learning techniques, for example, decision tree, artificial neural network, and support vector machine, they could estimate if the wheel was sharp or dull. Using the same way, Liao [89] developed a grinding wheel condition monitoring method based on acoustic emission wavelet packet transform to estimate the wheel sharpness or dullness. Later, Liao [95] developed a model based on the analysis of acoustic emission signal using autoregressive modelling and discrete wavelet decomposition to classify the state of the grinding wheel. Liu et al. [86] [87]

determined the wavelet packet transform was an ideal signal processing method to evaluate the acoustic emission signal and to extract features correlated to the grinding burn phenomena. Chiu and Guao [96] constructed an SVM model for the state classification of CBN grinding with featured data from the acoustic emission signal. Dias et al. [97] proposed a new methodology to predict and detect the surface quality and the dimensional errors by acoustic emission in the centreless grinding process. The acoustic emission was processed in both the frequency and the time-frequency domain by fast Fourier transform and wavelet analysis, respectively.

## **2.10 Summary and literature key gap**

Despite the improvements made in grit characterisation, few attempts have been made to narrow the gap between the description of real grit shape and characteristics in relation to the abrasion functions on processes. Such relationships are critical in the development of abrasion models. It appears that one of the major reasons for the lack in the shape definition comes from the difficulties related to measuring and quantifying the grit's shape. Grain shapes consist of irregular and multiple geometries and often a simplified description as conical, elliptical, or spherical is used in wheel modelling applications. These models proposed are mainly considering the abrasive shape as perfect shape (sphere, cone...) which are far from the reality. Furthermore, using acoustic emission signals in grinding process monitoring is commonly applied to assess the wear level of the grinding wheel. However, the direct relationship between the acoustic emission and the surface creation of the machined workpiece in relation to grain shapes have not been studied in a good extent and more research in this field is required. These problems will be addressed in this thesis by characterising a set of parameters and features in order to define more accurately the grit's shape and developing test methods that can improve the assessment of grit characterisation.

## **Chapter 3 Abrasive grits characterisation and shape classification**

The grit characterisation is the measurement of grit properties, which are key factors for its performance. Aiming at the development of new test methods for micron diamond processing assessments, a set of abrasive grit assessments based on observation image analysis has been carried out to distinguish the shape differences of the abrasive grits. In this study, initially loose diamond abrasives sorted in different samples were assessed and then diamond abrasives bonded to a cutting tool were again assessed. The cutting tool was then utilised to carry out experimental scratching tests. Thus, in the considered cutting tool or in the loose abrasives samples, thousands of abrasives are present and therefore it was not possible to assess individually every abrasive. However, the analysis was carried out in terms of statistics.

### **3.1 Geometrical grit's shape classification approach**

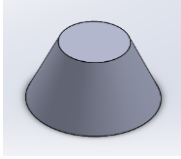
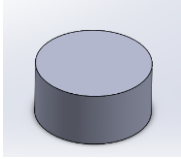
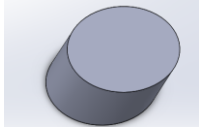
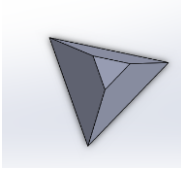
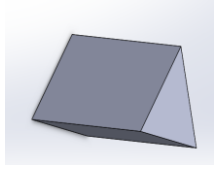
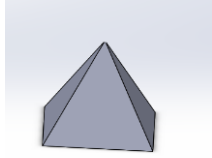
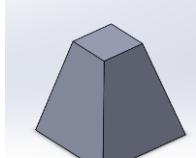
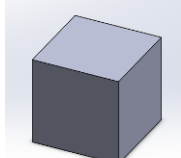
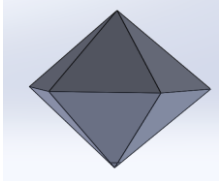
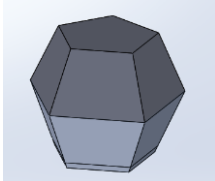
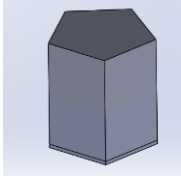
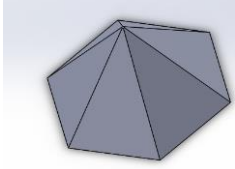
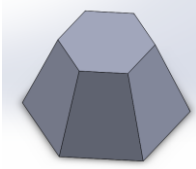
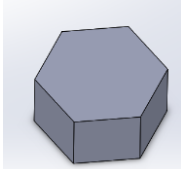
The approach of grit shapes classification was based on visual judgement. i.e., identification of the shape of the grain projection, i.e., the 2D grain image or 2D analogue of its spatially volumetric shape, is considered. The attempt consists of the grit classification based on their morphological aspects. This shape aspects criteria are shown in Table 3-1.

Table 3-1: Classification shape criteria

<i>Group shape</i>	<i>Aspect criteria</i>
<i>Sphere</i>	<i>radius</i>
<i>Ellipsoid</i>	<i>major and minor axis</i>
<i>Triangular pyramid</i>	<i>three edges and one peak height</i>
<i>Rectangular pyramid</i>	<i>four edges and one peak height</i>
<i>Pentagon pyramid</i>	<i>five edges and one peak height</i>
<i>Hexagon pyramid</i>	<i>six edges and one peak height</i>
<i>Triangular frustrum</i>	<i>three edges and one truncated height</i>
<i>Truncated tetrahedron</i>	<i>Four edges and one truncated height</i>
<i>Truncated pentagon</i>	<i>five edges and one truncated height</i>
<i>Truncated hexagon</i>	<i>six edges and one truncated height</i>
<i>Triangular prism</i>	<i>three edges and one top height</i>
<i>Cube</i>	<i>four edges and one top height</i>
<i>Pentagonal prism</i>	<i>five edges and one top height</i>
<i>Hexagonal prism</i>	<i>six edges and one top height</i>
<i>Rounded cylinder</i>	<i>round bottom surface and round top height</i>
<i>Oval cylinder</i>	<i>oval bottom surface and one oval top height</i>
<i>Rounded base section cone</i>	<i>round bottom surface and one peak height</i>
<i>Oval base section cone</i>	<i>oval bottom surface and one peak height</i>
<i>Truncated rounded base cone</i>	<i>round bottom surface and one top height</i>
<i>Truncated oval base cone</i>	<i>oval bottom surface and one truncated top height</i>

Table 3-2 shows the geometrical figures considered here as a common base used for grit shape identification criteria of categorisation to identify and classify abrasive grits according to their geometries with acceptable similarity. This classification is considering the point contact between the abrasive and the workpiece.

Table 3-2: Grit's shape classification

<i>Rounded shapes</i>	<i>Cone shapes</i>	<i>Truncated cones shapes</i>	<i>Columns shapes</i>	<i>Other shapes</i>
<p><i>Spherical</i></p> 	<p><i>Rounded base section</i></p> 	<p><i>Truncated rounded base</i></p> 	<p><i>Rounded cylinder</i></p> 	<p><i>All other shapes</i></p>
	<p><i>Oval base section</i></p> 	<p><i>Truncated oval base</i></p> 	<p><i>Oval cylinder</i></p> 	
	<p><i>Tetrahedron pyramid</i></p> 	<p><i>Tetrahedron frustrum</i></p> 	<p><i>Triangular prism</i></p> 	
<p><i>Ellipsoidal</i></p> 	<p><i>Quadrilateral pyramid</i></p> 	<p><i>Quadrilateral frustrum</i></p> 	<p><i>Cube</i></p> 	
	<p><i>Pentagonal pyramid</i></p> 	<p><i>Pentagonal frustrum</i></p> 	<p><i>Pentagonal prism</i></p> 	
	<p><i>Hexagonal pyramid</i></p> 	<p><i>Hexagonal frustrum</i></p> 	<p><i>Hexagonal prism</i></p> 	

A set of 21 group shapes is defined as follows:

- **Rounded shapes:** Sphere, Ellipsoid.
- **Cone shapes:** Base sections are round, oval, polygons up to 6 sides.
- **Truncated cone shapes:** Base sections are round, oval, polygons up to 6 sides.
- **Columns shapes:** Base sections are round, oval, polygons up to 6 sides.
- Other shapes not covered by above types.

Considering the observation from one direction under a microscope, a 2D image of the grits is taken and then the grits are classified regarding their 3D corresponding regular shape. Such classification contains 21 groups of grit shapes (which is still too many for practical application).

### **3.2 Initial work: assessment of loose abrasives**

In the analysis of the grit shapes was carried out by observing diamond abrasive grits under an optical microscope with a magnification that was adapted to avoid the grit size. This initial investigation was carried out on nine diamond loose abrasive samples, namely:

- PD M0510 (grits size from 5 to 10  $\mu\text{m}$ ),
- MDA C (grits size from 30 to 40  $\mu\text{m}$ ),
- MDA A (grits size from 20 to 30  $\mu\text{m}$ ),
- MDA M1225 (grits size from 12 to 25  $\mu\text{m}$ ),
- MDA M0510 (grits size from 5 to 10  $\mu\text{m}$ ),
- CDA M1530 (grits size from 15 to 30  $\mu\text{m}$ ),
- Synthesized M4060 (grits size from 40 to 60  $\mu\text{m}$ ),
- Synthesized M2030 (grits size from 20 to 30  $\mu\text{m}$ ),
- MDA B (grits size from 20 to 30  $\mu\text{m}$ ).

#### **3.2.1 Sample preparation process**

In sample preparation process, the abrasives were sprayed on the glass slide, well dispersed, rather than clusters or overlapped samples, to avoid a difficult to capture situation and to carry out microscopy observation tests. The number of the sampled grits observed in tests is only a very small proportion of all the samples. Thus, proper sampling number in tests is crucial to fulfil statistical analysis (i.e. to improve the objectivity of the classification). Each group of the

samples is composed of over 100 grits randomly captured under an optical microscopy vision area.

### 3.2.2 Microscopy Measurement Process

Optical microscopy technique is commonly used to measure diamond grits by capturing their clear images. The samples in the images are then dimensioned for size dimension analysis and shape classification. The process allows to observe the positioned samples and to evaluate their shape characteristics and size band. Prior to measurement, the scale calibration of the microscopy device is essential to significantly assure reliability of the test according to accuracy standards and size distribution of the grits. After that, different size distribution of the samples could be constructed by visually classifying and accumulating counts in sequence. Following such a defined procedure, the characterization criteria of size and shape distribution is elaborated. So far, automated optical scanning system (e.g. using optical or SEM microscope coupled with a computerized image analyser) can eliminate most of the fatiguing measurement works [98]. However besides high cost, not a single technique or feasible device is available to measure and identify the size and shape spectrum of the grits at consistent accuracy. Each technique/device is capable of providing optimal application in a certain size range based on specific 2D profile similarity (e.g. circularity and sphericity ) characterization.

In the investigation, the images of the grits are captured under a Leica DFC 295/CH9435 optical microscope (Leica Microsystem Ltd, Germany) [99], shown in Figure 3-1, coupled with an objective lens of magnification  $\times 100$ ,  $\times 50$ ,  $\times 20$ ,  $\times 10$ ,  $\times 5$ . The microscope, with a scanning distance from  $0.5 \mu\text{m}$  to  $2000 \mu\text{m}$  is equipped with a digital camera OLYMPUS BX51M. The size and morphology analysis are carried out with an image analysis software (LAS V3.6).



Figure 3-1: Leica microscope

The images of grits are shown in Figure 3-2. Once the images are obtained, grit size, geometrical aspect ratio, distribution and shape classification are evaluated. Measuring manually different geometric parameters of each grain or grit was time-consuming.

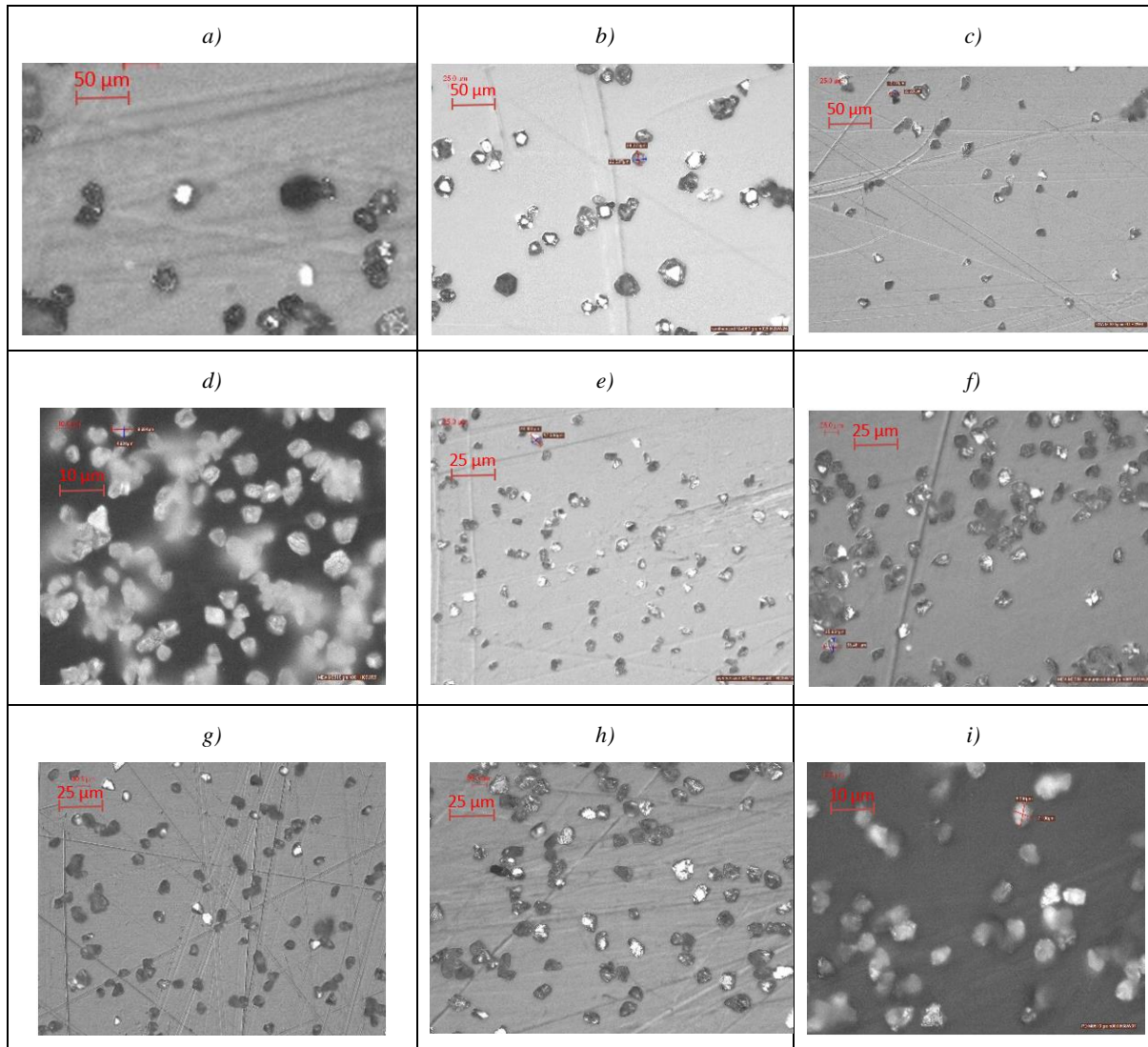


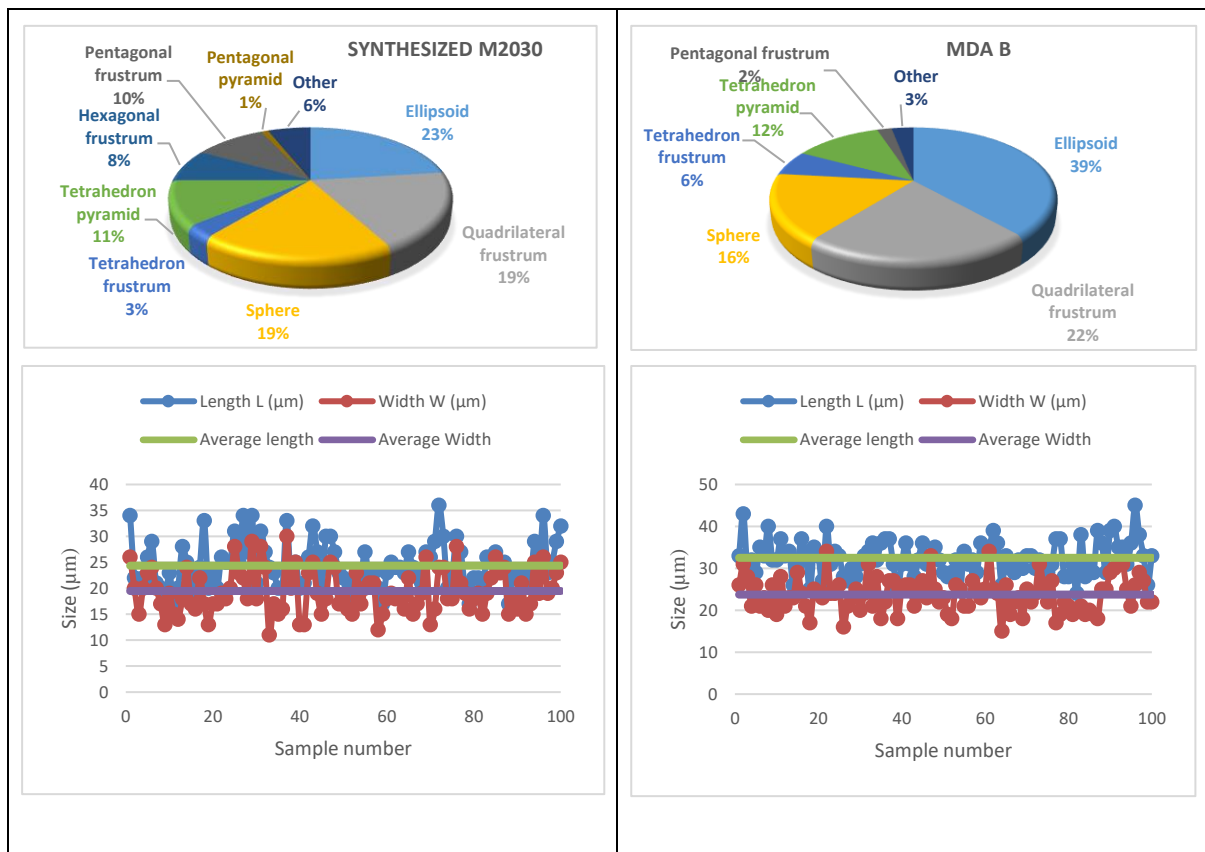
Figure 3-2: Leica images (a) synthesized M2030, (b) synthesized M 4060 (c) CDA M1530, (d) MDA M0510, (e) MDA M1225, (f) MDA B, (g) MDA A, (h) MDA C, (i) PD M0510

### 3.2.3 Grit shape and size distribution of loose abrasives

The randomly captured geometry characteristics are visually extracted to determine dominant shapes by conducting quantitative classification analysis of each grit. The dominant shapes distribution in each type of grit sample and its size distribution are presented in Figure 3-3. It can be seen that only a few types of geometrical shapes are dominant; ellipsoid, sphere, quadrilateral (pyramid, frustrum) and tetrahedron (pyramid or frustrum) shapes are among the

most prevailing ones. Hence, from this shape distribution the initial classification of 21 different geometries could fall down into only 5 or 6 geometries and therefore few of them are sufficient to specify the grit's shape.

The absolute values of maximum and mean in length and width bands and their size distribution of the samples are also illustrated in Figure 3-3.



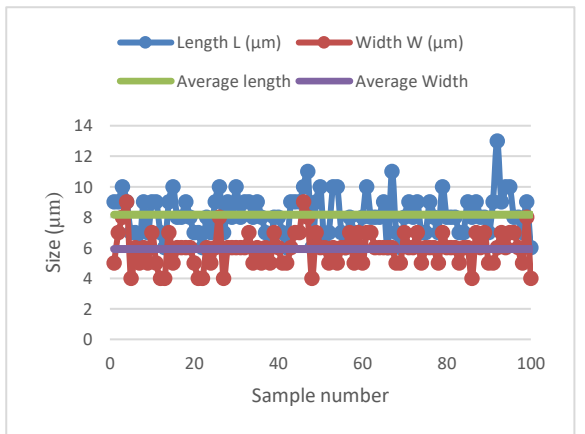
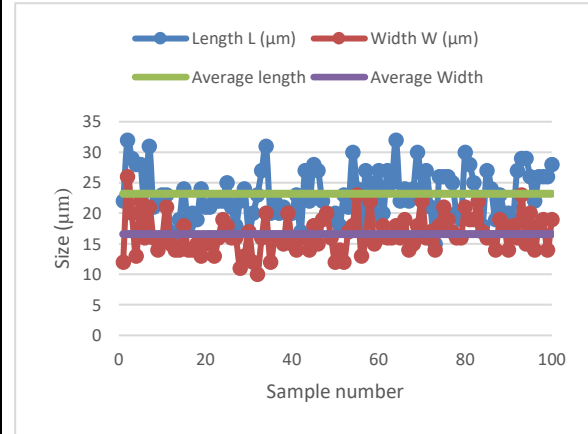
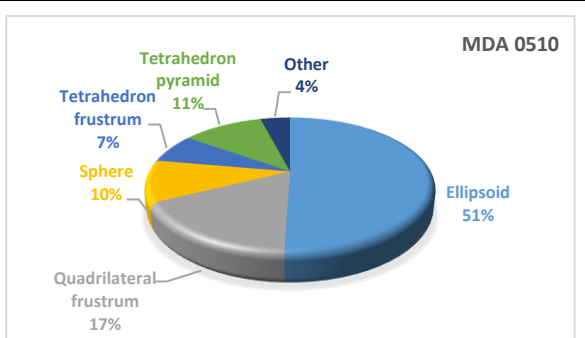
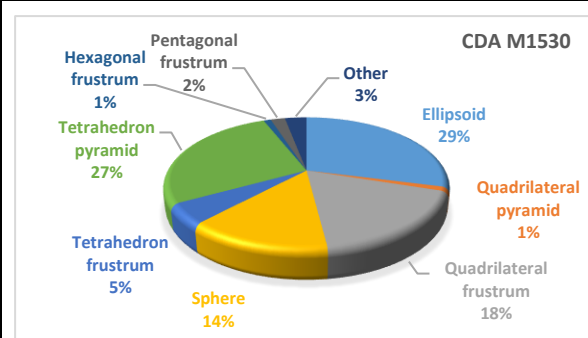
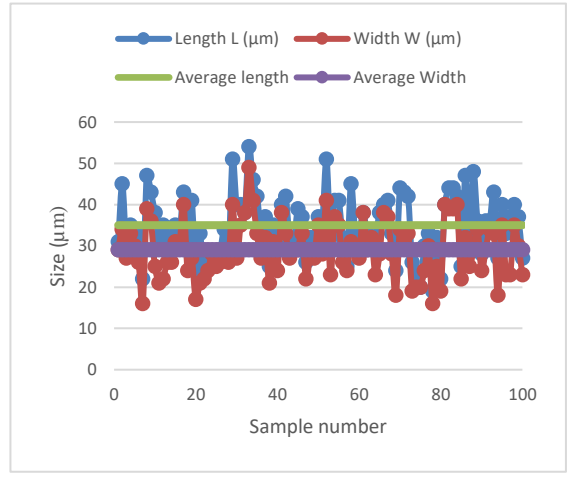
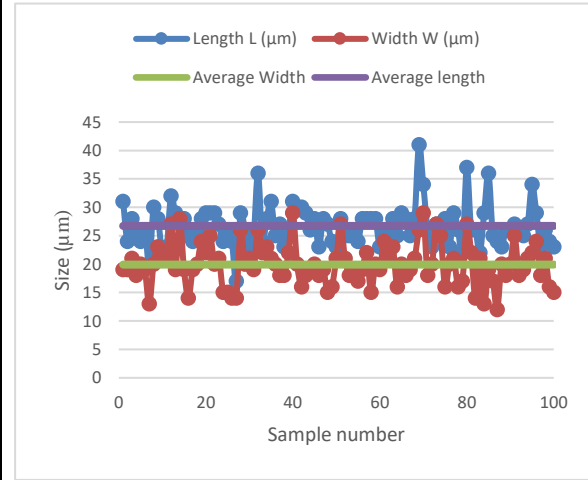
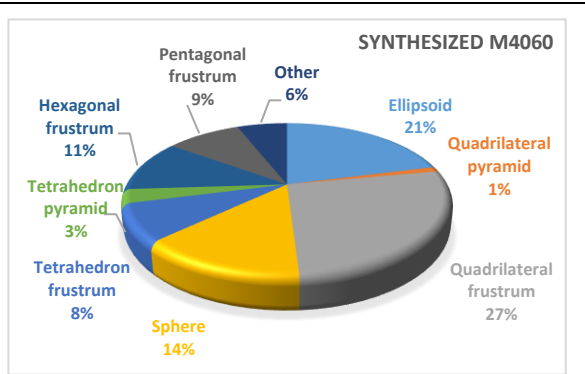
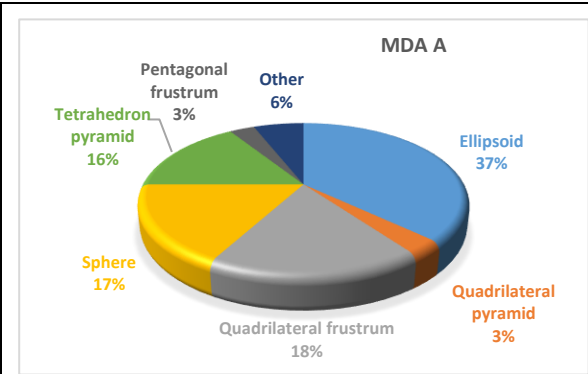




Figure 3-3: Grit shape and size distribution for nine diamond abrasives samples

### 3.2.4 Aspect ratio

A list of shape factors and measurements are mentioned in the literature and amongst them there is: the area, circular equivalent diameter, Feret's diameter major and minor axes, aspect ratio, convexity and circularity [19], For this study the focus is only on the aspect ratio (AR) defined as the width (W) to the length (L) of the grit. The length is considered here as the maximum distance between any two points on the perimeter of the grit parallel to the major axis. Similarly, the width is the maximum distance between any two points on the perimeter of the grit parallel to the minor axis. The length and width are represented in Figure 3-4. Aspect ratio is also an indication of grit shapes on abrasives. Basically, grit shape addresses the whole scenario between sharpness and bluntness of grits. Aspect ratio gives an idea about elongation of abrasive grits. Aspect ratio is a useful parameter for describing grit elongation. The abrasive grains in a grinding wheel are randomly formed and shaped in manufacturing and come in different aspect ratios. A blocky (high aspect ratio) grain will generally be far stronger than an angular, sharp-cornered grain [100].

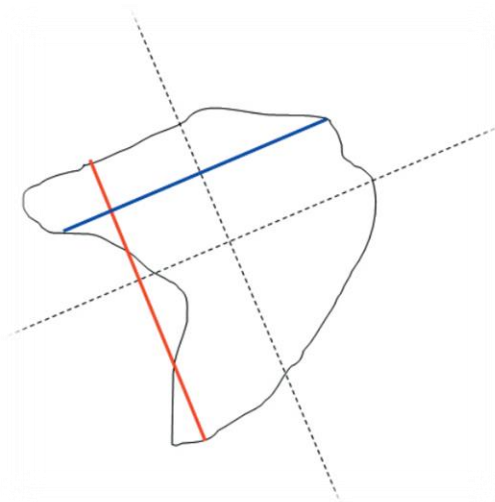


Figure 3-4: Major and minor axes (dashed lines), length (red) and width (blue)

### 3.2.5 Aspect ratio distribution

As an important index of morphological characteristics to indicate random distribution from measurement tests in industry, the variable  $x_i$  is defined as the AR of the width  $w_i$  to the length  $L_i$  of each abrasive grit, depicted as:

$$x_i = \frac{W_i}{L_i} \quad (3-1)$$

The mean of AR is calculated as

$$\bar{x} = \sum_{i=1}^n \frac{x_i}{n} \quad (3-2)$$

Where n is total number of the grits.

The standard deviation  $\sigma$  of the AR distribution defined to depict how all data of the grits AR are spread out from the mean, calculated by

$$\sigma = \sqrt{\sum_{i=1}^n \frac{(x_i - \bar{x})^2}{n}} \quad (3-3)$$

The AR distribution of each of the nine samples is shown in Figure 3-5. By means of this method the shape and variation of abrasive distribution could be assessed for the conformance of production. The tighter the AR distribution of the grits, the greater the conformance of production is. The AR distribution would be approximated as a Gaussian distribution which expected value is set to the mean of the AR and the probability density function is defined as [101]

$$f(x) = \frac{1}{\sqrt{2\pi}\sigma} e^{-\frac{(x_i - \bar{x})^2}{2\sigma^2}} \quad (3-4)$$

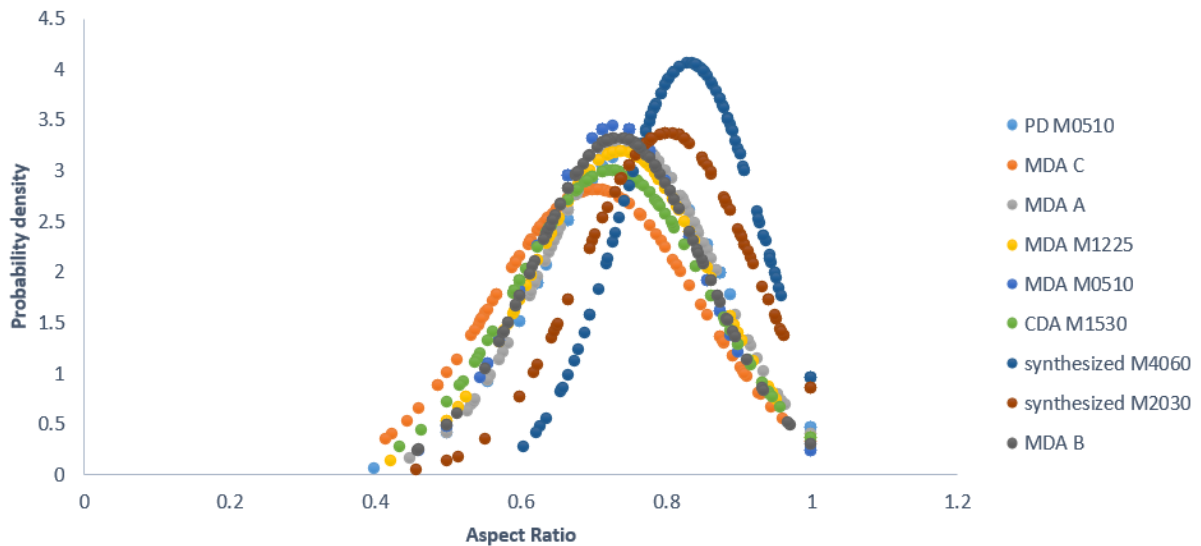


Figure 3-5: Aspect ratio distribution for the group of nine samples of loose abrasives

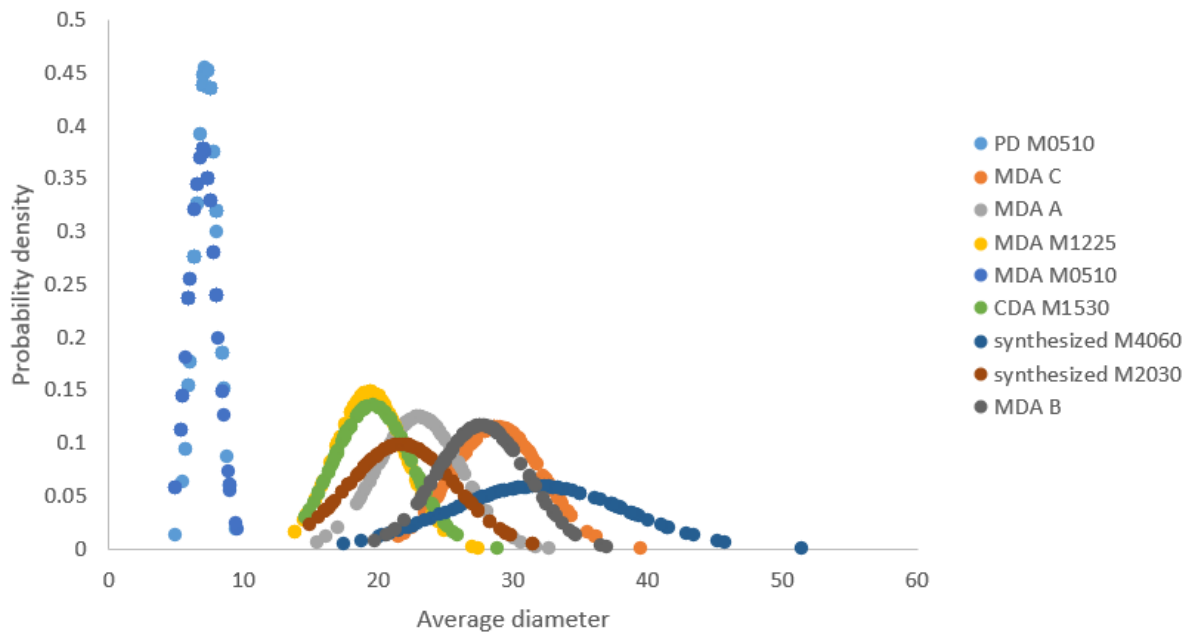


Figure 3-6: Average diameter distribution for the group of nine samples of loose abrasives

To describe the dispersion in the shape factor, namely AR, a statistical analysis applying average values, standard deviation and a probability density function is realised. The Table 3-3 shows the results obtained. Furthermore, the higher standard deviation ( $\sigma$ ) value is, the wider the AR values scatter and the higher the random variation. Per contra, the narrower distribution of the AR values does not necessarily imply less variation of the morphological geometries within the size range of the grits.

It is observed that the two synthesized diamond abrasive samples, synthesized M4060,

synthesized M2030, are presenting with a narrow distribution ( $\sigma = 0.15$  for the first sample and  $\sigma = 0,22$  for the second sample) and of a higher aspect ratio (Mean AR = 0.84 for the first and Mean AR = 0.81 for the second). In fact, in these two groups of abrasives more morphological types of grits are present than in the other groups as was illustrated in Figure 3-3. Nine different morphologies were counted for each of these two samples while for the other samples less than nine were counted. In contrast, the remaining samples have a broader distribution of lower aspect ratio, though the proportion of abrasive grits' AR values could reveal quality satisfaction of abrasive production. This illustrates the significance of the 3D morphological features in providing a rational guidance to enhance expertise for abrasive tools. Although the signification in the dispersion of the shape factor, AR, values might reflect the real dispersion of the grits shape composing the samples, this dispersion may also be affected by the procedure which considers only two-dimensional projection of the grits. A single grit could have different orientation positions and hence induce different two-dimensional projections and consequently different AR values.

*Table 3-3: Description of statistic measurements associated to the distribution of Aspect Ratio*

<i>Abrasive sample</i>	<i>Probability density of AR</i>	<i>Standard deviation (<math>\sigma</math>) of AR</i>	<i>Mean of AR</i>
<i>MDA M0510</i>	<i>3.43</i>	<i>0.23</i>	<i>0.73</i>
<i>MDA M1225</i>	<i>3.18</i>	<i>0.26</i>	<i>0.74</i>
<i>MDA A</i>	<i>3.24</i>	<i>0.24</i>	<i>0.75</i>
<i>MDA B</i>	<i>3.31</i>	<i>0.24</i>	<i>0.74</i>
<i>MDA C</i>	<i>2.81</i>	<i>0.31</i>	<i>0.71</i>
<i>CDA M1530</i>	<i>2.99</i>	<i>0.27</i>	<i>0.73</i>
<i>PD M0510</i>	<i>3.15</i>	<i>0.25</i>	<i>0.75</i>
<i>Synthesized M2030</i>	<i>3.36</i>	<i>0.22</i>	<i>0.81</i>
<i>Synthesized M4060</i>	<i>4.04</i>	<i>0.15</i>	<i>0.84</i>

### **3.3 Assessment of bonded abrasives**

In this project, five different cutting tools were planned for use in experimental scratching tests. In each tool a different diamond abrasive was bonded to its extremity (cf. Figure 3-7). In this section, the characterisation of these bonded abrasives in terms of dominant shapes distribution is reported. The analysis of the grit shapes was carried out by observing bonded diamond

abrasive grits under an SEM microscope, because the resolution observed in SEM images is significantly better as compared to the Leica images.

The five abrasives utilised are as below:

- MDA A (A)
- MDA B (B)
- MDA C (C)
- Synthesized M 2030 (D)
- CDA M 2030 (E)

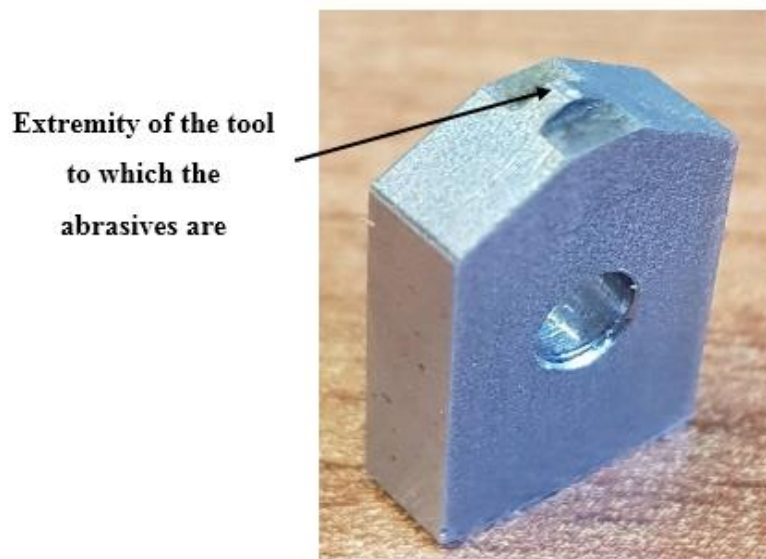
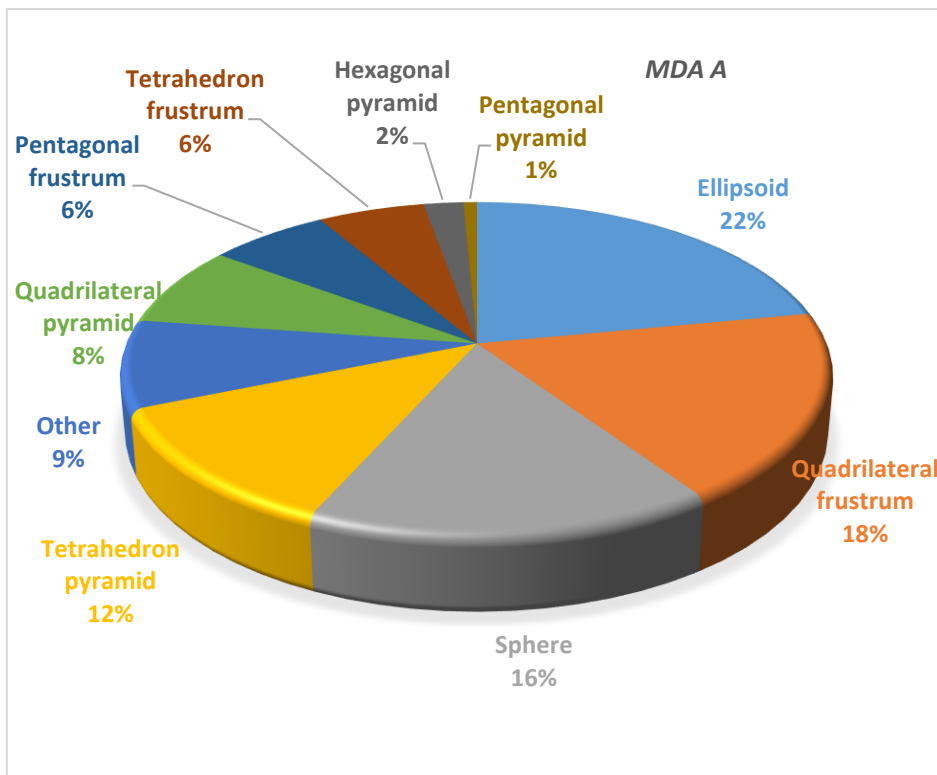
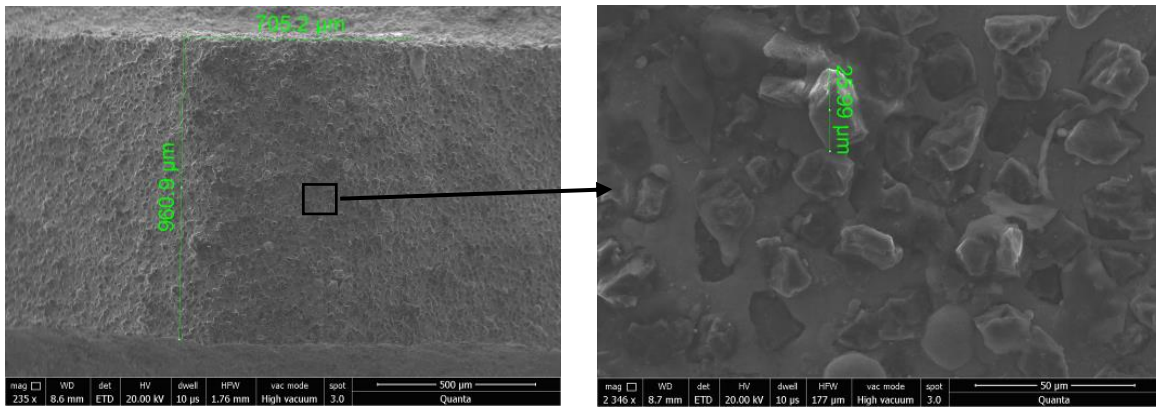


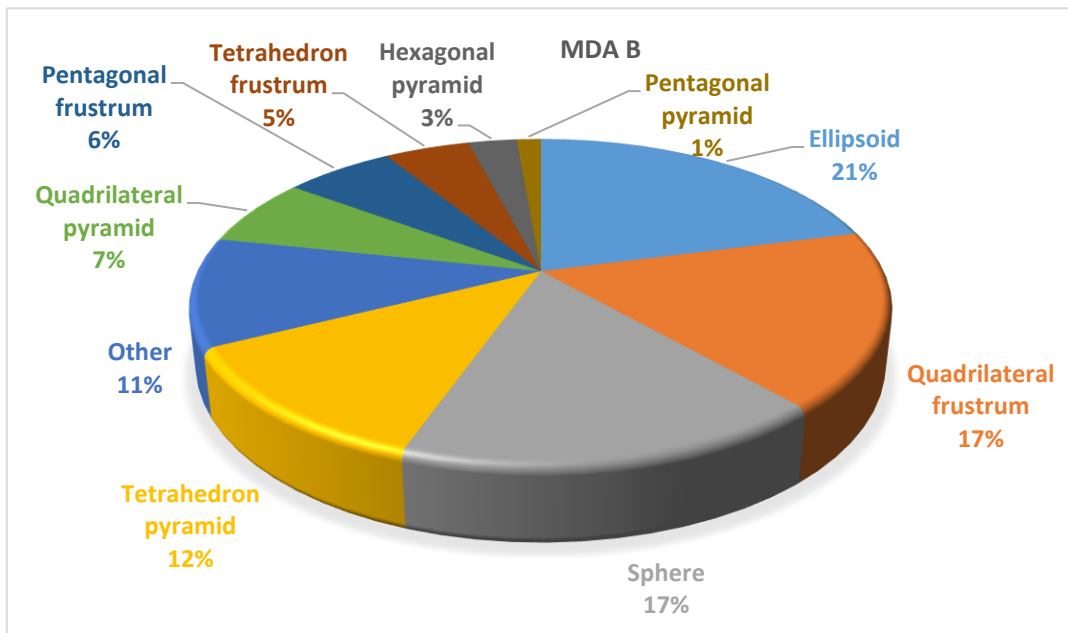
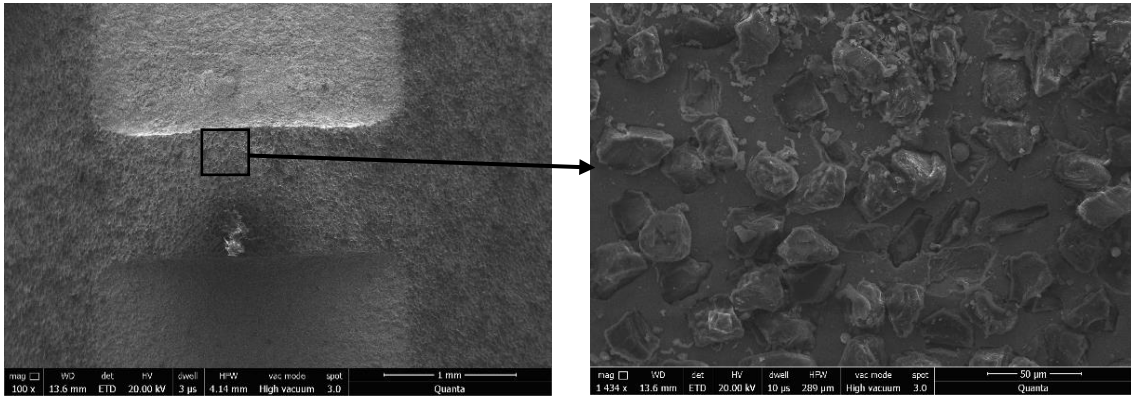
*Figure 3-7: Cutting tool with bonded abrasives*

The dominant shapes in each type of the bonded grits are presented using a pie chart as is shown in Figure 3-8. It can be seen that only a few types of geometrical shapes are dominant; ellipsoid, sphere, quadrilateral (pyramid, frustrum) and tetrahedron (pyramid or frustrum) shapes are among the most prevailing ones. Hence, from this shape distribution the initial classification of 21 different geometries could fall down into only 5 or 6 geometries and therefore few of them are sufficient to specify the grits' shapes.

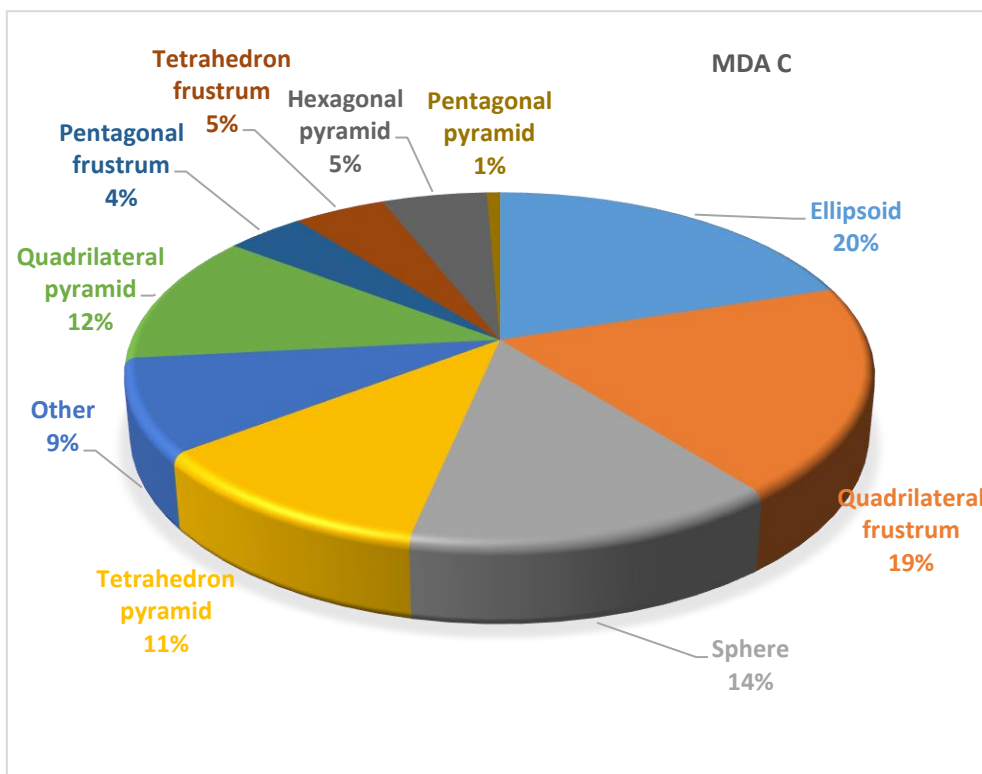
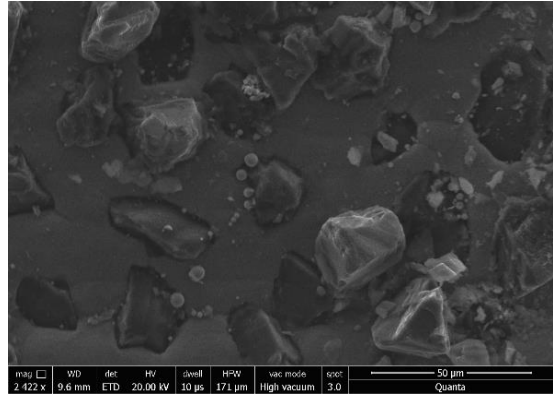
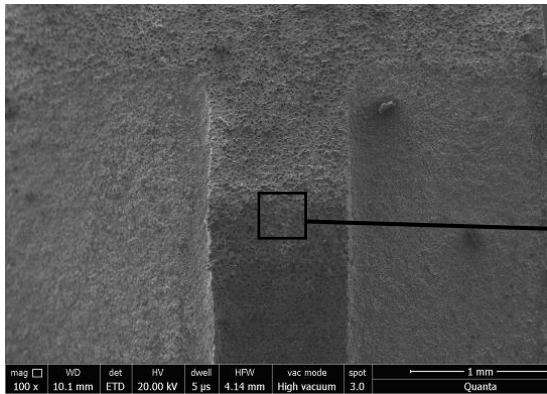
MDA A



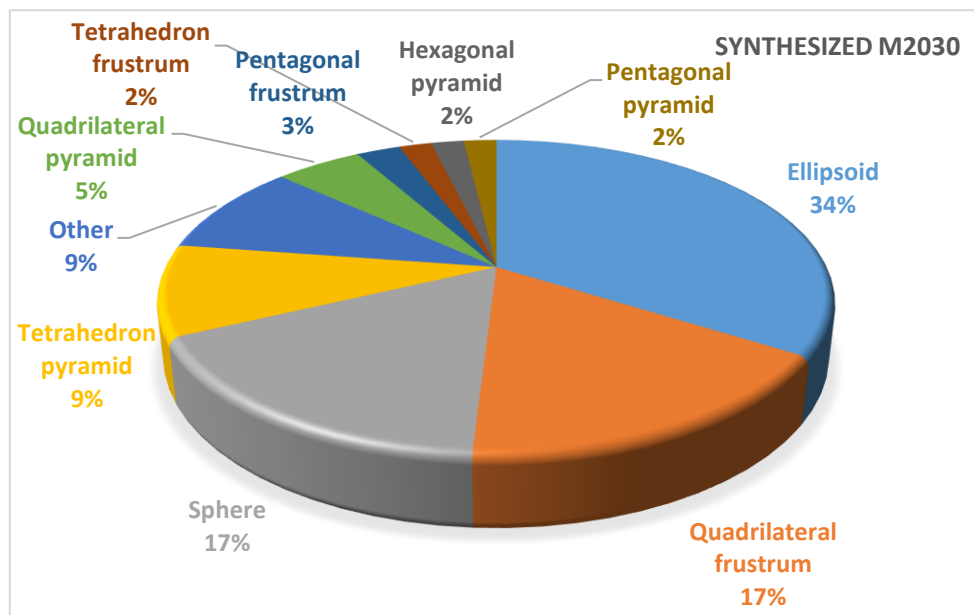
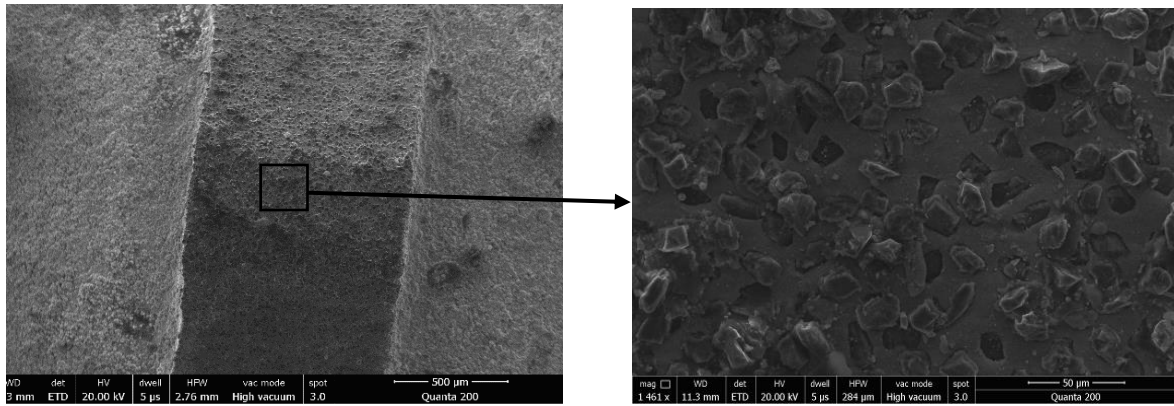
MDA B



MDA C



Synthesized M 2030



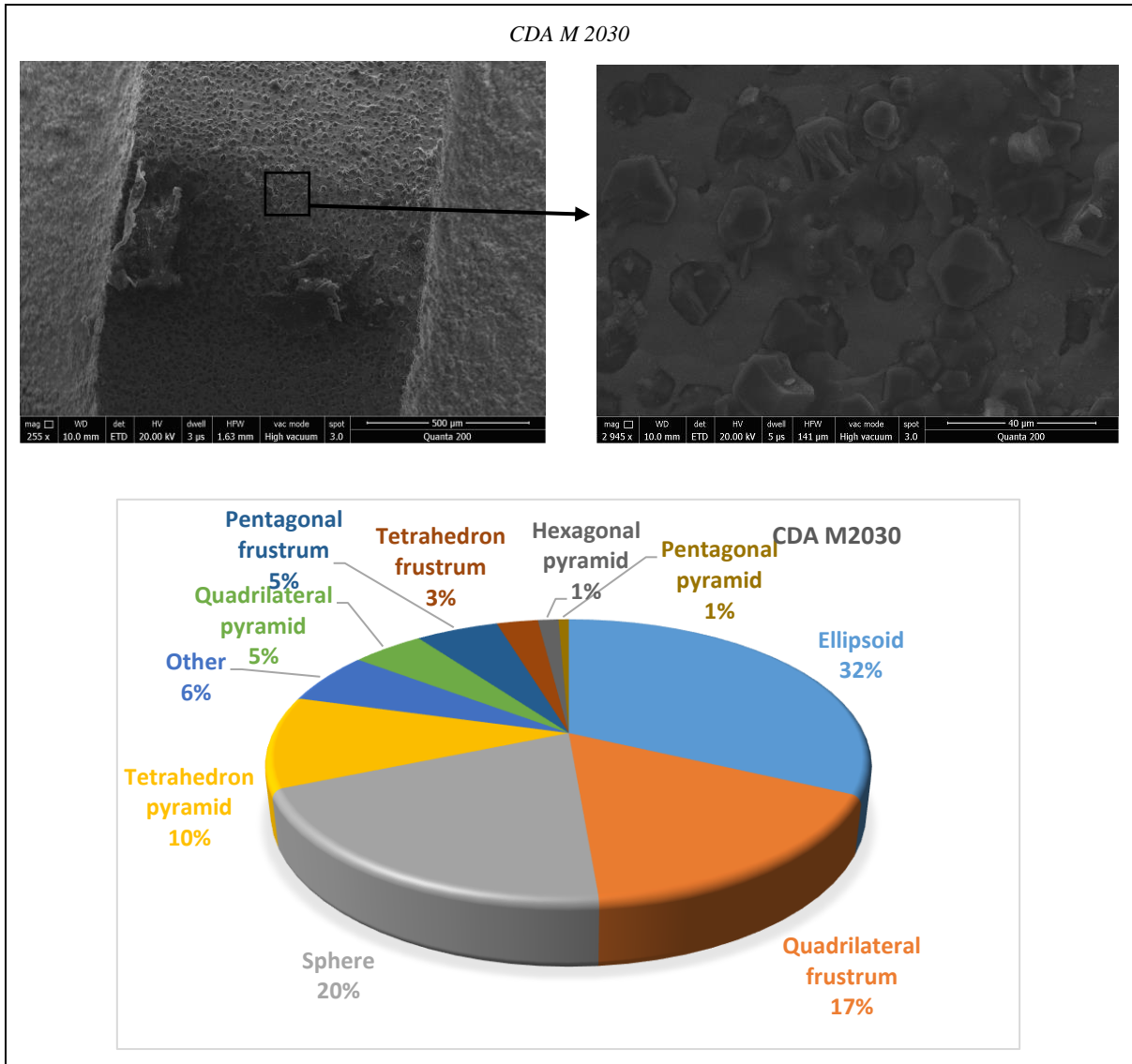


Figure 3-8: Shape distribution of five different abrasives bonded to cutting tools

The previous classification of the grit morphology involves many different groups of shapes and making analysis based on this classification is still not obvious. It is for this reason that making a simplified classification in order to develop a reasonable force model based on limited number of shape categories is more suitable. Figure 3-9 shows the main dominant abrasive shapes. It can be observed that six shape categories are most dominant ones. These shapes are ellipsoid with about 20% in each abrasive but with higher percentage in the abrasives “D” and “E”. Sphere with about 15% in each abrasive. Quadrilateral frustrum with about 15% in each abrasive. Quadrilateral pyramid with about 5% to 10% in each abrasive. Tetrahedron pyramid with about 10% in each abrasive. And finally, the shape category “other” with about 5 to 10% in each abrasive.

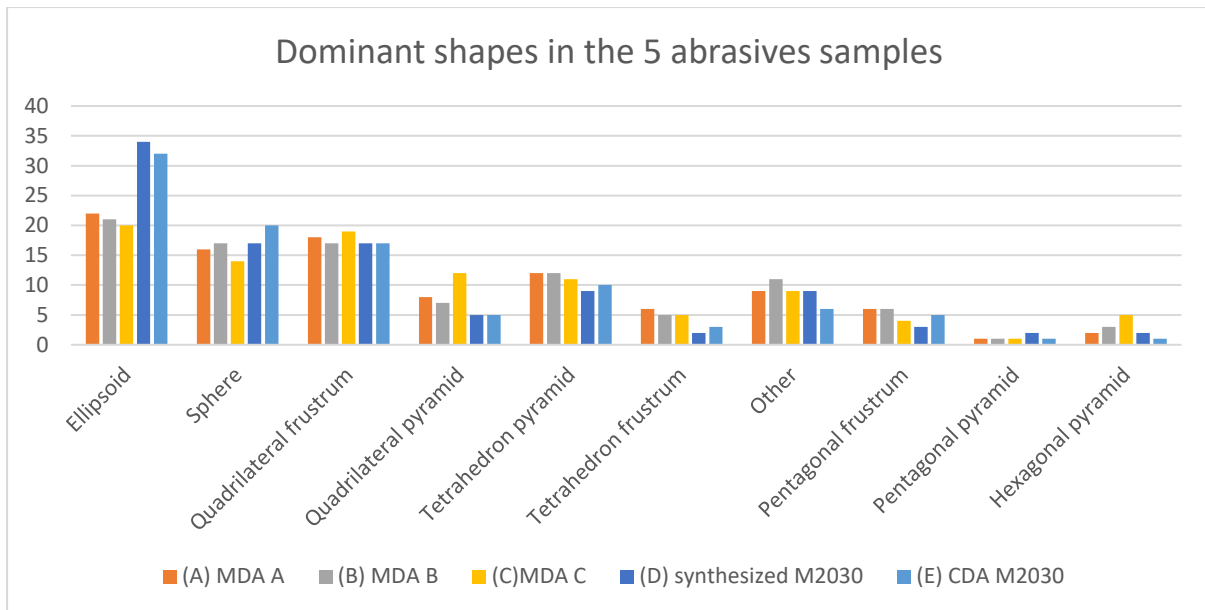


Figure 3-9: Dominant shapes in the five abrasives samples

For the modelling considerations, the precedent shape distribution is reconsidered and reduced into only three groups. The ellipse and the sphere shapes could be considered as rounded shapes and hence could be combined into one category, which make this category counts for almost half of the dominant shapes. Similarly, pyramidal shapes grouping tetrahedrons pyramids, quadrilateral pyramids pentagonal pyramids and hexagonal pyramid could be considered as shapes with sharp edges and are combined into one shape category. Finally, truncated pyramidal shapes containing the frustrum shapes (tetrahedron frustrum, quadrilateral frustrum, and pentagonal frustrum) could be considered as shapes with flat edges and are combined into one shape category. All the remaining shapes that are not sorted in one of these three categories are grouped in shape category as “other shapes”. This category is not considered later on this study as its proportion is much lower compared to the three main groups selected.

The proportions of the rounded, the pyramidal and the truncated pyramidal shapes in each of the five abrasives are shown in Table 3-4.

Table 3-4: Classification of the abrasive shapes into three main dominant shapes and their proportions

<i>Abrasive</i>	<i>Rounded shape proportion (%)</i>	<i>Pyramidal shape proportion (%)</i>	<i>Truncated pyramidal shape proportion (%)</i>	<i>Other shapes proportion (%)</i>
<i>A</i>	38	23	30	9
<i>B</i>	38	23	28	11
<i>C</i>	34	29	28	9
<i>D</i>	51	18	22	9
<i>E</i>	52	17	25	6

### 3.4 Abrasive assessment on diamond wire saw

In this section, the characterisation of three diamond wires regarding shape distribution is also reported. The analysis of the grit shapes was carried out by observing diamond wires under an SEM microscope.

The three wires utilised are as below:

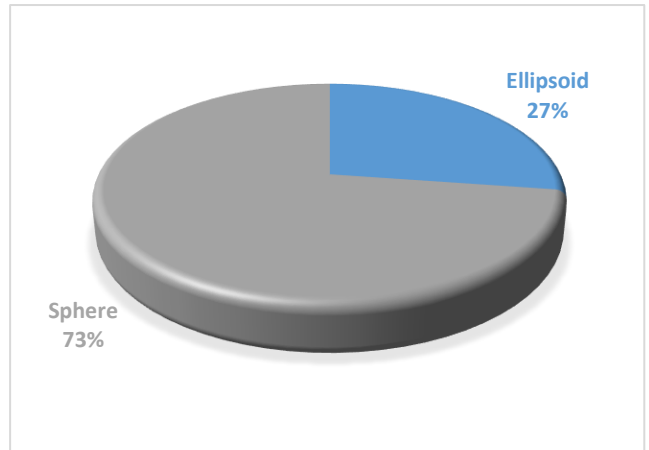
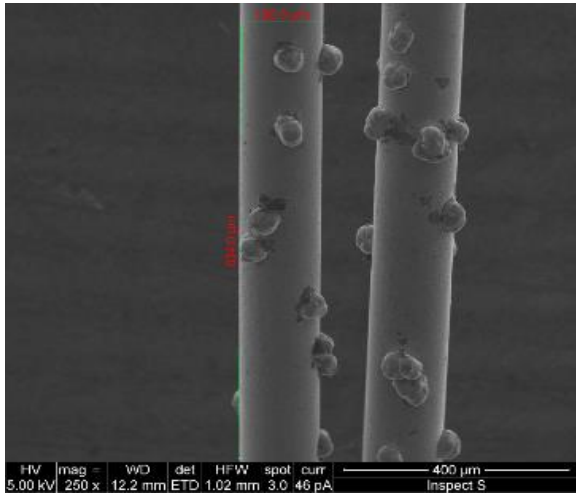
- Wire with 30 – 40  $\mu\text{m}$  grit's size
- Wire with 10 – 20  $\mu\text{m}$  grit's size
- Wire with 8 – 16  $\mu\text{m}$  grit's size

The three wires with their shape distribution are shown in Figure 3-10. In addition, the proportion of the rounded, the pyramidal and the truncated pyramidal shapes in each of the three wires are shown in Table 3-5.

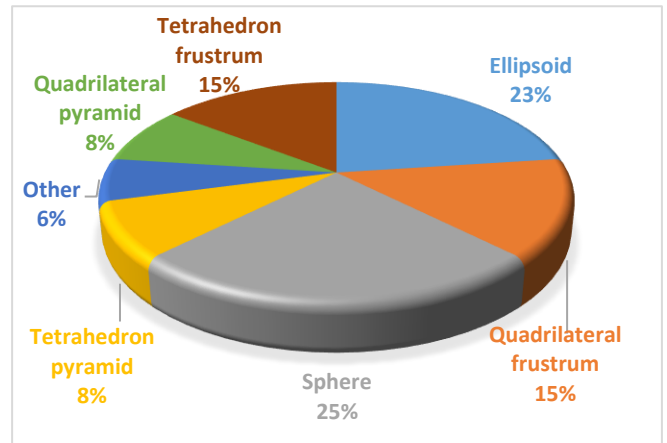
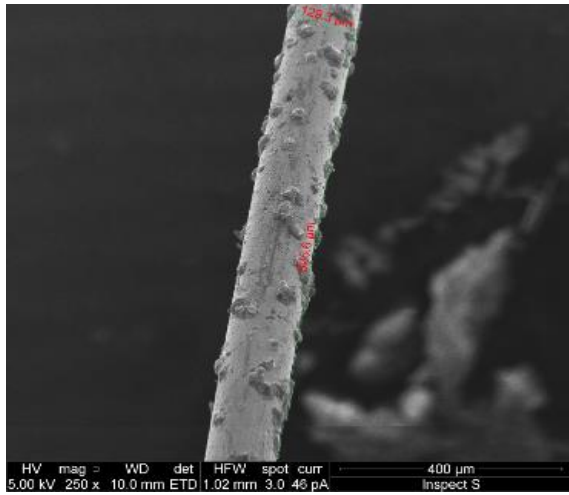
Table 3-5: Geometrical grit shapes proportion in each wire and the associated total measured force

<i>Wire saw</i>	<i>Rounded shape proportion (%)</i>	<i>Pyramidal shape proportion (%)</i>	<i>Truncated pyramidal shape proportions (%)</i>	<i>Other shapes proportion (%)</i>
<i>30 40 wire</i>	74	0	26	0
<i>10 20 wire</i>	48	16	30	6
<i>8 16 wire</i>	68	6	26	0

Wire with 30 – 40 μm grit's size



Wire with 10 – 20 μm grit's size



Wire with 8 – 16 μm grit's size

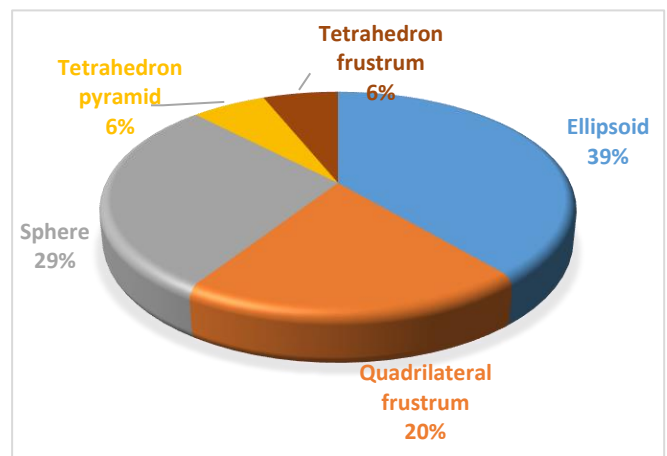
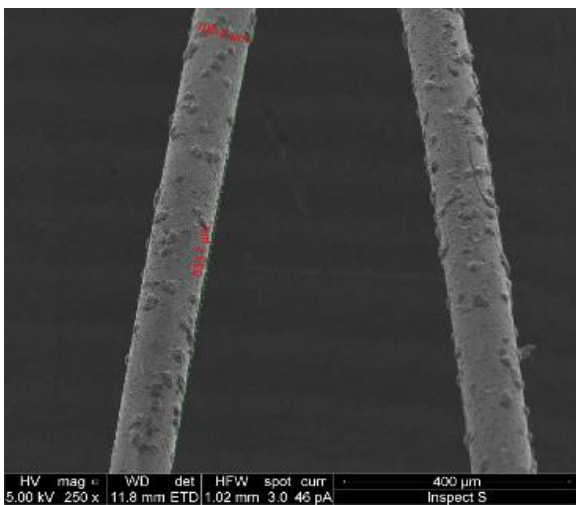


Figure 3-10: Shape distribution on the three diamond wires

### **3.5 Summary**

Aiming at the development of new test methods for micron diamond processing assessments, loose diamond abrasives, bonded diamond abrasives and wire saw diamond have been characterised in terms of grit morphology and shape. Twenty-one basic geometrical figures were considered as a common base for grit shape identification and the grits were classified according to their morphology with acceptable similarity. Through image analysis, it was found that only a few types of grit geometries dominate the grit population. These dominant shapes are ellipsoid, sphere, quadrilateral frustrum, quadrilateral pyramid and tetrahedron pyramid. Considering the contact point between the grit and the workpiece during the grinding process, the shape classification groups fall down into only three main groups: rounded shapes, pyramidal shapes and truncated pyramidal shapes.

## Chapter 4 **Theoretical model of abrasive machining mechanics**

### **4.1 Introduction**

Cutting brittle materials is a very challenging process in a way that brittle materials are known to be fragile and tend to be fractured easily. The shape of the abrasive grits is considered as an influential parameter in the grinding process. Each engaged active grit, which are of random nature of distribution and orientation, affects the grinding forces. The grinding process efficiency is generally dependent upon the effectiveness of individual grain cutting. Though, it is essential that the grain has favourable cutting geometry to make every grain perform with full capability. The improvement in the cutting abilities and reduction of the wheel wear is possible because of the categorization of grain shape by applying the specific shape to different tasks [102].

In this chapter, the influence of grit shape on grinding force and stress is analysed by using the finite element method (FEM). FEM is a useful approach to characterise the interaction mechanism on the cutting tool and the workpiece. This method is also able to determine and predict cutting behaviour during the process such as cutting forces, stresses and strains.

The objective of this work is to calculate the stress distribution in a Sapphire material by applying normal and tangential forces imposed through single abrasive grit. A simplified geometrical model of the abrasive grits is proposed here based on the classification established in Chapter 3, i.e. spherical, pyramidal and truncated pyramid. The abrasive grit is gradually imposing a force onto the workpiece; a stress is then generated in the contact region caused by the abrasive grit. The cutting force is calculated once the maximum stress reaches the maximum material strength at a given cutting depth.

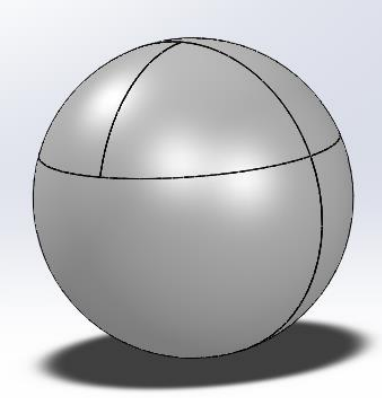
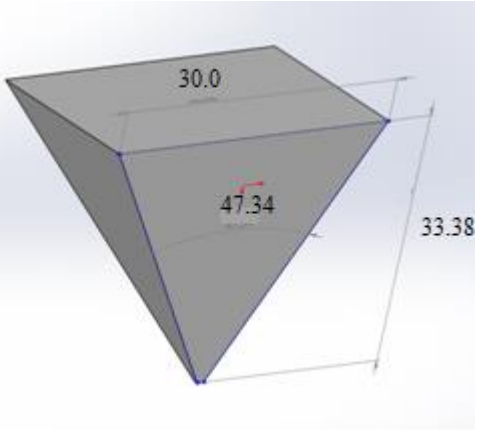
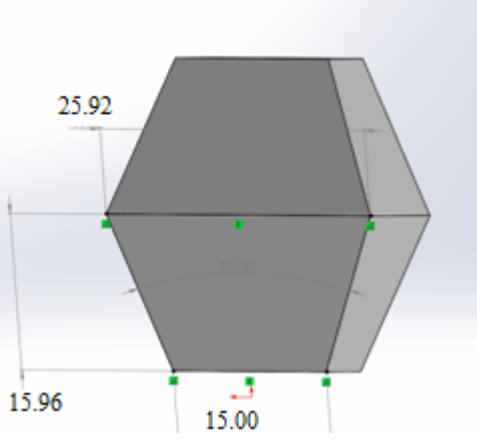
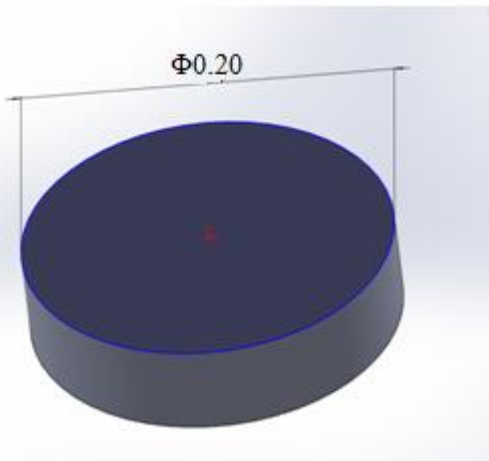
### **4.2 Grit geometry and workpiece design**

Abrasive grits are modelled as of three different shaped solid bodies: spherical, pyramidal and truncated pyramidal. Table 4-1 shows the grit's shapes and the dimensions considered in the design. As it was seen in Chapter 3, real abrasive grits might have various shapes; some might be sharp while others might be round or blunt. Thus, it is required to make assumptions to model the grit body. Albeit not entirely including all the possible geometries that could occur, the preference of selecting particular shapes of the abrasives consists on the necessity to vary their surface contact against the workpiece and to mimic the main possibilities that could

happen when the grit is engaged into the workpiece. Here, the spherical shape accounts for the rounded grits, the pyramidal shape represents the sharp grits and the truncated pyramidal shape imitates the blunt grits. The base shape of pyramid and truncated pyramid is considered here as a square base. The reason for that is that most cutting cases can be simplified as one or two rake faces engaged in the cutting, and also because the average apex angle of triangle (60 degree), quadrilateral (90 degree), pentagon (108 degree) and hexagon (120 degree) is 94.5 degree that is similar to that of square.

The size of the modelled grits used in the simulations was relatively similar to that of the abrasive grits used in the experimental tests.

Table 4-1: Workpiece and grit shapes modelled in SolidWorks

<p style="text-align: center;"><i>Spherical, <math>\phi=30\mu\text{m}</math></i></p> 	<p style="text-align: center;"><i>Pyramidal</i></p> 
<p style="text-align: center;"><i>Truncated</i></p> 	<p style="text-align: center;"><i>Workpiece</i></p> 

### 4.3 Workpiece material and properties

The material workpiece utilised for this analysis is Sapphire, which is a popular ceramic well known for its excellent optical performance and superior properties in mechanical, thermal, chemical stability at high temperature. And the abrasive grit material is diamond, which has the highest hardness and thermal conductivity. These properties are highly appreciated in major industrial applications such as cutting and polishing. The properties of the two materials are taken from published literature and are listed in the Table 4-2 below.

Table 4-2: Material properties

<i>property</i>	<i>Material</i>	
	<i>Sapphire<sup>1</sup></i>	<i>Diamond [103]</i>
<i>Young's modulus E (GPa)</i>	<i>345</i>	<i>1050</i>
<i>Poisson's ratio</i>	<i>0.28</i>	<i>0.07</i>
<i>Shear modulus (GPa)</i>	<i>145</i>	<i>318</i>
<i>Mass density (g.cm<sup>-3</sup>)</i>	<i>3.98</i>	<i>3.51</i>
<i>Tensile strength (MPa)</i>	<i>400</i>	<i>9000</i>
<i>Yield strength (MPa)</i>	<i>400</i>	<i>9000</i>
<i>Hardness (GPa)</i>	<i>18-22</i>	<i>80-100</i>
<i>Fracture Toughness (MPa-m<sup>1/2</sup>)</i>	<i>1.4</i>	<i>3.40</i>

<sup>1</sup> <http://www.matweb.com>

### 4.4 Materials and elastic-plastic behaviour

Elastic-plastic material behaviour during the single grit indentation simulation is governed by yield stress-strain curve (Figure 4-1). Material hardening was assumed to be isotropic. Stress  $\sigma$ , is a measure of the force per unit area acting on a plane passing through the point of interest in a body. The stress is, at the initial stage, directly proportional to the strains  $\epsilon$ . This is known as Hooke's Law:  $\sigma = E \epsilon$ , E is the elastic modulus of the material. The material considered for the simulation is a brittle material i.e. Sapphire, which in general shows little ability to deform plastically and hence will usually fracture at, or very near to, the elastic limit when subjected to tension. Therefore, it will not consider the plastic deformation in this model.

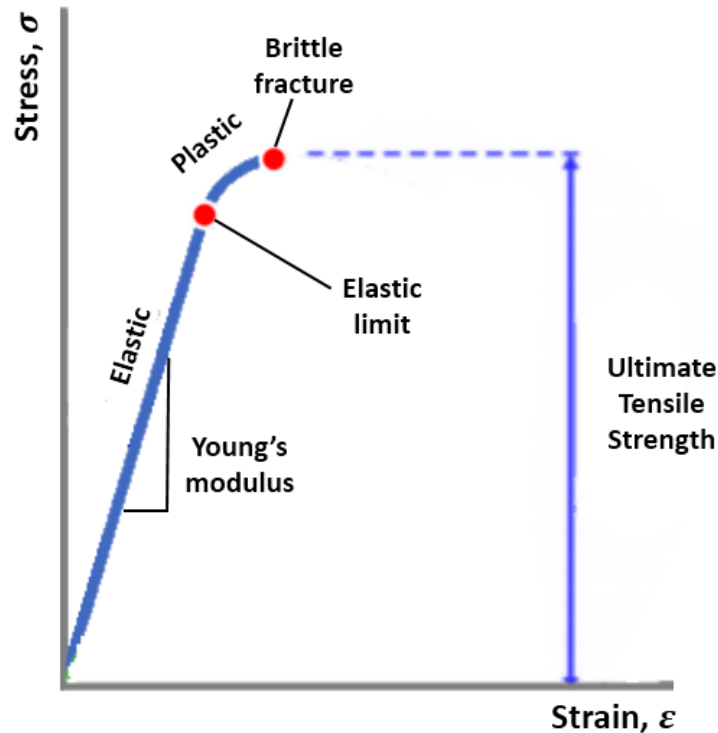


Figure 4-1: Stress-strain curve for brittle material illustrating elastic plastic behaviour and brittle fracture

## 4.5 Simulation approach

The model utilised here for the grit interaction with the workpiece is simplified by considering some assumptions regarding material deformation aspect throughout the simulation. Consequently, the single grit model reported here is only to examine elastic deformation. Different grit shapes, various depths (grit scratching depth into the workpiece, cf. Table 4-3) and different materials properties are considered in the simulations to inspect the influences on material deformation.

Finite element simulation in this thesis refers to simulation of single grit grinding at the micro scale, where the depth of cut is in order of few micrometres. This is not a straight-forward simulation. Actually, the simulation was done on SolidWorks environment and it is a process by manipulating abrasive scratching model. The cutting tool was constrained as a rigid body and the workpiece was fixed on the bottom. Both the single grit and the workpiece are meshed using a four-node linear tetrahedron element. A linear tetrahedral element is defined by four corner nodes connected by six straight edges. A finer mesh in the contact zone is required for the accuracy of the FEM analyses. Fine meshes over the contact area bring better conformity of contact between grit and workpiece. Coarse meshing may result in poor conformity of

simulation due to the relatively large stress gradients in the grinding contact zone.

Three-dimensional finite element model is established to investigate the effects of shapes of grit on the stress distribution on the surface contact of the workpiece.

The idea is to gradually increase imposed total force, where the ratio between normal and tangential force is 1.2, and calculating the generated stress in the contact region caused by the abrasive grit for different cutting depths (cf. Figure 4-2). The aim is to repeat the process until the maximum stress of the considered workpiece reaches the failure stress of the material. No damage model was used to allow element fracture, only elastic deformation. Commercially available 3D finite element program-SIMULATION of the SOLIDWORKS was used to analyse the stress in the material under static conditions.

Table 4-3: Applied cutting depth for each of the three shapes configuration of the simulation

Grit shape	Applied cutting depths ( $\mu\text{m}$ )
Spherical	0.5, 1, 1.5, 2
Pyramidal	0.5, 1, 1.5, 2
Truncated	0.5, 1, 1.5, 2

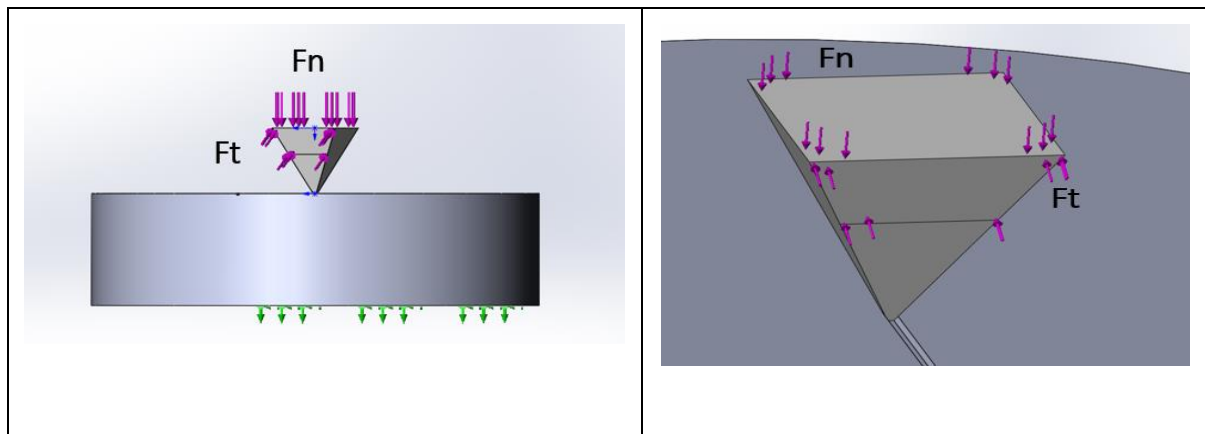


Figure 4-2: Workpiece and grit body (Pyramidal shape) modelled in SolidWorks

## 4.6 Simulation results and discussion

### 4.6.1 Stress and force analysis

The simulation results are reported in the tables and figures below Figure 4-3. Under the defined workload, the maximum stress was calculated for the three different grit shapes and

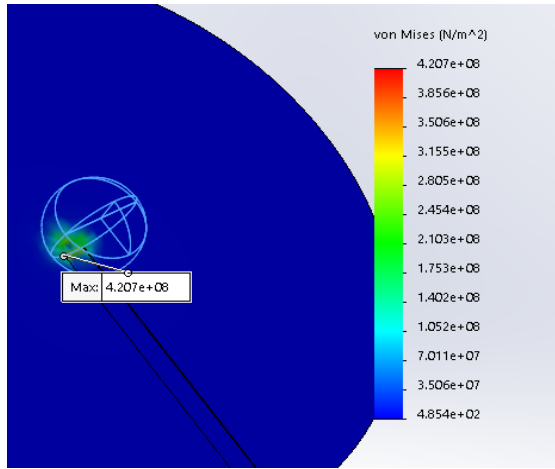
with four different cutting depths (0.5, 1, 1.5 and 2  $\mu\text{m}$ ) for each grit shape. It was found that the maximum stress occurred at different position in the contact region of the workpiece depending on the shape of the abrasive(cf. Figure 4-3). As the tensile limit strength for sapphire material is 400 MPa, any stress above this limit is supposed to lead to the occurrence of cracks and fractures on the workpiece material. For the spherical grit shape, it was found that for the cutting depths 0.5, 1, 1.5, and 2  $\mu\text{m}$ , the identified loads causes deformation stress to the workpiece were  $1.13 \times 10^{-3}$ ,  $2.79 \times 10^{-3}$ ,  $4.0 \times 10^{-3}$  and  $5.64 \times 10^{-3}$  N respectively. Similarly, for the pyramidal shape the cutting forces for the depth 0.5, 1, 1.5 and 2  $\mu\text{m}$  are  $5.74 \times 10^{-5}$ ,  $8.88 \times 10^{-5}$ ,  $23.6 \times 10^{-5}$  and  $43.4 \times 10^{-5}$  N respectively. While for the truncated grit shape, the cutting forces for the depth 0.5, 1, 1.5 and 2  $\mu\text{m}$  are  $1.56 \times 10^{-2}$ ,  $1.81 \times 10^{-2}$ ,  $2.30 \times 10^{-2}$  and  $2.52 \times 10^{-2}$  N. These forces were deduced from the linear regression equations obtained of the stress and force curves shown Figure 4-4, Figure 4-5 and Figure 4-6. The linear regression equation is in the form:

$$y = ax + b \quad (4-1)$$

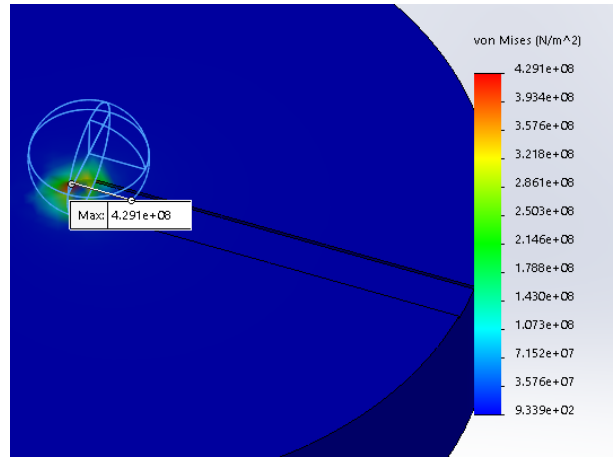
Where y represents the stress, x the force, *a* the slop and b the vertical intercept to the y axis. The force is then calculated from this equation considering the stress value as the ultimate limit strength of sapphire, which is 400 MPa.

Spherical

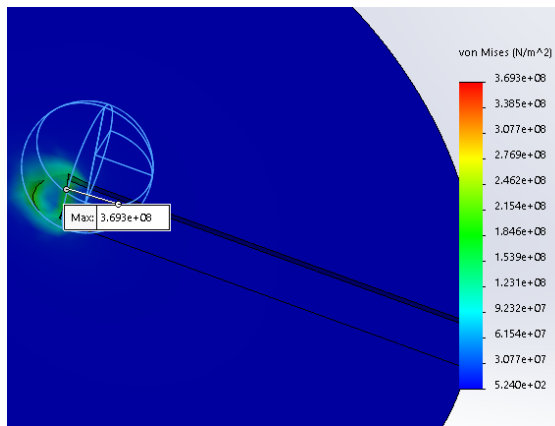
0.5  $\mu\text{m}$



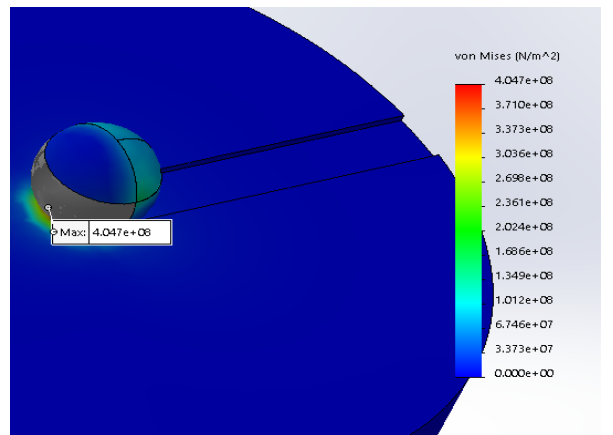
1  $\mu\text{m}$



1.5  $\mu\text{m}$

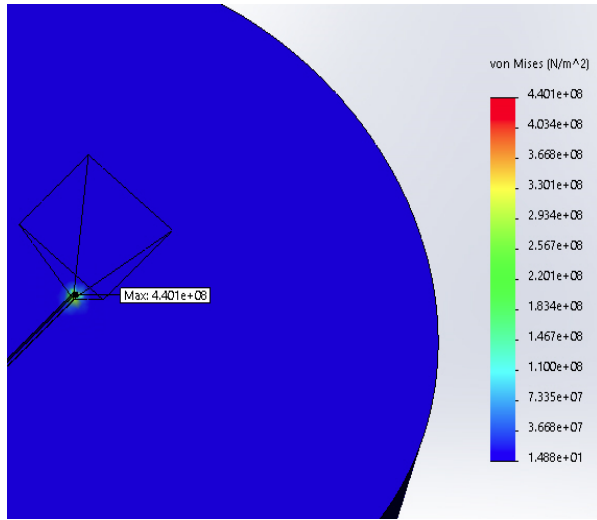


2  $\mu\text{m}$

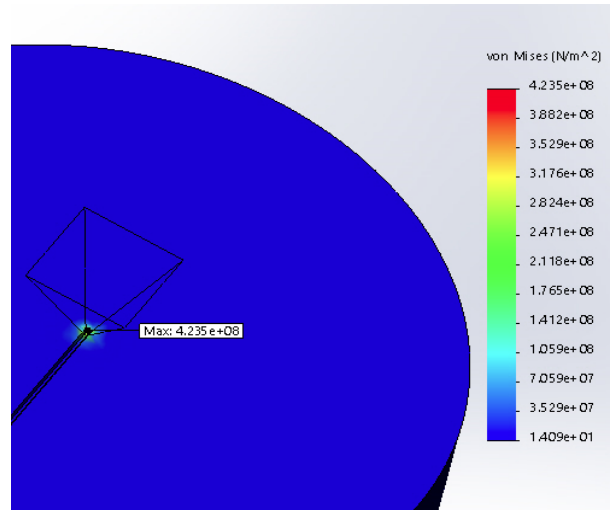


Pyramidal

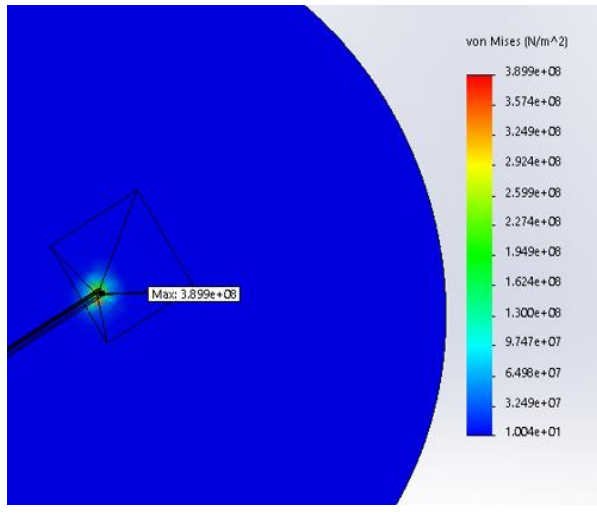
0.5  $\mu\text{m}$



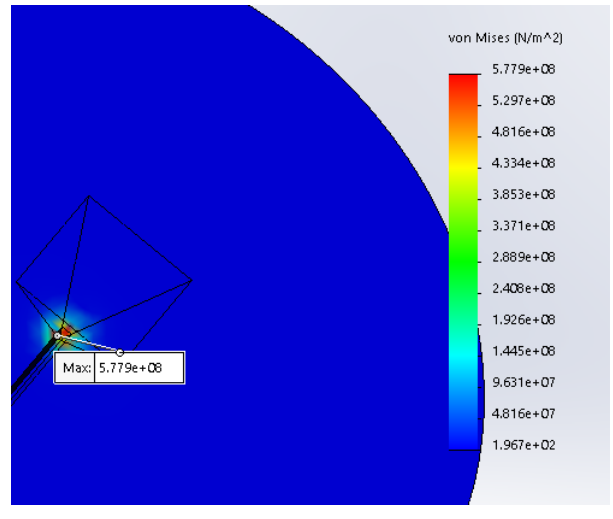
1  $\mu\text{m}$



1.5  $\mu\text{m}$



2  $\mu\text{m}$



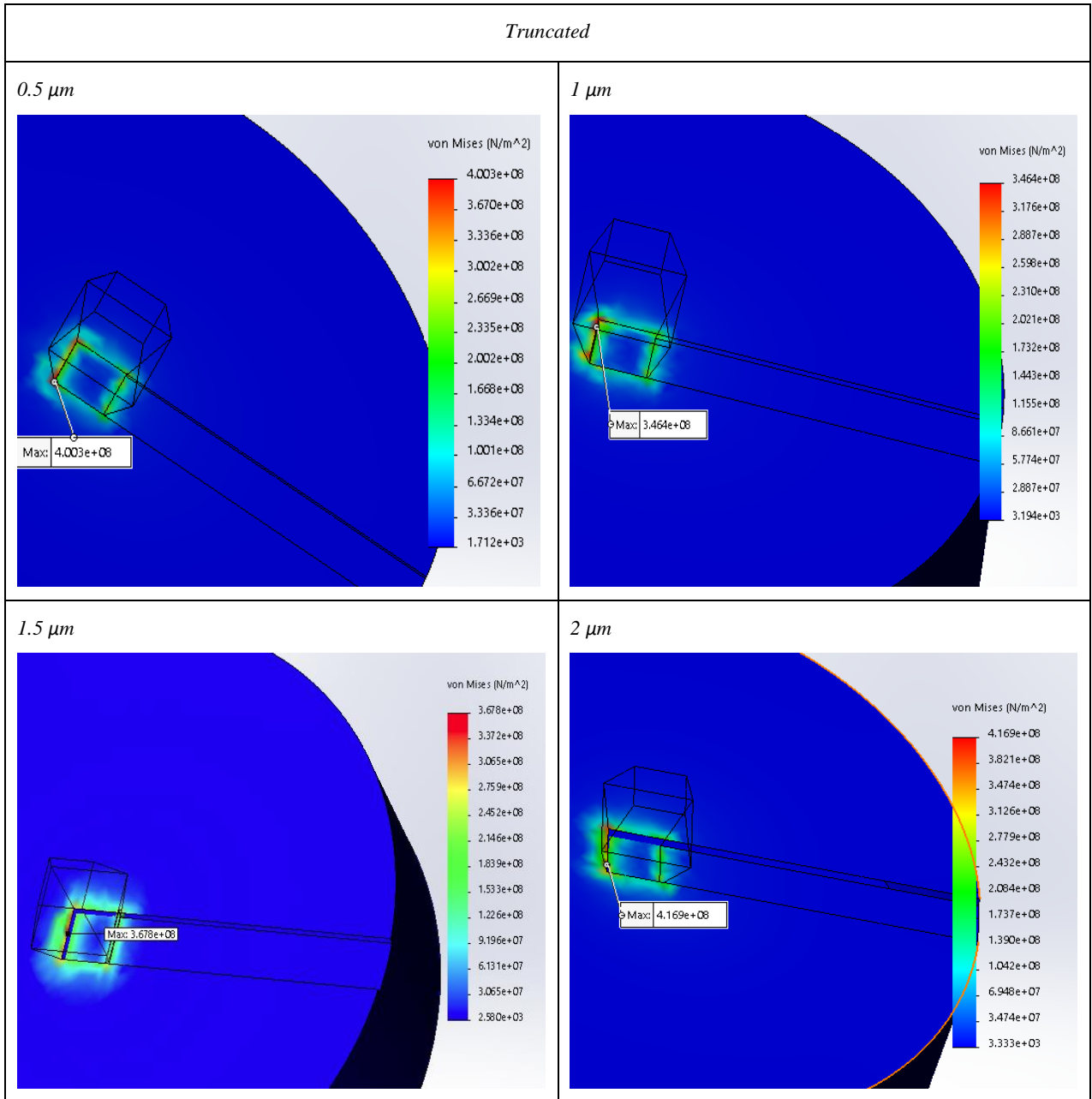


*Figure 4-3: Stress distribution for different grit shapes*

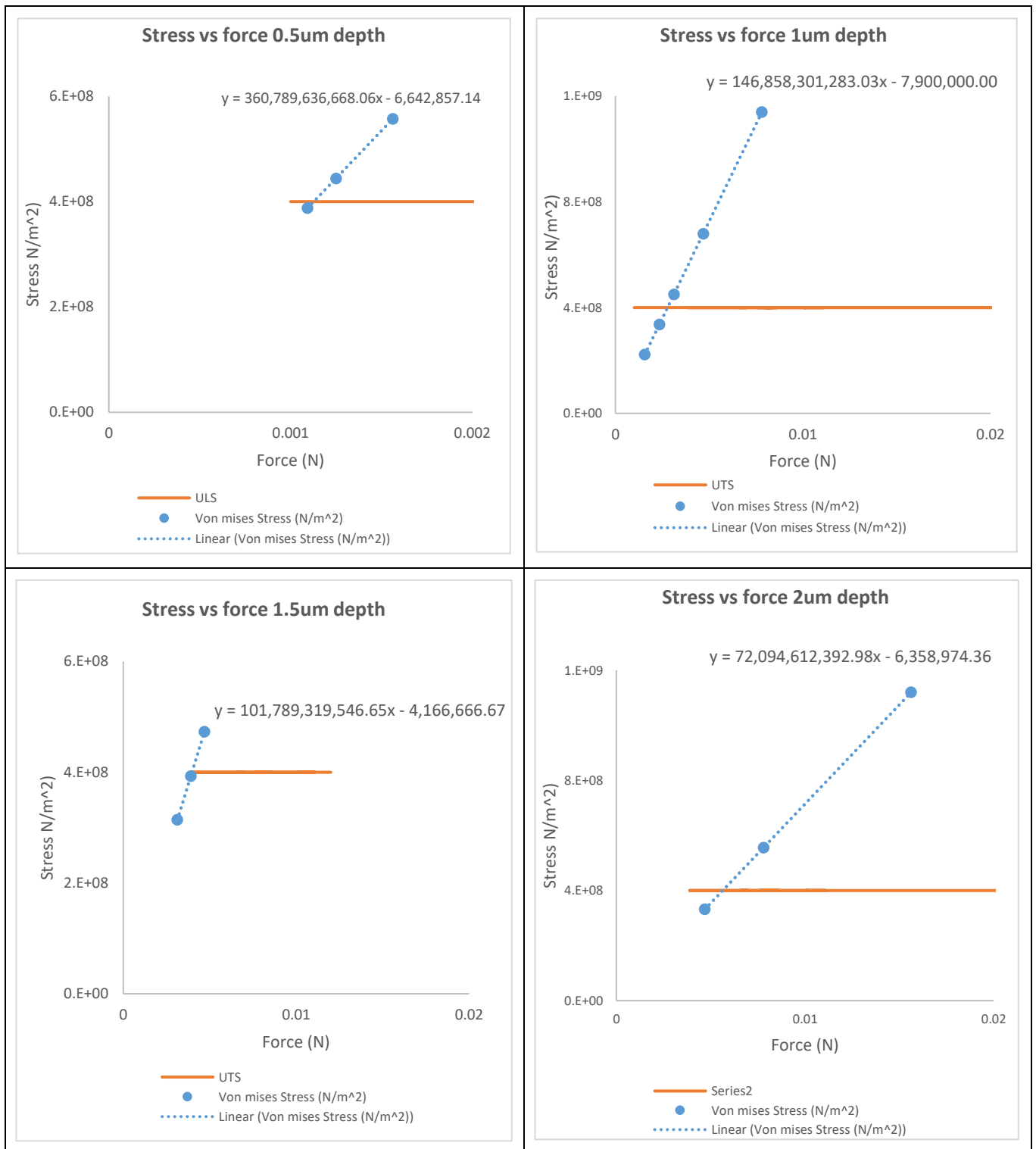


Figure 4-4: The results for the spherical shape

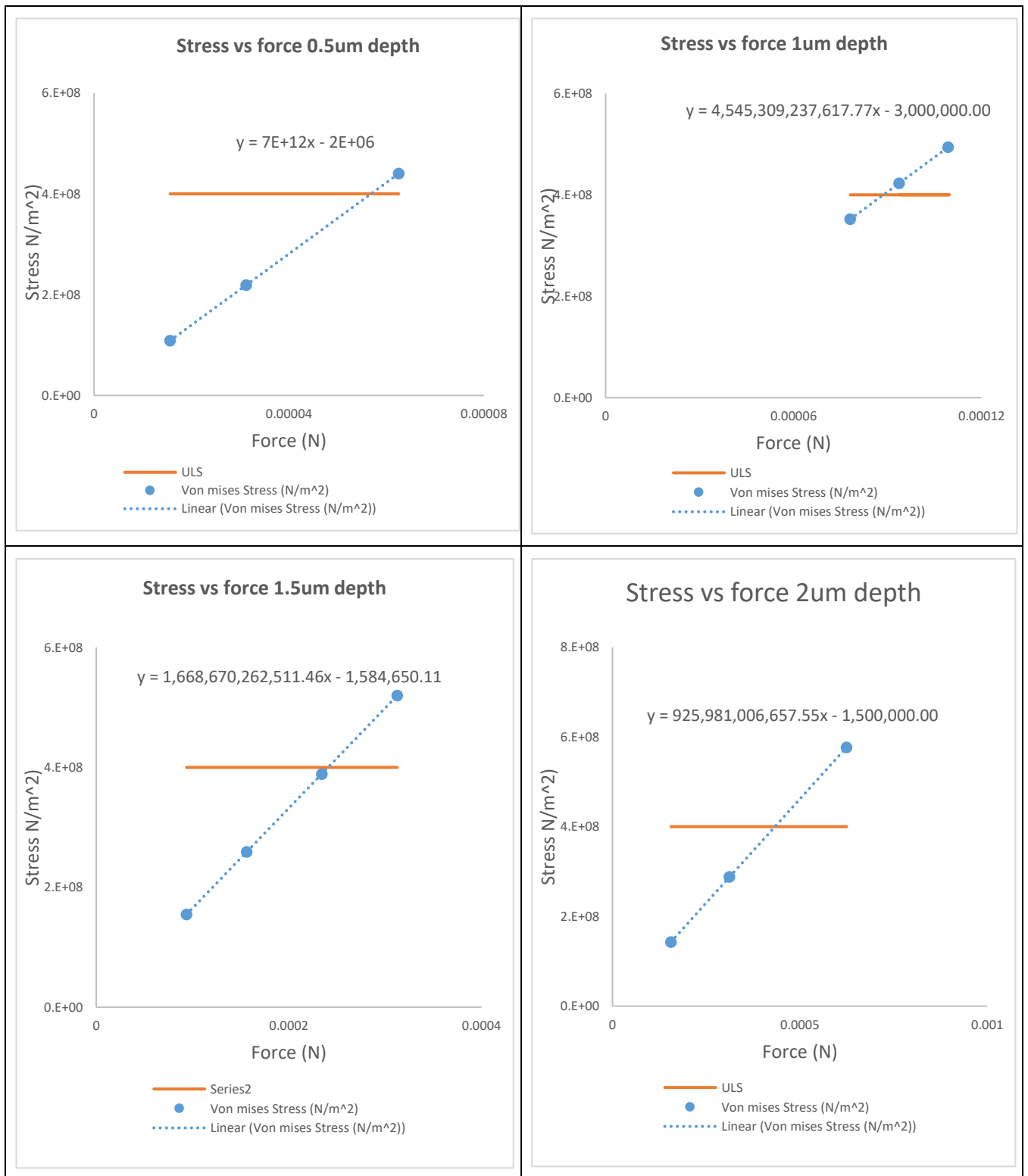


Figure 4-5: The results for the pyramidal shape

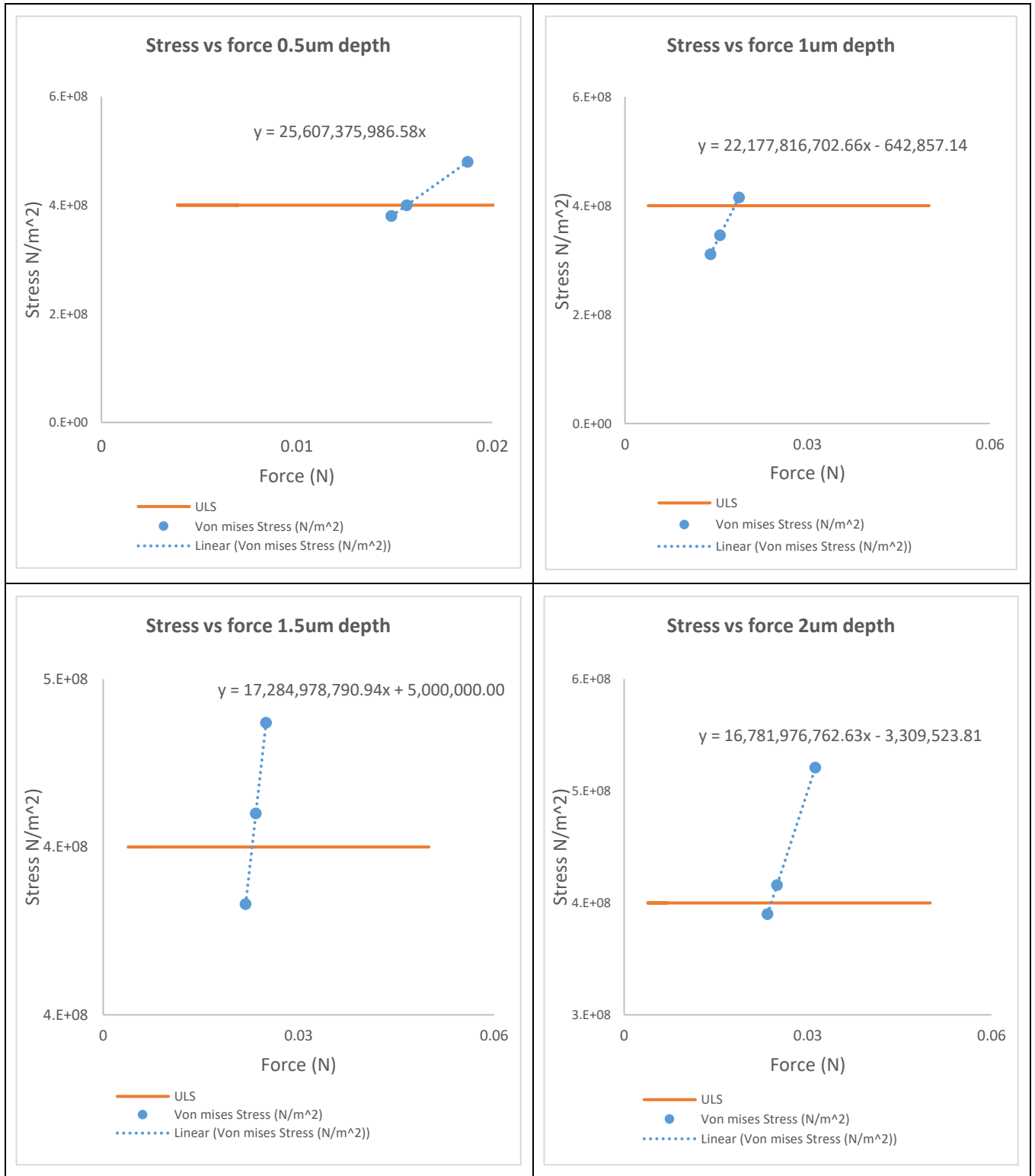


Figure 4-6: The results for the truncated shape

Table 4-4: Force simulation results

Depth ( $\mu\text{m}$ )	Force simulation results (N)		
	Spherical shape	Pyramidal shape	Truncated pyramidal shape
0.5	$1.13 \times 10^{-3}$	$5.74 \times 10^{-5}$	$1.56 \times 10^{-2}$
1	$2.79 \times 10^{-3}$	$8.88 \times 10^{-5}$	$1.81 \times 10^{-2}$
1.5	$4.00 \times 10^{-3}$	$23.6 \times 10^{-5}$	$2.30 \times 10^{-2}$
2	$5.64 \times 10^{-3}$	$43.4 \times 10^{-5}$	$2.52 \times 10^{-2}$

#### 4.6.2 Analysis of the grit shape influence

The grit shape has a great impact on the loading forces and the stress distribution on the surface contact region. Figure 4-7 shows that the cutting forces calculated based on the limit strength of workpiece material in the case of the grit of a sharp pyramidal shape were the lowest, while the forces are the highest for the grit of a truncated pyramidal shape. For the grit with spherical shape, the applied force laying in between the sharp and the truncated pyramid. The high loading forces presented by the truncated pyramid grit is due to the fact that the surface contact between the grit and the workpiece is the largest in this configuration compared to the two other cases. The high surface contact allows the stress to be spread in a large region and by consequence higher forces could be applied without reaching the ultimate limit strength of the workpiece material. On the other hand, in the case of a sharp pyramid grit shape, the surface contact is very tiny, and the stress is concentrated in a tiny region. That means only small forces could be applied before initiating cracks on the sapphire workpiece. This emphasises the significance of grit's shape on the grinding process in general and practically when brittle materials such as ceramics are considered as workpiece materials.

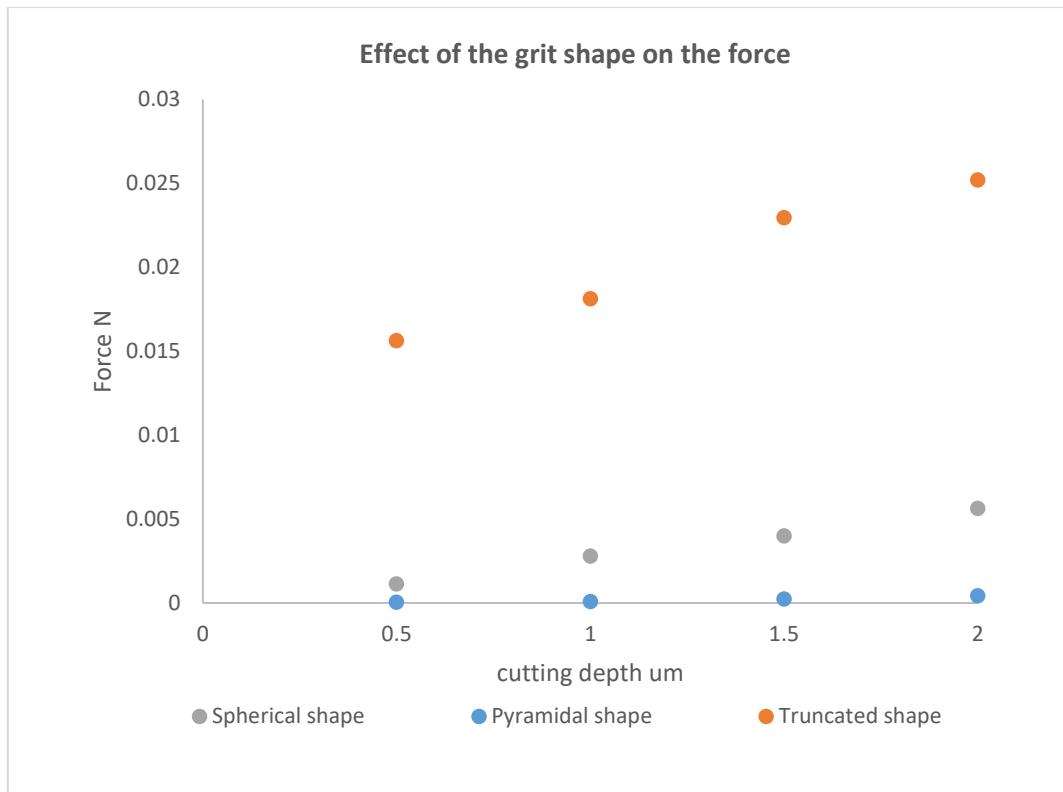


Figure 4-7: Effect of the grit shape on force level

### 4.6.3 Proposed grinding force model

The simulation results show grit's shape is effective in cutting forces. Hence, the force variation obtained from the simulation can be attributed to the grit shape and geometry.

Accordingly, the effect of the different grit shapes i.e. spherical, pyramidal and truncated shapes on the cutting force can be considered as rounded, sharp and blunt grit shape. The Figure 4-8, indicates that for each shape category the force is increasing when the cutting depth is increased but the value of the force for the same depth is different for each shape. A correlation of the force and the cutting depth is hence drawn according to the curves tendency.

Assuming that a grinding wheel is composed of abrasives with various shapes and that those shapes are classified into the three shape categories established and considered in this simulation, each shape present in the wheel with different proportion, a relationship was found as is shown in (4-2).

$$F = c_0 + \sum_{i=1}^n c_i X_i \quad (4-2)$$

Where:

$c_0$  is a correctional factor could be associated to friction forces.

$c_i = \alpha_i x^{b_i}$  are the power regression functions for the force and cutting depth curves as it is shown in Figure 4-8.

$X_i$  is the shape percentage established in Chapter 3 for each of the shapes considered,  $n$  is the number of grit shapes considered in the force model.

Ultimately, considering grit shapes of sphere, pyramid and truncated pyramid, the equation of the cutting force model will be defined as follow:

$$F = c_0 + 0.0026x^{1.1481}X_1 + 0.0001x^{1.4609}X_2 + 0.019x^{0.3551}X_3 \quad (4-3)$$

Here:  $X_1$  for the proportion of the spherical shape,  $X_2$  for pyramidal shape and  $X_3$  for the truncated shape. And  $\sum_{i=1}^3 X_i = 1$ .

Thus, this analysis provides a clear indication to specify the influence of grit shape in grinding tools that customise appropriate applications.

Finally, this model will be compared to the experimental results and will be discussed in Chapter 6.

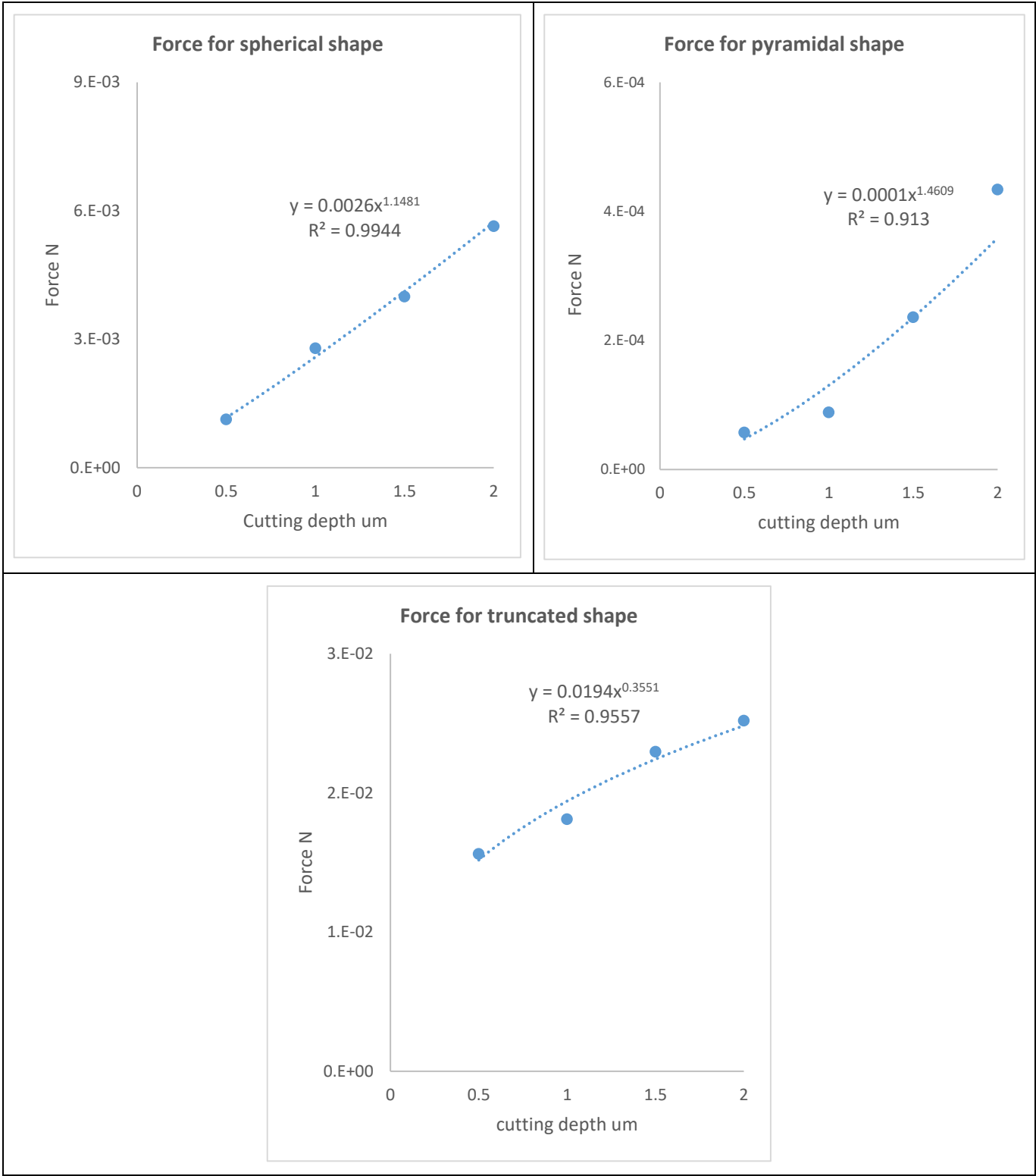


Figure 4-8: Force vs cutting depth regression model

## **4.7 Summary**

Based on the grit shape classification of the abrasives, a geometrical model of the abrasive grits was established, and a theoretical force model of the abrasive machining was proposed. The force modelling was simplified by considering only most typical grit cutting situations. The cutting forces and the stress distribution on the surface contact region of the workpiece were evaluated through FEM simulations. It was found that the grit shape has a great impact on the cutting forces and the stress distribution. The forces were the lowest in the case of the grit of a sharp pyramidal shape, while they are the highest in the case of the grit of a truncated pyramidal shape. Furthermore, a force model associating the cutting force and the shape proportion of the abrasives was established.

## Chapter 5 **Experimental investigation set up**

### **5.1 Introduction**

This work is focussing on investigating the effect of the abrasive's grit shape on cutting forces and Acoustic Emission (AE) during the grinding process. To do so, two approaches were undertaken; a series of scratching tests and a wire saw cutting tests.

For the purpose of carrying out experimental trials, an experimental test rig for multiple grit scratching and wire saw cutting were developed and set-up. In addition, several pieces of equipment have been utilised. These pieces of equipment have also been used for facilitating the data acquisition and for the recording of the experiment output data. In this chapter the description of the equipment is reviewed. Furthermore, an AE monitoring system set-up and a force sensor are described. Finally, the scratching marks generated are inspected through various measurement techniques.

### **5.2 Multiple grits scratching experimental tests**

In this study, an experiment was conducted to investigate the multiple grits scratching test on two different workpiece materials: sapphire and zirconia. Five cutting tool tips of different diamond abrasives were used for tests.

The abrasives used for the testing are listed here in bellow:

- (A) MDA A,
- (B) MDA B,
- (C) MDA C,
- (D) Synthesized M2030,
- (E) CDA M2030.

A test rig was developed, and several pieces of equipment have been used and the experimental set-up was tested to make sure that the equipment is assembled accurately in order to meet machining system requirements and to inspect the feasibility of the cutting process using the developed test rig set-up. The experiment was performed to develop a strategy to obtain acceptable results and these are compared with the numerical simulation results.

### 5.2.1 Cutting tool

In order to explore this investigation, a rotary wheel was designed and manufactured in order to conduct the tests. The selected abrasives were bounded to a grit-holder that was mounted on the rotary wheel (Figure 5-1).

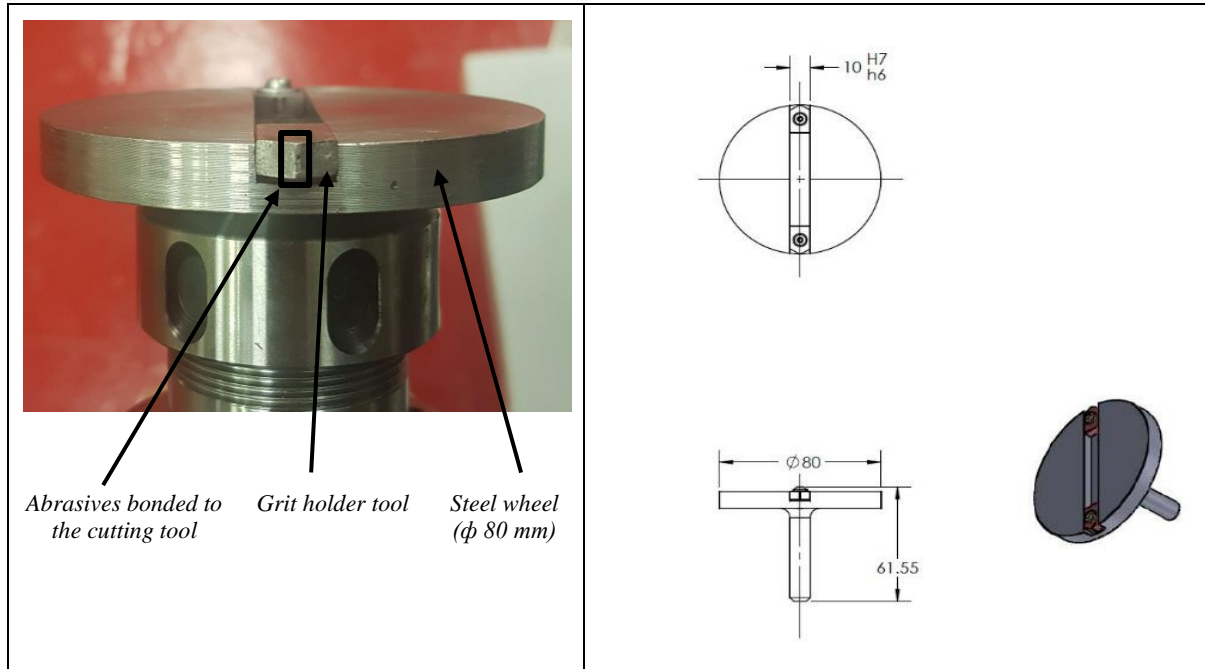


Figure 5-1: Cutting tool

### 5.2.2 Workpiece materials

Two type of advance ceramics were used in the experiments i.e. sapphire and zirconia. Both materials were provided by Element Six Ltd and are shown in Figure 5-2. Sapphire workpiece is in a cylinder shape with a diameter of 50 mm, thickness of 2 mm and surface roughness Ra 0.154  $\mu\text{m}$ ; and zirconia workpiece is in a square shape of 50 mm side length, 4 mm thickness and surface roughness Ra 0.064  $\mu\text{m}$ . Their mechanical properties of the sample materials at ambient temperature are listed in Table 5-1.

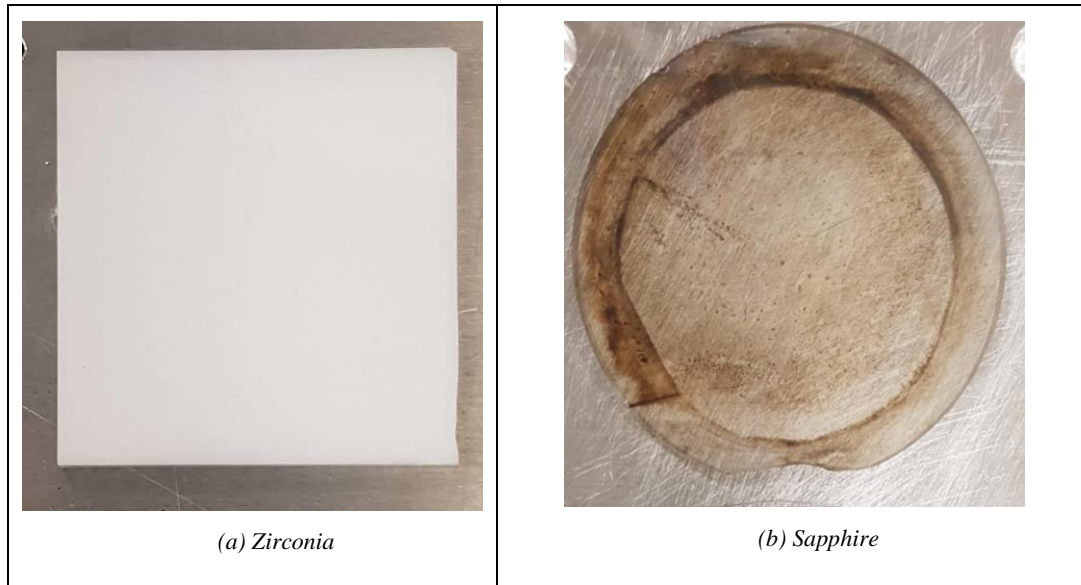


Figure 5-2: Workpiece material: (a) zirconia and (b) sapphire

Table 5-1: Material properties

property	Material	
	Sapphire <sup>1</sup>	Zirconia <sup>2</sup>
Young's modulus $E$ (GPa)	345	200
Poisson's ratio	0.28	0.25
Shear modulus (GPa)	145	53.4
Mass density ( $\text{g.cm}^{-3}$ )	3.98	5.8
Tensile strength (MPa) at 25 °C	400	410
Yield strength (MPa)	400	410
Hardness (Knoop) (GPa)	18-22	12

<sup>1</sup> <http://www.matweb.com>

<sup>2</sup> <https://www.makeitfrom.com>

### 5.2.3 Experimental test set-up and procedure

The experiment was carried out on the Heidenhein XR 610 VMC milling machine, which is a 2-axis Computer Numerically Control (CNC) machine. The CNC machine tool spindle is equipped with a rotating disc attached to the electrical spindle that can be adjusted continuously from 50-12,000 revolutions per minute (RPM). The spindle is of capability to carry out

grinding operation and a five-axis worktable has a good position accuracy at 1  $\mu\text{m}$  level.

The set of experimental tests were conducted in dry condition using the developed test rig as it shown in Figure 5-4. The operation conditions are listed in Table 5-2. The scratching tests were performed using abrasive cutting tools assembled to a rotating steel wheel. The cutting tools were made of five different types of diamond abrasives. The scratching proceeding was as follows: while the wheel is rotating, the worktable is moving through the Z-axis towards the wheel's spindle. Once the abrasive grits touch the workpiece surface, the AE sensor detects an acoustic emission signal of initial contact between the abrasives and the workpiece. At this point, the wheel rotation was set to the desired speed before the scratch test commenced. The scratching marks are generated by moving the spindle from the top to the bottom along the X-axis. The process was repeated by shifting the position of the worktable over the Y-axis to generate new series of scratches. The cutting process was undertaken with five types of abrasive on each workpiece, sapphire and zirconia respectively, where each selected type of abrasive would scratch a line on the sample.

In each machining trial, the acoustic emission (AE) was registered using a Physical Acoustics WD sensor with a sampling frequency ( $f_s$ ) of 2 MHz. The WD sensor was mounted as near as possible to the cutting zone in order detect the contact between the abrasives and the workpiece and acquire the AE signal during scratching process.

An Interface's 3-axis force sensor was used for the scratching force measurements with a sampling rate of 900 Hz. In order to assure the accuracy of the measurements and reduce the errors, the sensor was calibrated after installation; the calibration curves obtained from experimental tests are shown in Annex D-2. The recorded AE and force information will be analysed to indicate the grit performance.



*Machine specification*

<i>Spindle motor power</i>	<i>21 kW</i>
<i>Spindle speed</i>	<i>50-12000 rpm</i>
<i>Torque</i>	<i>134 Nm</i>
<i>Table</i>	<i>900x500 mm</i>
<i>Travels XYZ axis</i>	<i>610x510x610 mm</i>

*Figure 5-3: XR 610 CNC machine*

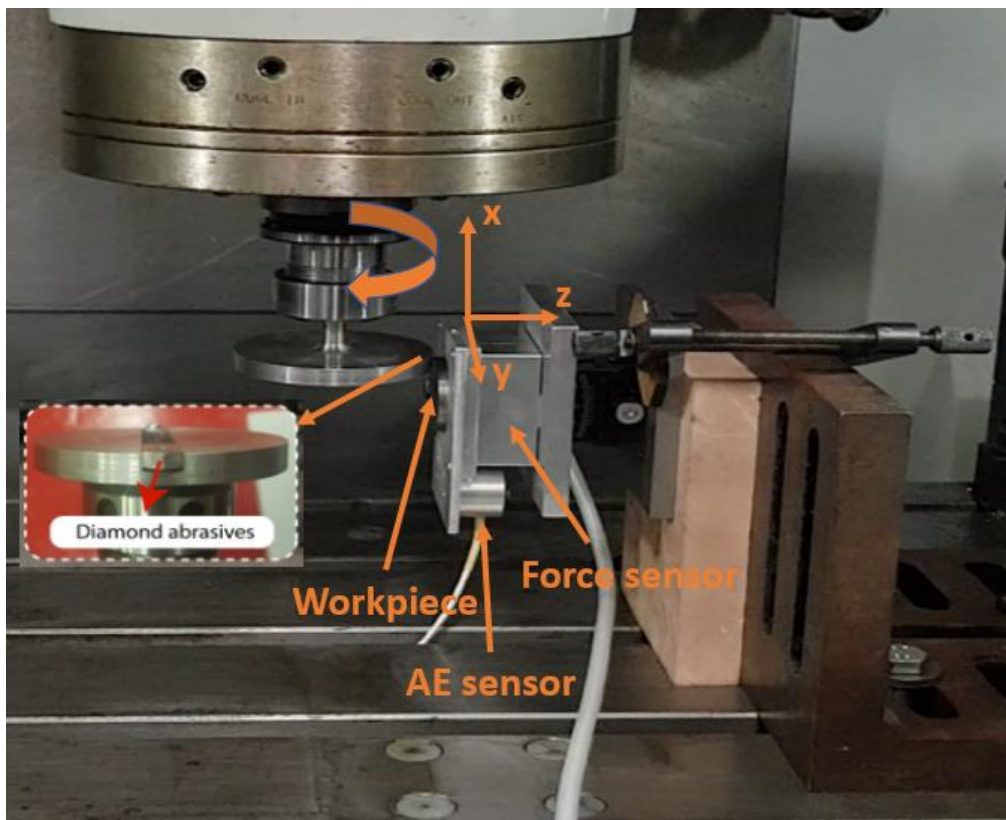


*Figure 5-4: Experimental test set up*

Table 5-2: Grinding test parameters

<i>Grinding Parameters</i>	<i>Value</i>
<i>Wheel diameter</i>	<i>80 mm</i>
<i>Cutting speed <math>V_s</math></i>	<i>1m/s</i>
<i>Feed rate in Y direction <math>V_w</math></i>	<i>1000mm/min</i>
<i>Cutting depth <math>a_e</math></i>	<i>1 <math>\mu</math>m</i>
<i>Spindle speed</i>	<i>238 rpm</i>
<i>Grinding condition</i>	<i>Dry</i>
<i>Workpiece material</i>	<i>Sapphire and zirconia</i>
<i>Abrasive</i>	<i>A: Cutting line 1: MDA A</i> <i>B: Cutting line 2: MDA B</i> <i>C: Cutting line 3: MDA C</i> <i>D: Cutting line 4: Synthesized M2030 and</i> <i>E: Cutting line 5: CDA M2030</i>
<i>Machine tool</i>	<i>XR 610 VMC CNC machine</i>

#### 5.2.4 Cutting marks inspection

Once the cutting is performed, many scratching marks are generated on the workpiece at each pass of the cutter tool on the workpiece. Those marks are the result of the penetration of the abrasive grits on the workpiece. A group of marks forms one cutting scratch and a group of cutting scratches form one cutting line (c.f. Figure 5-5). The features of these marks should be assessed to represent the grit performance. The depth of cut ( $D$ ) and the width of cut ( $W$ ) of the marks were measured using a Bruker interferometer. The ratio  $W/D$  was then evaluated to characterize the scratching surface creation.

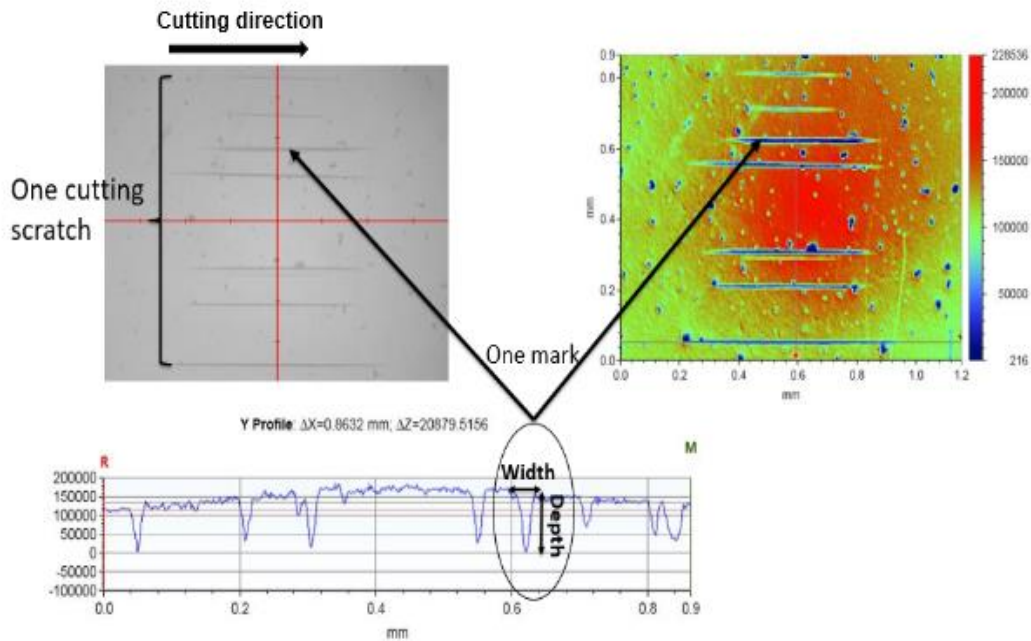
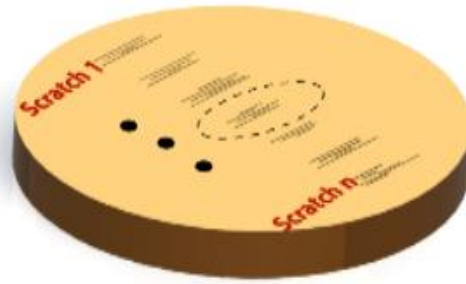


Figure 5-5: cutting marks inspection: depth and width measurements

#### 5.2.4.1 Force and acoustic emission during scratching tests

During the scratching tests, cutting forces and acoustic emission were recorded. Force profile extraction is a fundamental measurement to examine the variation of grit-workpiece interaction forces during the formation of the scratching marks. The forces were recorded during the grits scratching to obtain possible correlation between the cutting forces and the abrasives shapes. The AE was set to detect the touching between the abrasive grits and workpiece before the starting of the test. And then, the AE signal was recorded during scratching process. The raw AE signal was recorded in time domain; it can be transformed into frequency domain to obtain the power spectrum of the signal for further analysis. A direct correlation between the acoustic emission signal, the force signal and the experimental values of the width  $W$  and depth  $D$  of the marks is established where each pic on the force and the AE signal is corresponding to one cutting scratch (Figure 5-6).

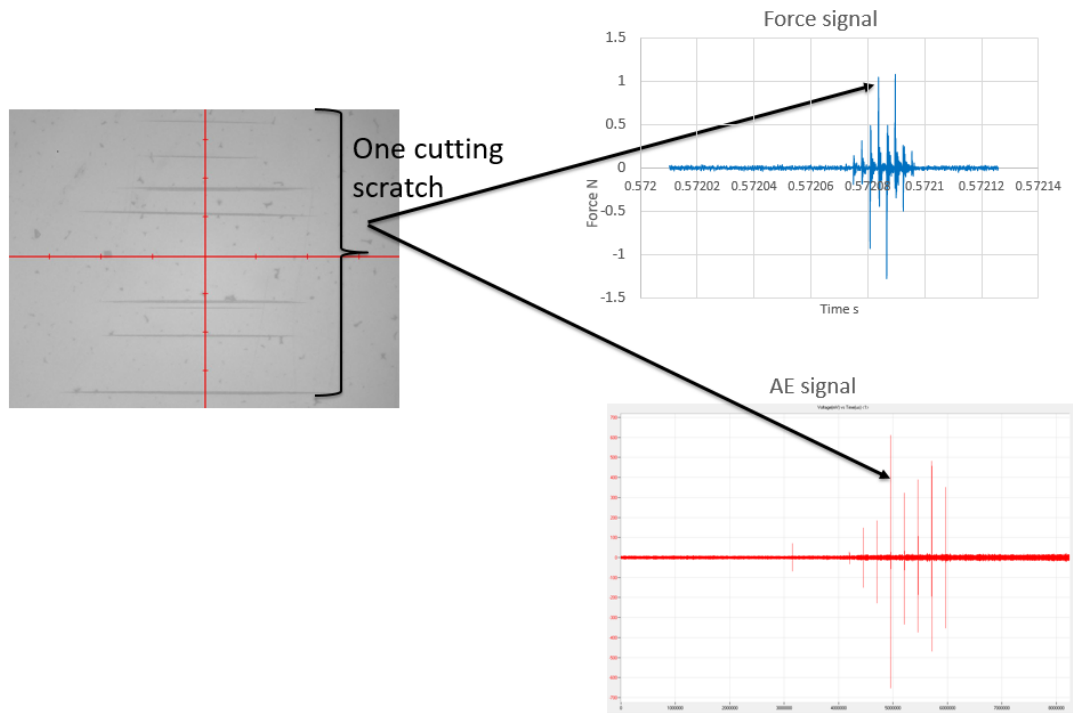


Figure 5-6: cutting marks inspection: force and acoustic emission

#### 5.2.4.2 Scratching marks surface formation inspection

Figure 5-7 shows the SEM images of a scratching mark on the sapphire workpiece surface. It shows that different surface formation modes are found along the scratching mark. At the early stage of the cut, shown in Figure 5-7.a), the cutting depth was very shallow and the cutting action occurred in the form of rubbing and ploughing but no material is removed. As the cutting progressed but still in the beginning of the cut, illustrated in Figure 5-7.b), a very small material ridge was generated by material plastic deformation and the deformed surface is smooth. The more the abrasive engages into the workpiece, the higher cutting depth is reached. At this stage of cutting, fractures and micro-cracks are generated in the cutting path as is shown in Figure 5-7.c). At the sides of the cutting path, the material accumulations are visible which can be related to material displacements by plastic deformation and pointing out that rough ploughing has taken place. As the depth of cut increases, some discontinuous chips are generated in the groove surface area as shown in Figure 5-7.c). At the end of the engagement of the abrasive in the workpiece, the material deformation was similar to the deformation which occurred during the beginning of the engagement: small depth of cut and cutting mechanism is characterised by elastic and plastic deformation by means of rubbing and ploughing.

From these surface creation observations, it could be concluded that the surface formation mode is depending on a certain critical cutting depth. Shallow depth implies ductile cutting

mode characterised by rubbing and ploughing, and as the value of the cutting depth increases brittle cutting mode takes place identified by the occurrence of the fracturing on the ground surface of the workpiece.

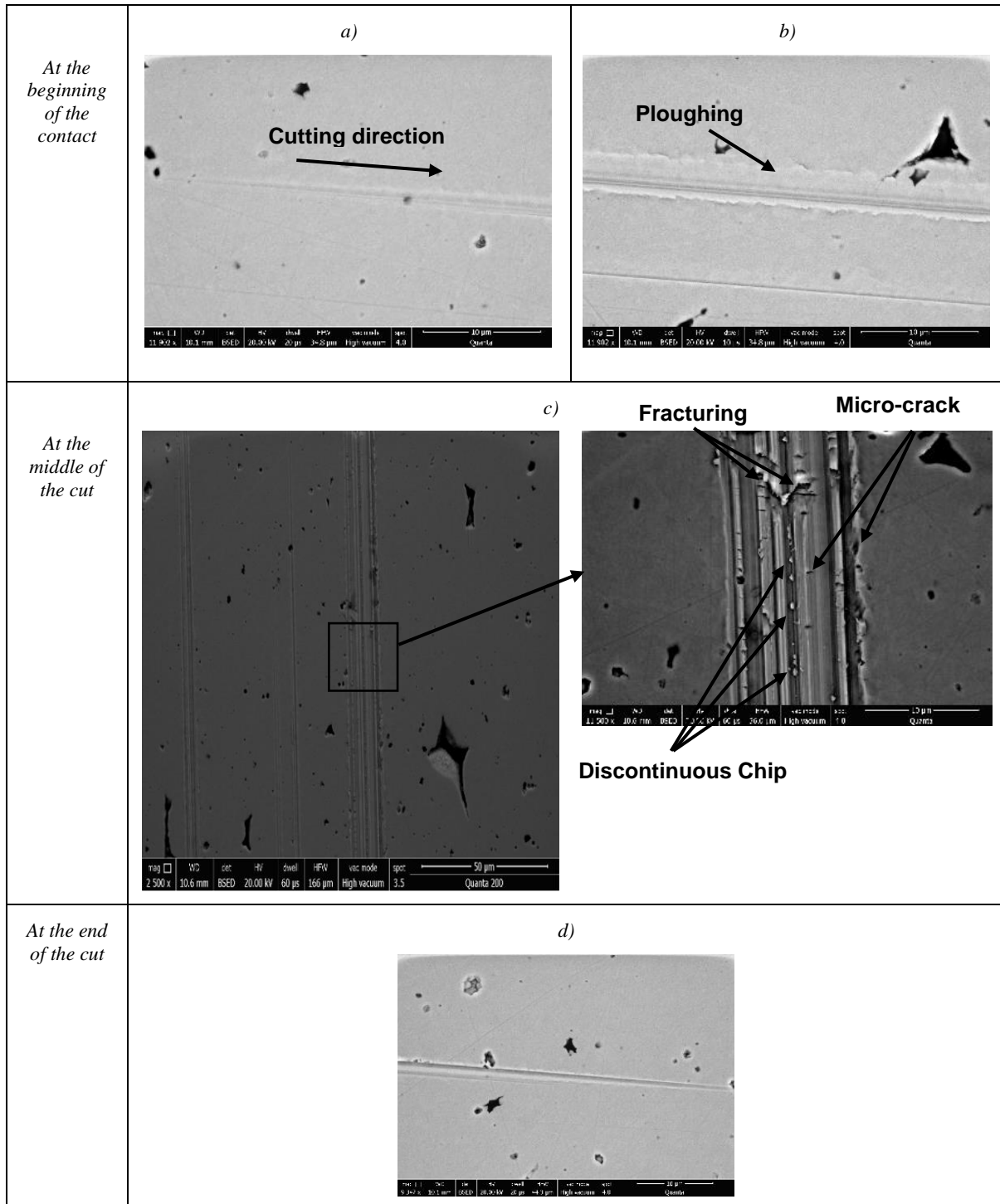


Figure 5-7: SEM images of scratching marks obtained in Sapphire cutting

### 5.3 Diamond wire saw cutting test

Wire saw experiments were conducted on a sapphire bar of 50 mm diameter. Details of the experimental set-up are presented in this section.

Three different diamond wires were used in the tests. The characterisation grits on these three wires was provided in Chapter 3. The experiments were conducted to investigate the influence of three types of diamond wires, in which the focus is on the influence of diamond abrasive shape. Thus, all the processing parameters are kept constant for the experiments and only the diamond wires were changed from an experiment to another.

In order to do the experiment, a test rig was designed. The designed test rig was set up to meet predefined requirements that include: the performing of the cut under a constant speed, controllability of the diamond wire tension and use of a small length of wire (approximately 30 cm). To achieve these requirements, it was decided that the cut will be accomplished through pushing a fixed saw wire against a rotating workpiece with a constant normal force. The proposed conceptual design is shown in Figure 5-8. The diamond wire is set to be installed around two pulleys and fixed in its two extremities; one extremity is slotted in and the second extremity is attached into a tension spring. The tension spring is linked to an S beam strain gauge force sensor allowing the diamond wire tension control by an adjustment screw. This set of elements (diamond wire, two pulleys, force sensor, tension spring) are mounted into a holder (wire holder) and constitute one assembly. Through a guide pin and a weighting wire this bloc is affixed into a counterbalancing-weight enabling a vertical movement of the bloc. This movement allows the diamond wire to come into contact with the workpiece.

The workpiece is mounted onto a chuck on the feed axis of the diamond wire and the chuck is mounted onto an electric motor permitting the control and the adjustment of the workpiece rotation speed.

Once the wire is in touch with the workpiece at a stabilized position established by the counterweight, the wire pushes against the workpiece with a desirable constant force determined by the counterweight balancing. Finally, the cut could be performed by turning on the electrical motor which allows it to provide a constant rotation speed to the workpiece. The cut is interrupted by lifting the diamond wire away from the workpiece; this is done by adding a counterweight.

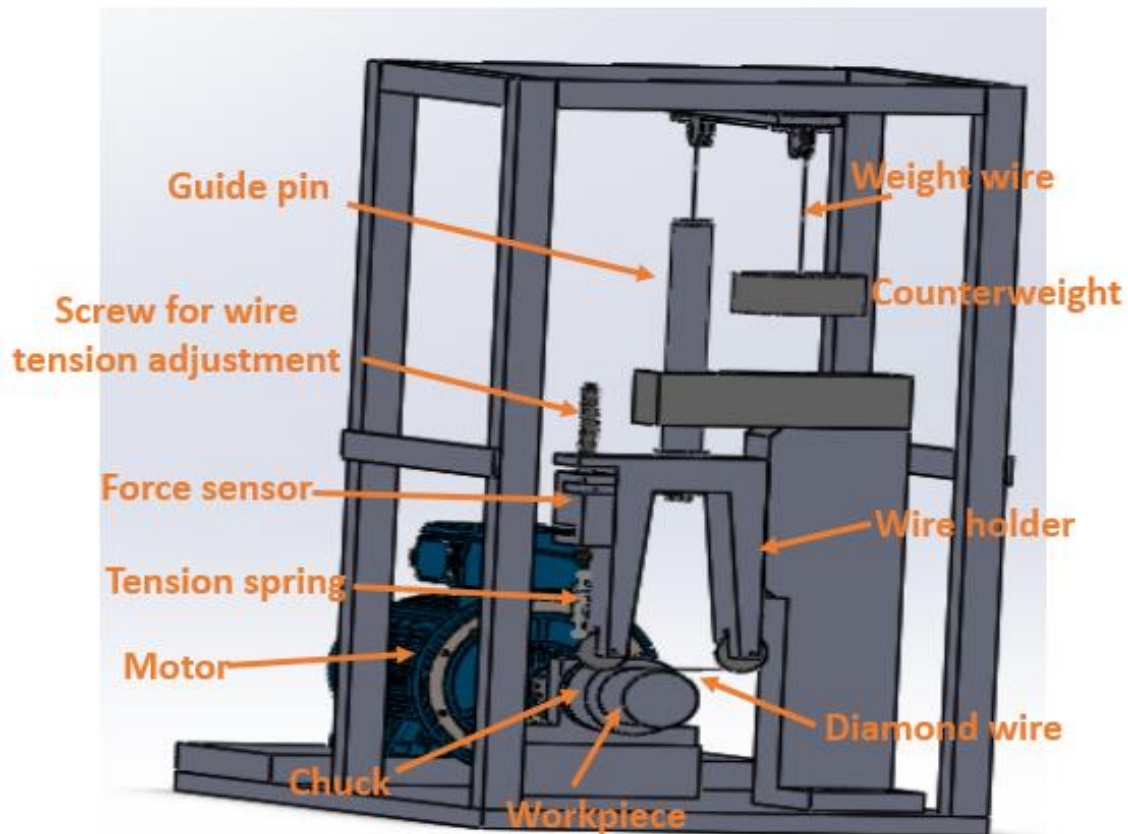
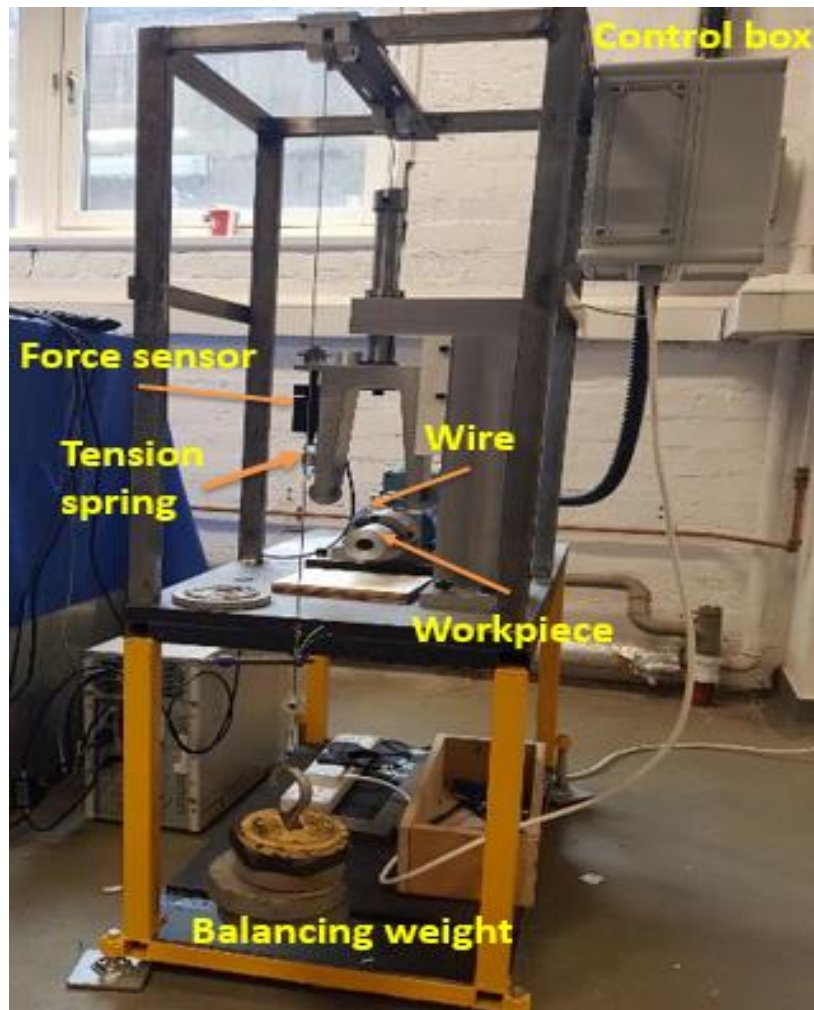


Figure 5-8: Conceptual design of the diamond wire saw rig

Based on the conceptual design, the diamond wire saw test rig was assembled and is shown in Figure 5-9. The tests were undertaken following the test's conditions displayed in Table 5-3. The sapphire workpiece bar with wire cut kerf loss after undertaking first tests is shown in Figure 5-10 and the tests proceeded under the following conditions based on industry requirements:

- Making the wire in touch with the workpiece and balancing the wire holder using the counterweight balance
- Setting the wire tension to 20N
- Applying 2N force as feed force
- Turning the motor on at 382 rpm from the control box
- After 10 s of cut, lifting away the wire from the workpiece
- Checking the wire conditions



*Figure 5-9: Diamond wire saw test rig*

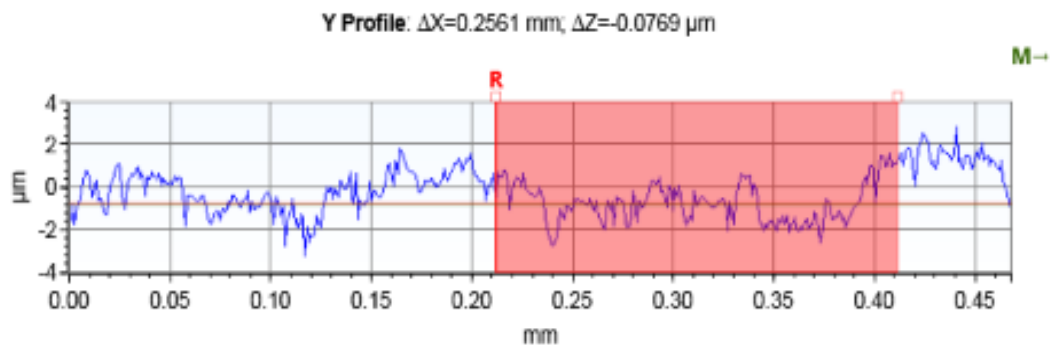
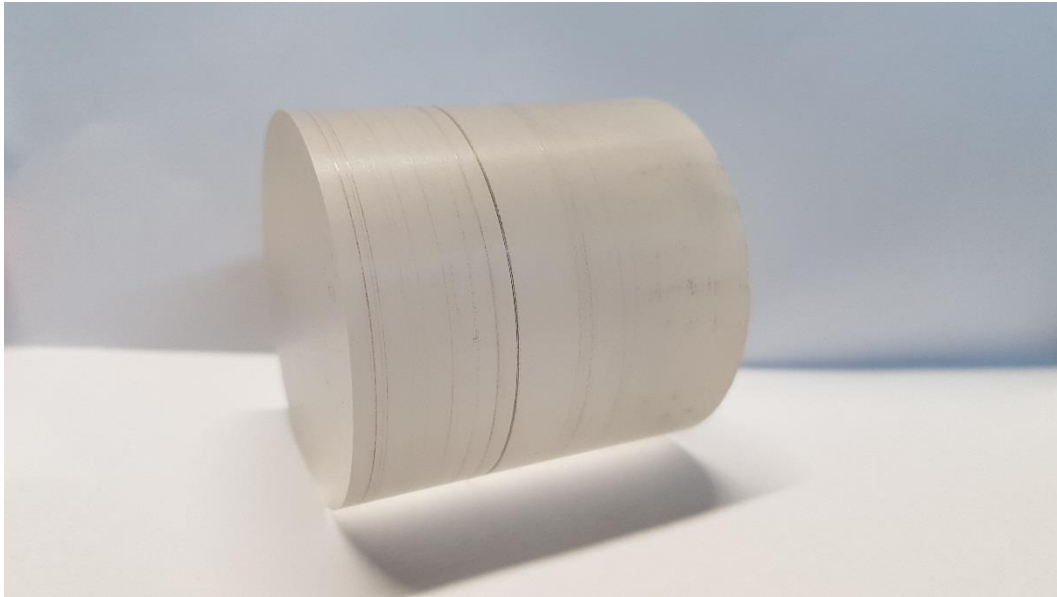


Figure 5-10: Sapphire workpiece bar with wire cut kerf loss

Table 5-3: Diamond wire cutting test conditions

Cutting Parameters	Value
Wire tension	20 N
Workpiece speed $V_w$	1 m/s (382 rpm)
Cutting time	10s
Feeding Force	2 N
Workpiece material	Sapphire bar
Diamond wires	Wire 1: 30 – 40 $\mu$ m diamond size Wire 2: 10 – 20 $\mu$ m diamond size Wire 3: 8 – 16 $\mu$ m diamond size

## **5.4 Summary**

In this chapter, the approach followed during the research study has been developed. Particularly the experimental setup and procedure for a series of scratching tests and a wire saw cutting tests. For this purpose, a test rig for multiple grit scratching and wire saw cutting rig were developed. The sensors used for monitoring and recording process signals, a force and an AE system sensor, were described for multiple grit grinding. The scratching marks assessment and analysis was described to obtain possible correlation between the cutting forces and the abrasives shapes.

## Chapter 6 Cutting force results and model validation

### 6.1 Introduction

In the previous chapter, multiple grit grinding and wire saw cutting tests were described. The results obtained, in terms of cutting forces and specific force (which is defined as the ratio of the cutting force over the cutting depth) are presented in this chapter for analysis. The influence of the abrasive grit shapes on the force will be particularly analysed and discussed in detail. The effect of each of the three categories of abrasive shapes established previously (rounded, pyramid and truncated shapes) on cutting forces is highlighted. The investigation is carried out on two different workpiece materials, sapphire and zirconia, for the multiple grit scratching and only sapphire material was tested, for wire saw cutting. Finally, comparison of the experimental and theoretical results is addressed.

### 6.2 Effect of grit's shape on specific cutting force

In chapter 3, abrasive grits characterisation, each abrasive (from the five types of abrasives used in the multiple grit cutting test and three types of abrasives used in the wire saw cutting test) was classified based on the geometrical shape of the grits constituting each abrasive type. Three groups of shape were selected: rounded shape, pyramidal shape and pyramidal truncated shape to represent rounded, sharp and blunt grits. The proportion of every group of shapes in each abrasive was identified using the method described in chapter 3. For this analysis, the proportion of the shapes on each abrasive cutting tool is utilised to evaluate the measured cutting forces for two workpiece materials on the case of multiple grit cutting test and the cutting forces on the wire saw cutting test.

#### 6.2.1 Sapphire

The forces were recorded at all marks for each cutting line, where each abrasive was associated to a cutting line. To make fair comparison, the specific force, defined as force divided by depth of cut, is shown in Figure 6-1. It can be observed that the specific forces in each cutting line gradually increase while producing more scratches up to a certain stage where the forces start to decrease. In fact, at the beginning of the scratching process, the abrasive grits were sharp and hence imply lower forces. However, as the scratching continues generating more marks on

the workpiece the grits are getting more and more worn and consequently the forces increase as a result of the grits wear phenomena. Figure 6-2 shows SEM images of abrasive grits before and after the scratching process. It is clearly seen that the morphology of the grits on the cutting tool before scratching are with sharp edges. While worn grits are noticed, with fractures and blunt edges, after the cutting. The later decrease in the force values after a period of increasing could be due to fact that at this stage of the process, the first set of grits in contact with the workpiece are either fractured into smaller and sharper grits or pulled out from the cutting tool; and new sharper grits start engaging and taking place in the process. The sharper new grits engaged in the scratching process are generating lower force. The cutting forces are continuously in evolution during the scratching process influenced by the degree of the wear or the self-sharpening of the grits.

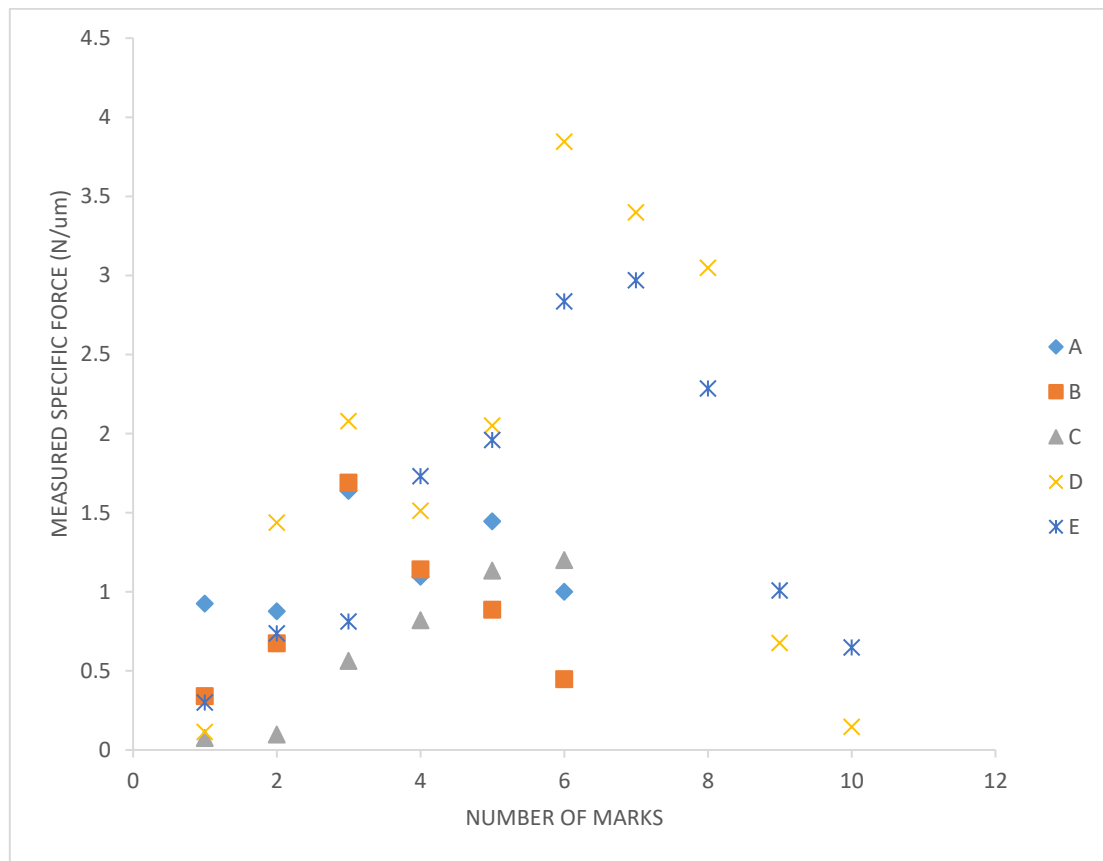


Figure 6-1: Measured specific force on multiple grit cutting test. Workpiece: sapphire

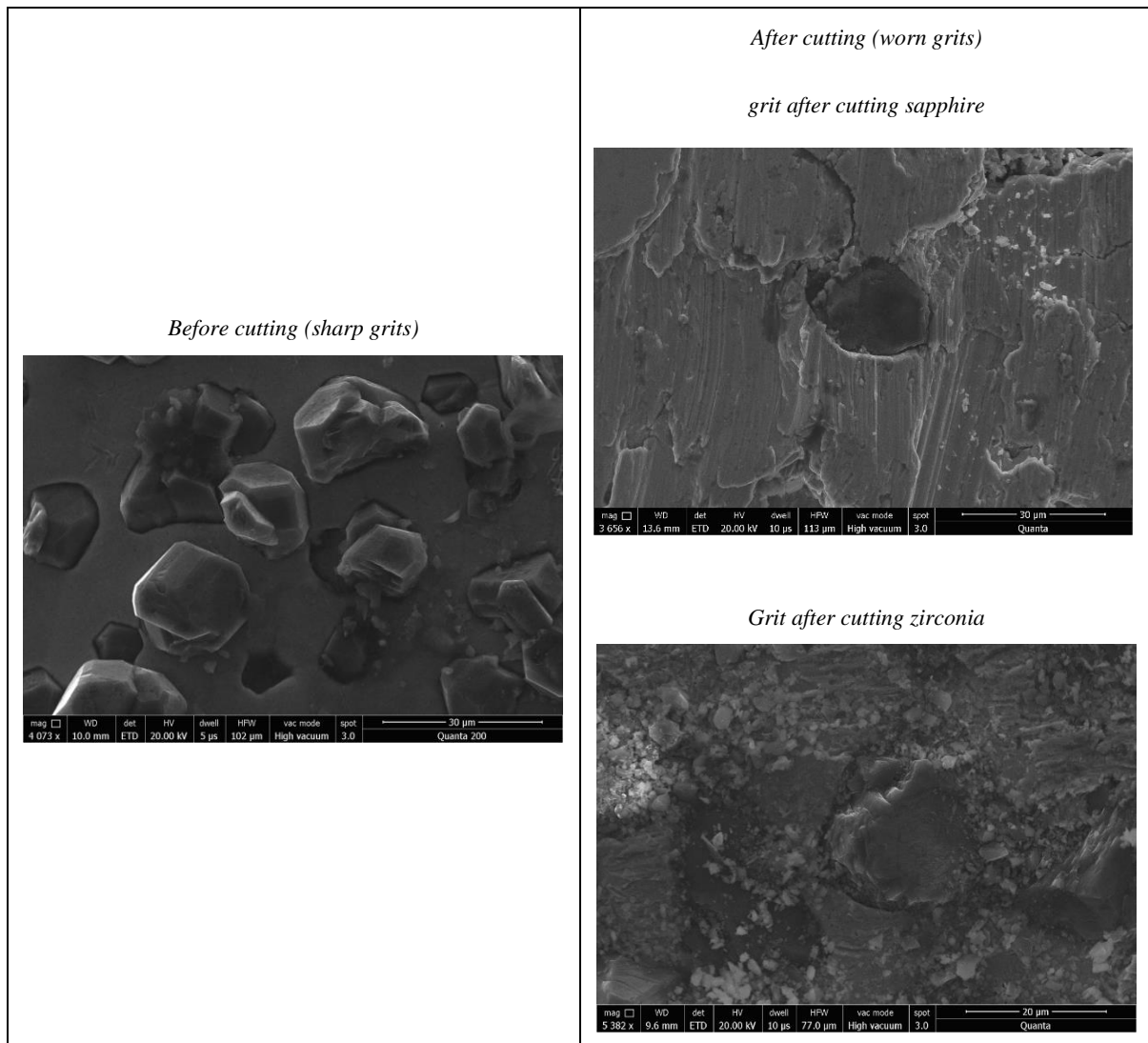


Figure 6-2: SEM images of the abrasive grits before and after scratching test

In order to emphasize the effect of each group of the grit shapes on the force variations, a deeper analysis of every cutting line and the associated abrasives is necessary.

The different group shapes for the abrasive “C” are of roughly balanced proportions as is shown in Table 6-1: 34%, 29% and 28% for rounded shape, pyramidal shape and truncated pyramidal shape respectively. Moreover, in the third cutting line associated with the abrasive “C”, the specific force behaviour in this case of cutting shows a progressive increase (cf. Figure 6-1). In addition, the average force generated during the cutting with the abrasive “C” was the lowest (only 1.02 N) compared to the average forces engendered while cutting with the four other abrasives (cf. Table 6-1). This could mainly be explained by the proportion of the pyramidal shape grits (the sharpest grits) in the abrasive “C”. 29% of shapes are pyramidal, which is the highest percentage in comparison to its proportion in the four other abrasives. The more the

proportion of the pyramidal shape is present in the abrasive cutter, the lower the cutting force generated.

The specific force behaviour in the case of scratching with the abrasives “D” and “E” shows similar tendency. In these two abrasives, the grit shapes distribution is as following 51% and 52% for rounded shape, 18% and 17% for pyramidal shape, 22% and 25% for the truncated pyramid shape for the abrasive group “D” and “E” respectively. The proportion of each group shape is very close in each abrasive. Each shape group has a close percentage on each abrasive. Additionally, the average measured forces in the case of cutting with these two particular abrasives are the highest compared to the remaining abrasives, where 1.77 N in the case of cutting with the abrasive group “D” and 2.86 N in the case of cutting with the abrasive “E”. This is to correlate with the proportion of the rounded shape present in the two abrasives: 51 and 52% respectively, which are the highest proportion, compared to the proportion of this group of shapes in the other abrasives. It can be derived that the more the proportion of the rounded shape is present in the abrasive the more the cutting force generated is higher. It can be seen that the round shape of abrasive has heavier weighted influence on the total cutting force, which would be an evidence in later part of force model validation. In contrast, the force is tending to be lower as the ratio of the pyramidal shape is higher.

Finally, the specific force in the case of cutting with the abrasives “A” and “B” follows the same tendency; the specific forces gradually increase while producing more scratches and then a decrease in its values takes place.

*Table 6-1: Geometrical grit shapes proportion in each abrasive and the associated total measured force. Workpiece: sapphire*

<i>Abrasive</i>	<i>Rounded shape proportion (%)</i>	<i>Pyramidal shape proportion (%)</i>	<i>Truncated pyramidal shape proportions (%)</i>	<i>Average measured force (N)</i>	<i>Average measured specific force (N/μm)</i>
<i>A</i>	<i>38</i>	<i>23</i>	<i>30</i>	<i>1.57</i>	<i>1.63</i>
<i>B</i>	<i>38</i>	<i>23</i>	<i>28</i>	<i>1.29</i>	<i>0.91</i>
<i>C</i>	<i>34</i>	<i>29</i>	<i>28</i>	<i>1.02</i>	<i>0.54</i>
<i>D</i>	<i>51</i>	<i>18</i>	<i>22</i>	<i>1.77</i>	<i>1.18</i>
<i>E</i>	<i>52</i>	<i>17</i>	<i>25</i>	<i>2.86</i>	<i>1.44</i>

## 6.2.2 Zirconia

The multiple grit scratching test was also performed on Zirconia which has a lower hardness value (1350 HV) than Sapphire (2500 HV). The Figure 6-3 shows the variation of the specific forces during the cutting with the five different abrasives. It is observed that there is the same tendency as was observed previously for the case of cutting Sapphire materials: progressive increase in the specific forces until it reaches a maximum and then a second phase is launched where the specific forces begin to fall down. It can again be attributed to the wear, fracture and the pull out of grits during the scratching process.

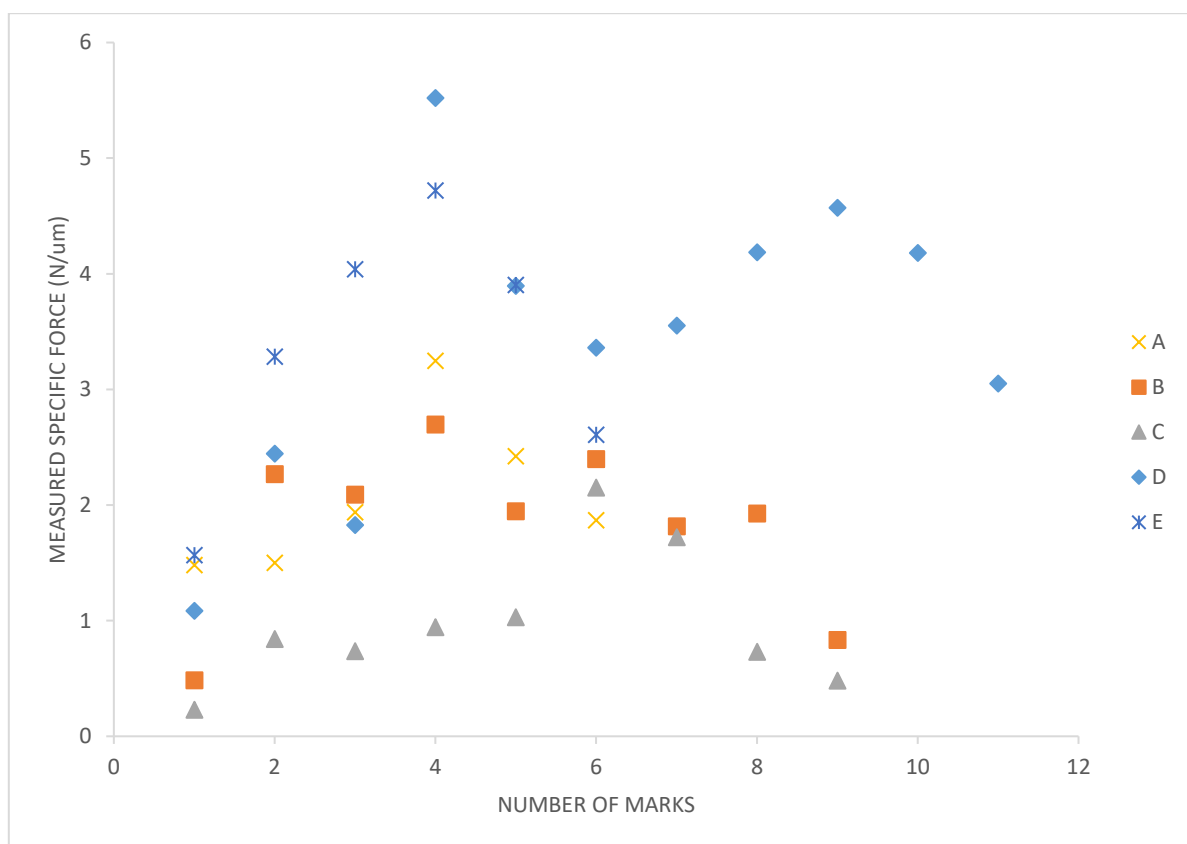


Figure 6-3: Measured specific force on multiple grit cutting test. Workpiece: zirconia

Furthermore, the lowest force was also obtained in the case of cutting with the abrasive “C”: 0.65 N (Table 6-2). In this configuration, the proportion of the pyramidal shape is the highest and the proportion of the spherical shape is the lowest in the abrasive “C” compared to that of other abrasives. In contrast, the proportions of the rounded shape were the highest for the abrasives “D” and “E”. Which was reflected in the amount of the forces measured while cutting with these two abrasives: 1.57 N and 1.29 N for “D” and “E” respectively. These forces are the

highest measured during the scratching process on Zirconia as is shown in Table 6-2.

The analysis of the cutting forces during the scratching tests on Sapphire and Zirconia highlighted the influence of the abrasive grit shapes during the process. Abrasive grits with rounded shape imply high cutting forces, while grits with pyramidal shape generate low cutting forces. Furthermore, grits' shape continuously changes during the formation of the marks and scratches on the workpiece: grits wear, grits fracture and grits pull out continuously happen and the forces trend are accordingly variate following those changes.

*Table 6-2: Geometrical grit shapes proportion in each abrasive and the associated total measured force. Workpiece: zirconia*

<i>Abrasive</i>	<i>Rounded shape proportion (%)</i>	<i>Pyramidal shape proportion (%)</i>	<i>Truncated pyramidal shape proportions (%)</i>	<i>Average measured force (N)</i>	<i>Average measured specific force (N/μm)</i>
<i>A</i>	38	23	30	1.15	2.14
<i>B</i>	38	23	28	1.13	1.77
<i>C</i>	34	29	28	0.65	0.92
<i>D</i>	51	18	22	1.57	3.31
<i>E</i>	52	17	25	1.29	3.24

### **6.2.3 Cutting performance comparison on sapphire and zirconia**

The following graph in Figure 6-4 reflecting the experimental results of the cutting forces for the two different materials namely Sapphire and Zirconia. Here identical conditions of grinding operation were used, and the graph illustrate the performance of both materials in terms of cutting force. It can be seen that, Sapphire appears to have the highest demand of cutting forces, in comparison to Zirconia in the five cases of cutting (Each case with a different abrasive). This difference of performing is attributed to the nature and the mechanical properties of the materials. Zirconia material is more softer than sapphire consequently the number of grits engaged into zirconia workpiece and participating in the cutting process is higher than in sapphire as it can be seen in Figure 6-5. Sapphire is much harder than Zirconia and consequently the forces needed to cut Sapphire are higher.

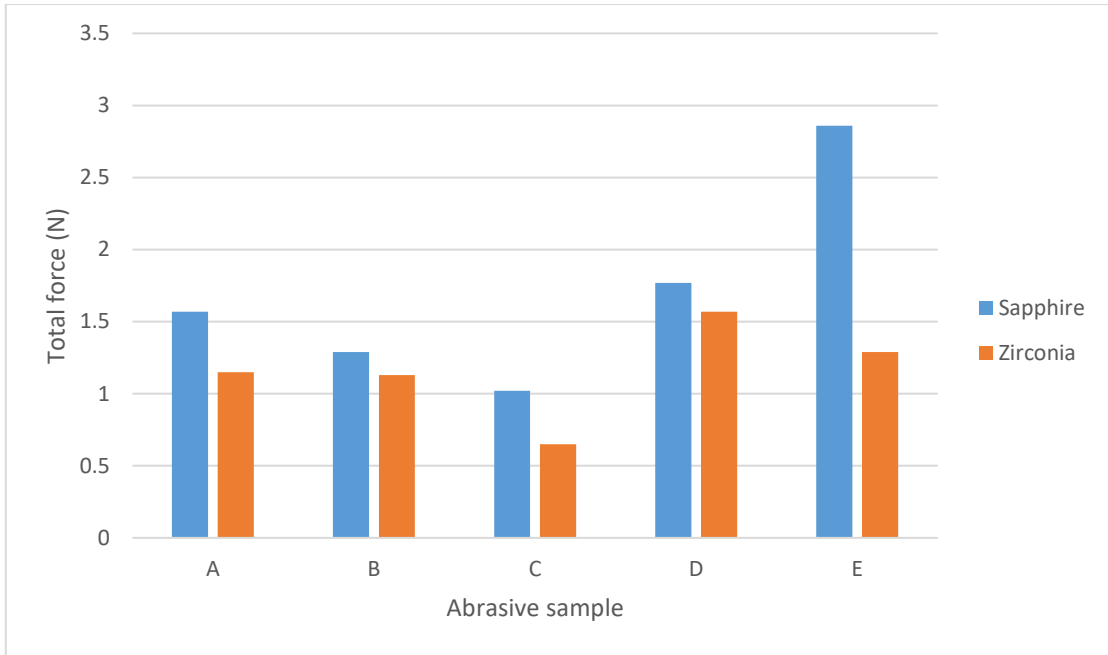


Figure 6-4: Cutting force comparison for Sapphire and Zirconia

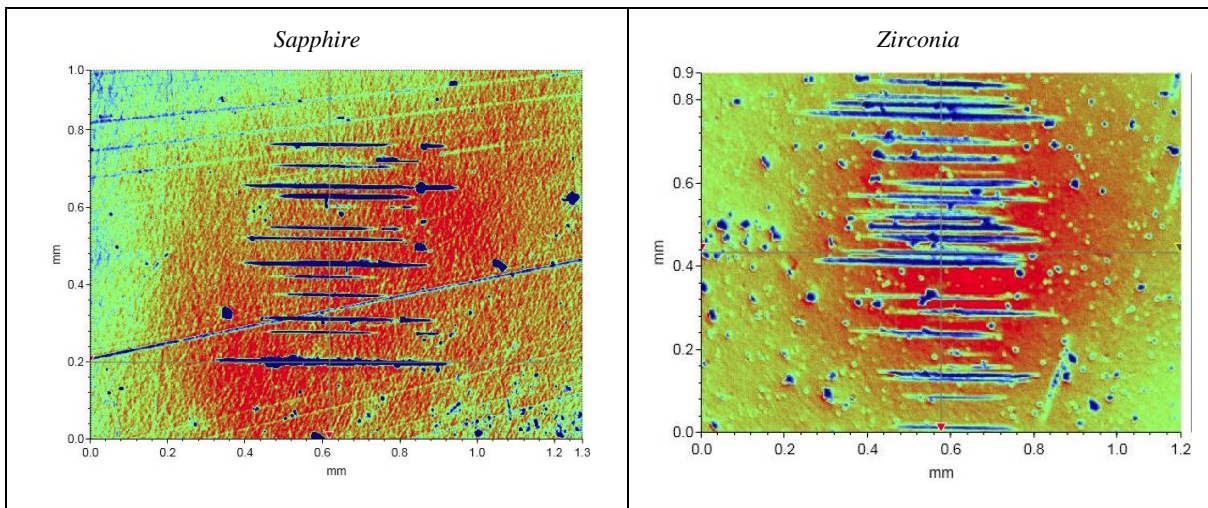


Figure 6-5: Grits engagement in sapphire and zirconia materials

#### 6.2.4 Wire saw cutting

After completing the first experiments on multiple grit cutting, it was quite evident that the abrasives grit shapes highly influence the amplitude of the forces generated during the scratching process. The second set of tests was set up to examine again the effects the grits shape during the wire saw cutting of Sapphire material on cutting forces.

In total, three different diamond coated wires were used in this series of tests and each wire was characterised in respect to the shape of the abrasives displayed over to each wire as it was previously established in Chapter 3.

After processing the experimental data, the cutting forces are obtained for the three different wires and are plotted in the Figure 6-6.

The interpretation of the force plot could be as showing a process in which the diamond abrasives wear extremely. At the initial stage, the forces are very low then as the tests went on the forces increased remarkably. The SEM images of the wires after the cutting process shown in the Figure 6-7 reveal a severe wear on the abrasives and even the abrasives are ripped out from the side of the wire involved in the cutting and hitting the surface workpiece. The cutting performance of each wire in relation to the abrasive grit's shape could also be assessed and compared. During cutting with the 30–40 wire, the forces generated are the highest. However, the forces were the lowest when the cutting was done with the 10-20 wire whereas the force rate stands in between in the case of cutting with the 8-16 wire. The grit's shape enacted a meaningful effect on the cutting forces since the abrasive's shapes distribution on the three wires demonstrates disparities as is shown in the Table 6-3. The percentage of the rounded shape, 74%, on the 30-40 wire was the highest, compared to its percentage on the other wire, and so was the force produced with this same wire. On the other hand, the percentage of the pyramidal shape, 16%, on the 10-20 wire was the highest and therefore the force observed was the lowest. This result on the wire cutting test comes to confirm what was initially deduced from the multiple grit cutting test relating to the impact of the grit's shape on the cutting forces. To achieve a lower force, a high proportion of pyramidal shapes and low proportion of rounded shapes are more suitable.

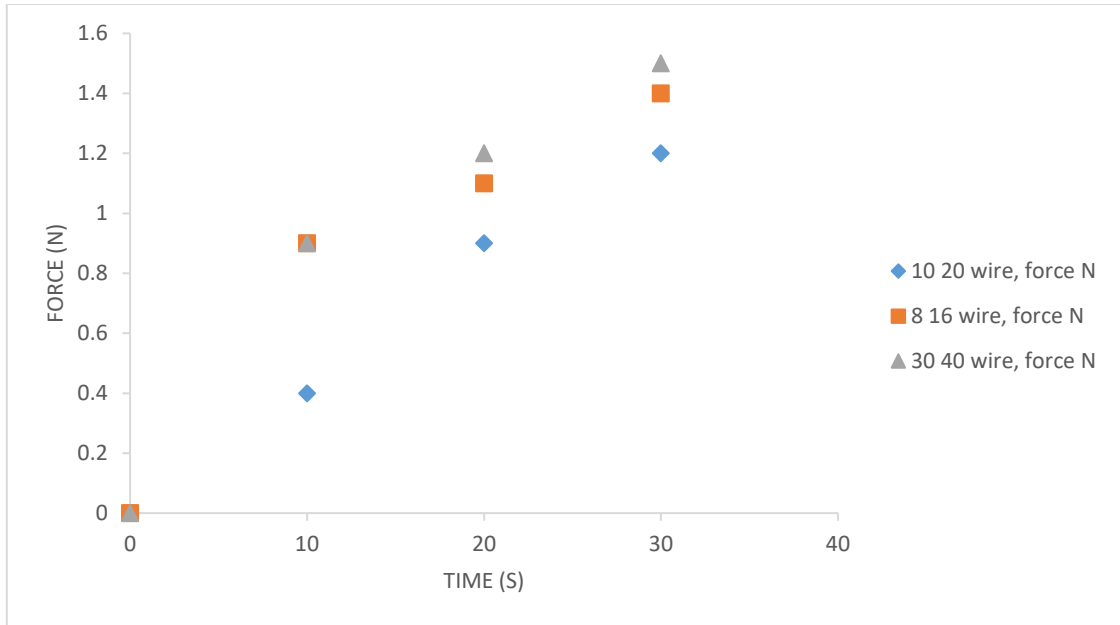


Figure 6-6: Measured forces during the wire saw cutting tests

Table 6-3: Geometrical grit shapes proportion in each wire and the associated total measured force

Wire saw	Rounded shape proportion (%)	Pyramidal shape proportion (%)	Truncated pyramidal shape proportions (%)	Total force (N)
30 40 wire	74	0	26	1.2
10 20 wire	48	16	30	0.83
8 16 wire	68	6	26	1.13

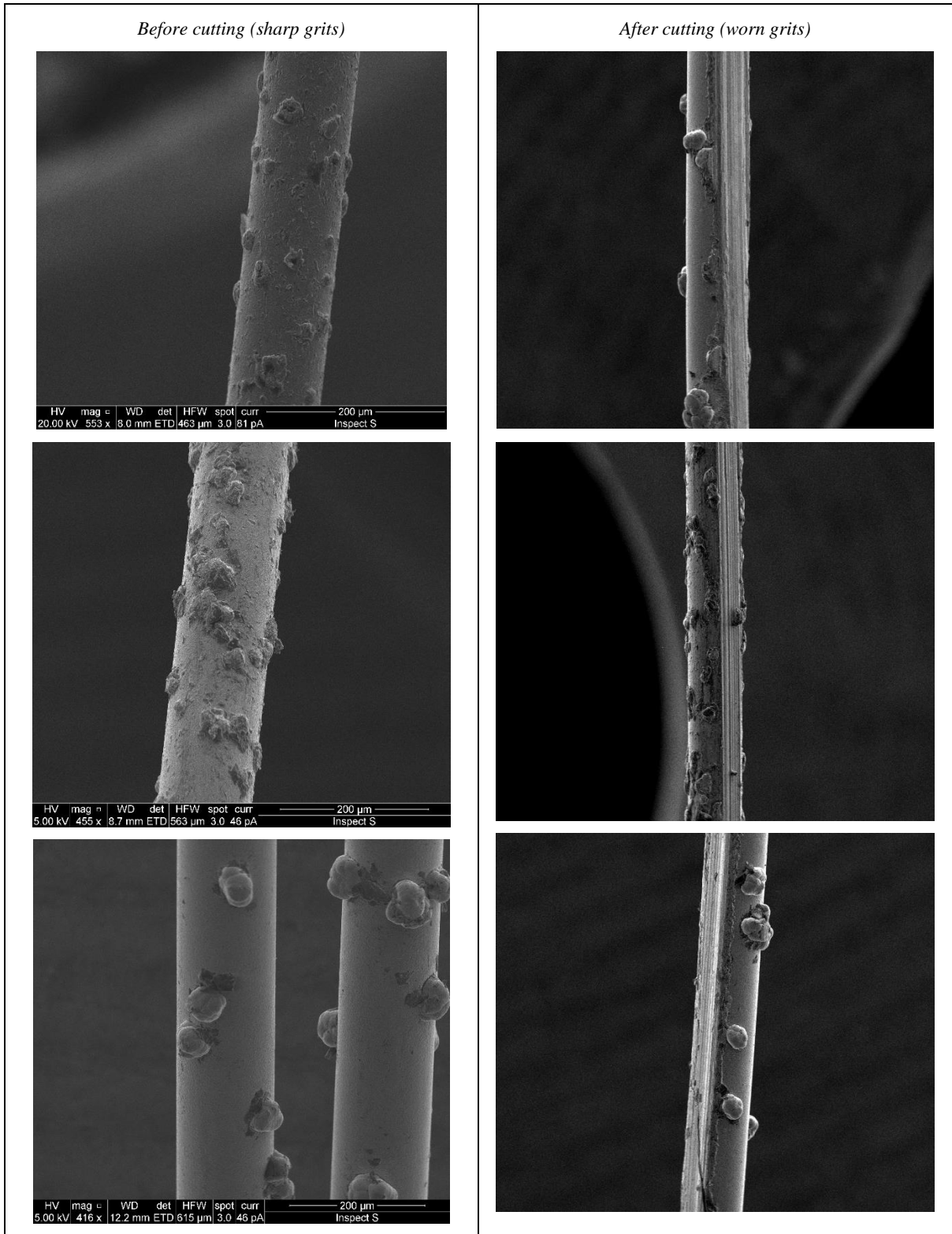


Figure 6-7: SEM images of the wire wear after the cutting tests

### 6.3 Force model validation: experimental and theoretical results comparison

The influence of the grit's shape on the grinding forces was clearly seen on the experimental results discussed previously. This effect was as well highlighted through simulations in chapter 4 and a force model was established. In this section, the modelled force and the experimental measured force in the case of Sapphire cut are compared.

The force model was defined as follow:

$$F = c_0 + 0.0026x^{1.1481}X_1 + 0.0001x^{1.4609}X_2 + 0.019x^{0.3551}X_3 \quad (6-1)$$

This force model was established based on individual grit. Hence, the theoretical total force for the multiple grits cutting case is obtained by multiplying the equation by the number of the grits,  $N$ , involved in the contact area and contributing to the scratching action. In this work,  $N$  is estimated to be equal to 150 grits. Considering  $c_0 = 0$ , which means that the friction force is neglected, the equation is now:

$$F = (0.0026x^{1.1481}X_1 + 0.0001x^{1.4609}X_2 + 0.019x^{0.3551}X_3)N \quad (6-2)$$

Figure 6-8, Figure 6-9, Figure 6-10, Figure 6-11 and Figure 6-12 compare the total force of the modelled and the experimental measured values for the cutting with the abrasives "A", "B", "C", "D" and "E". It can be observed that the experimental values are in the same range and with the same tendency of the modelled values in the five different cases. Increasing depth of cut is resulting in increasing cutting force. However, there is no perfect match between the experimental and the theoretical model values. This is most probably due to the fact that not all shapes are considered in the model; it could be made more realistic by refining the shapes considered and including more geometrical configurations instead of appointing only three geometries. In addition, the error could be as well be related to the fact that friction force was neglected while the real process of grinding is always accompanied with rubbing phase generating friction forces. Moreover, in the simulation model only elastic deformation was considered while in the scratching tests fracture and plastic deformation were observed on the ground surface of the workpiece. This was as well contributed to amplify the error observed between the experimental and the simulation results.

The comparison of the specific cutting force (force over cutting depth), at a 1  $\mu\text{m}$  depth, between the experimental and the simulation values is shown in the Figure 6-13. It can be seen that the values are almost similar in four cutting situations, i.e. in the case of cutting with the abrasives “A”, “B”, “D”, and “E”. However, in the case of cutting with the abrasive “C”, the values in the specific forces show a significant difference. The differences between the experimental and the model values are: 11%, 15%, 69%, 18% and 17% for the five cutting cases “A”, “B”, “C”, “D”, and “E” respectively. In terms of shape, the abrasives sample “C” was containing more sharpest grits compared to the other samples. Furthermore, in real grinding process, the abrasive grits do not have regular shapes and even more their shapes is changing all over the time during the contact with the workpiece due to wear and fracture of the grits. Hence, an abrasive grit could engage into the workpiece with a single edge at the very beginning of the process. But later, due the grain fractures it could start to engage into the workpiece with multi-edges. The sharpest grits are more exposed to fracture and hence for the abrasive sample “C”, the number of the grits engaged into the workpiece and involved in the cutting process becomes higher very quickly after the beginning of the process due to grits fracturing. While in the simulation model, the number of the grits engaged into the workpiece in the contact region was considered constant.

Although the force model is too weak to predict the experimental results, still the comparison at a very shallow depth ( 1  $\mu\text{m}$  ) gives an acceptable prediction of the real data.

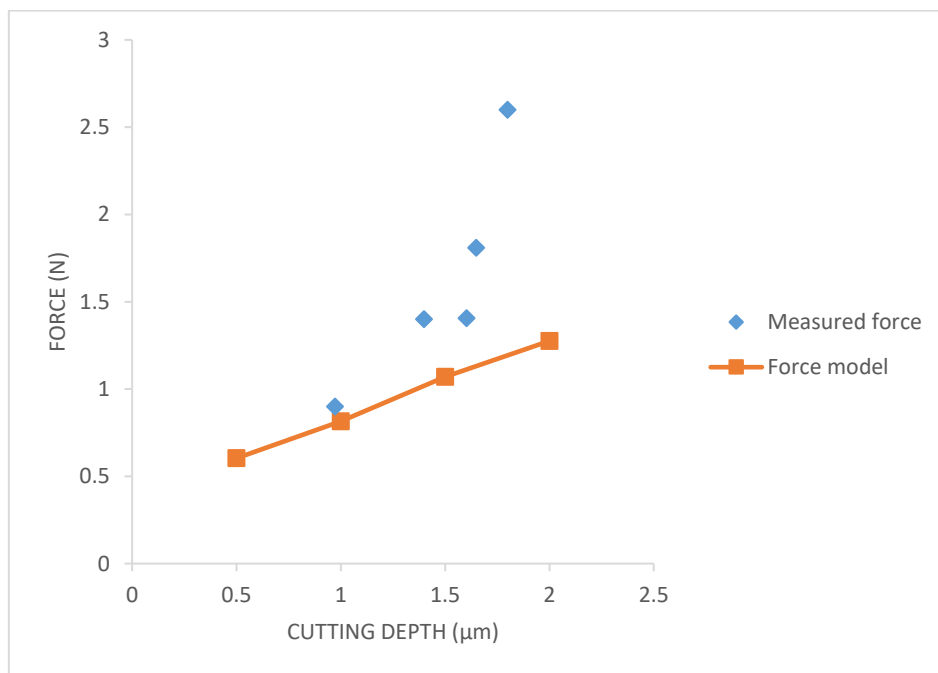


Figure 6-8: Measured and modelled force in the case of cutting with the abrasive A

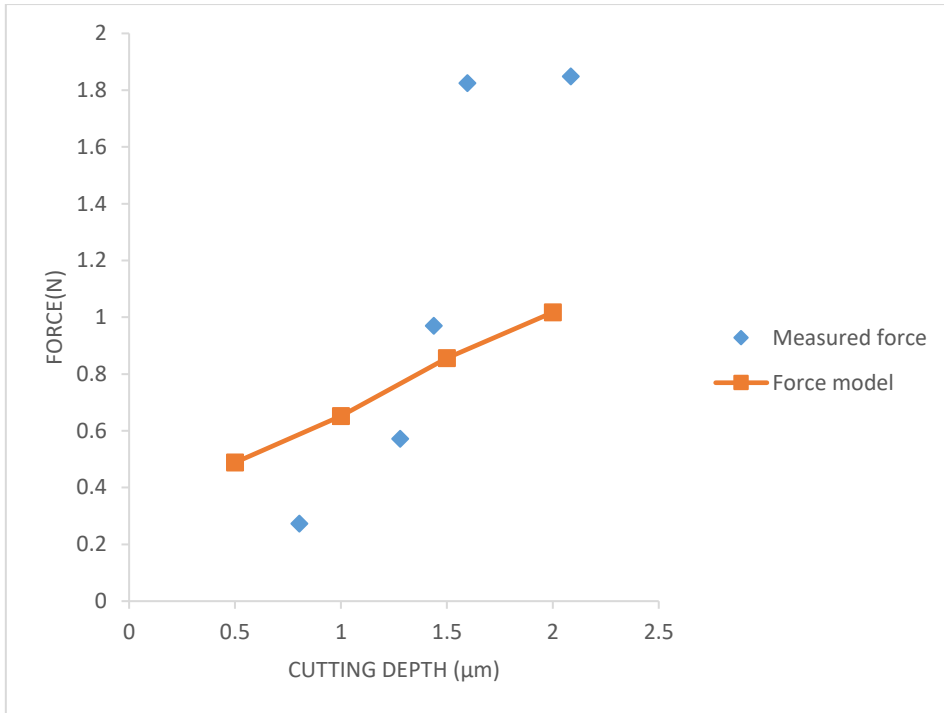


Figure 6-9: Measured and modelled force in the case of cutting with the abrasive B

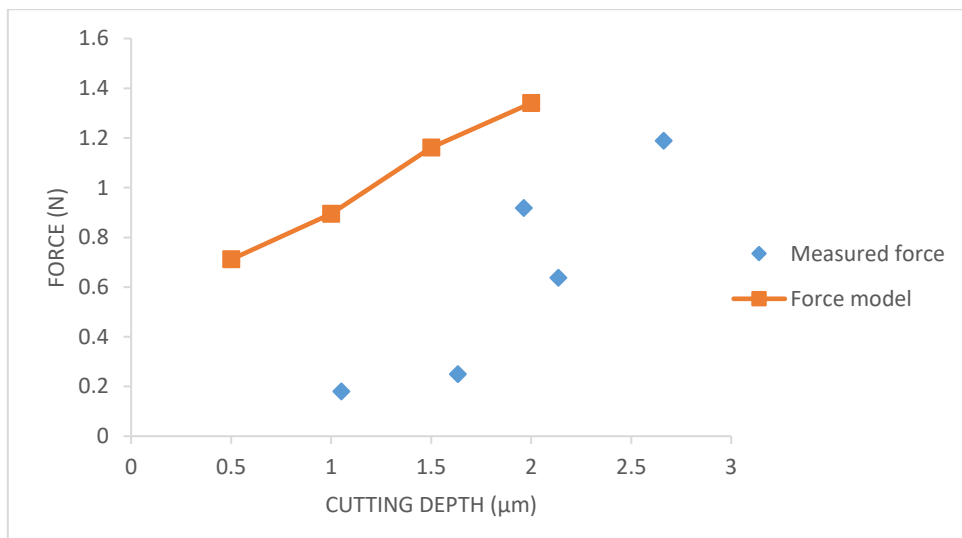


Figure 6-10: Measured and modelled force in the case of cutting with the abrasive C

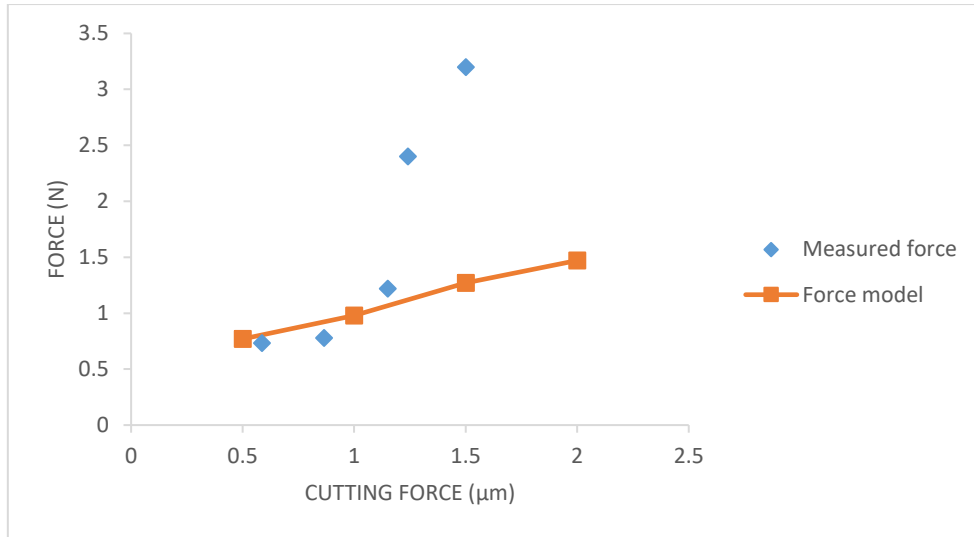


Figure 6-11: Measured and modelled force in the case of cutting with the abrasive D

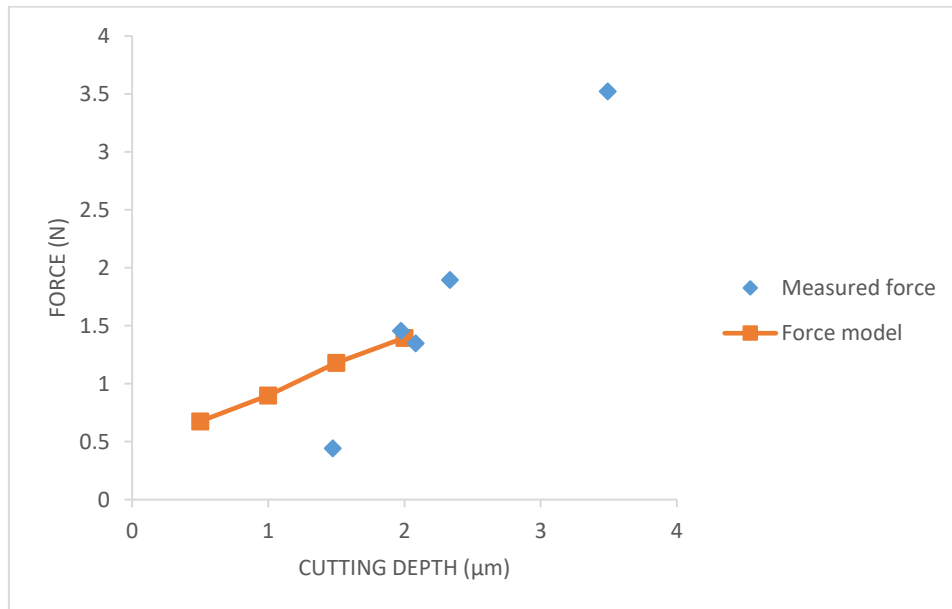


Figure 6-12: Measured and modelled force in the case of cutting with the abrasive E

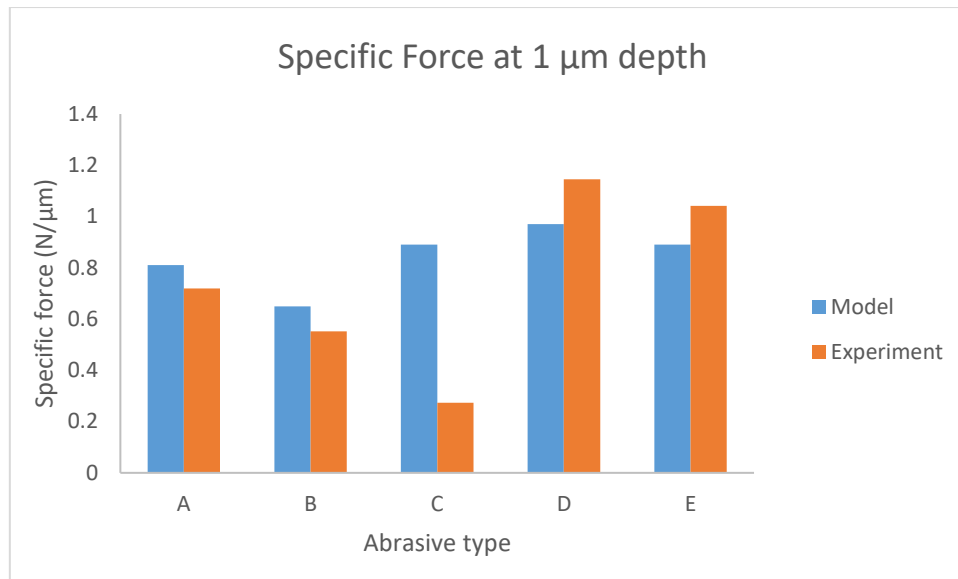


Figure 6-13: Comparison of the specific force at 1 μm depth for the model and the experiment results

## 6.4 Summary

In this chapter, multiple grit grinding and wire saw cutting tests on brittle materials (sapphire and zirconia) show how force and specific force are affected during the cutting process. The influence of the abrasive grit shapes on the force was particularly analysed. It was found that the proportion of different grit shapes has significant influence on grinding force. When the proportion of sharp grits are higher, the grinding forces generated are smaller. However, when the proportion of blunt and flat edge grits are higher, the cutting forces generated are higher. The force model and the experimental results emphasised the importance of taking into consideration the abrasive's shape as a significant parameter that influences the grinding process.

## Chapter 7 Acoustic emission feature extraction and analysis

### 7.1 Introduction

One of the most important signals used in grinding process monitoring has been acoustic emission (AE). In grinding, the AE signal represents many important aspects of grinding, such as: grain and bounding ruptures in the wheel, workpiece chipping, cracks, elastic and plastic deformation, phase transformation, and so on. Thus, AE signal has been used to characterise different physical performances of grinding processes. Most of the studies in grinding process monitoring have used the acoustic emission signal to classify the wear level of the grinding wheel. However, the direct relationship between the acoustic emission and the surface quality of the machined workpiece has been studied to a lesser extent and more research in this field is needed. In this chapter, the objective is to monitor grinding surface creation based on the acoustic emission signal acquired during grinding scratch tests.

To evaluate the acoustic emission signal two signal feature extraction methods were applied, i.e., the time domain analysis (TDA) and the frequency analysis with the fast Fourier transform (FFT). The whole bandwidth of the acoustic emission signal was analysed to determine the frequency ranges with more information correlated with the grinding process.

### 7.2 Methodology

Figure 7-1 shows the methodology applied in this study to determine the optimum signal feature extraction for the monitoring of surface creation in relation to  $W/D$  parameter defined in Chapter 5. The first step (a) involved the application of the TDA and FFT signal processing methods to the acoustic emission signal. The next step (b) was statistical signal characterization by evaluating the features shown in Table 7-1. In step (c), signal feature parameters were correlated with the  $W/D$  parameter using predictive regression models.

$$f(W/D) = \sum_{i=1}^n a_i X_i \quad (7-1)$$

Finally, (d) an exhaustive analysis of the signal feature extraction method was carried out to build and assess the targeted predictive models based on multivariable polynomial regression method, in which the stepwise regression is the core technique. Stepwise regression is a method where predictor variables are entered into the regression equation based upon statistical criteria. At each step in the analysis the predictor variable that contributes the most to the prediction equation are added to the model and the weakest correlated variables are removed.

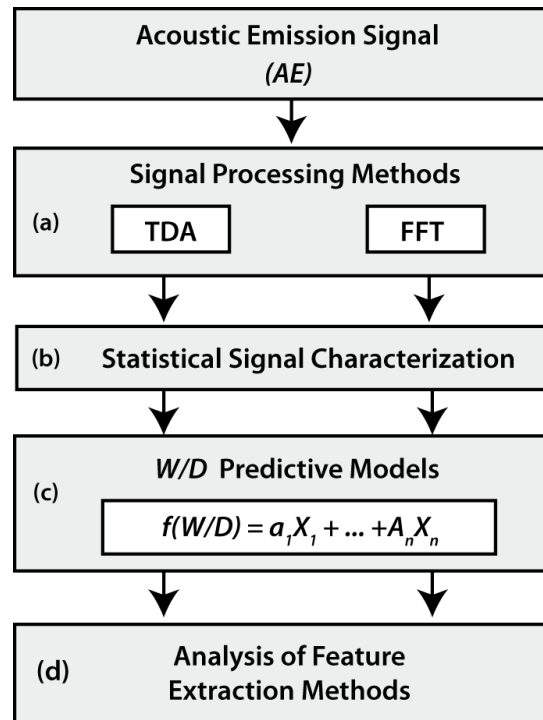


Figure 7-1: AE signal feature extraction methodology

All of the models obtained were diagnosed by analysing atypical values, multicollinearity, independence and normality of the residuals, homoscedasticity, and hypothesis contrast tests. The predictive models were built using stepwise regression method to obtain statistically significant variables at 90 % of confidence (p-value). Proceeding with a stepwise approach, which implies removing variables that are highly insignificant (p-value higher than 10%) and maintaining variable that are showing better statistical performances for these model specifications. Predictive models were assessed in three ways. Firstly, the goodness of fit to experimental data was evaluated using the adjusted determination coefficient (adjusted R-squared,  $R^2_{adj}$ ). Secondly, the sum of squares type III and the p-values [104] were studied in other to determine the variables more correlated with the  $W/D$  parameter. Finally, the goodness of fit was evaluated by the graphical representation of the experimental values of  $W/D$  versus the predicted values with the predictive model.

## 7.3 Results and discussion

### 7.3.1 Time domain analysis (TDA)

The TDA method directly analyses the raw *AE* signals in the time domain, with no transformation or decomposition. This method provides fast signal processing at a low analytical-computational cost, making it suitable for real-time applications. The efficacy of the TDA method mainly depends on the type of the machining process, the registered signal and the process parameter under assessment. On many occasions, working directly with the time signal provides an adequate signal characterization, however, in some cases, this method cannot extract significant distinctive information, which often is hidden or masked in the signal itself. The signal feature extraction using TDA method in this study is based on the parameters shown in Table 7-1.

Table 7-1: statistical feature extraction of acoustic emission signal

<i>FEATURES</i>	<i>TIME DOMAIN</i>	<i>FREQUENCY DOMAIN</i>
<i>Root mean square</i>	<i>RMS</i>	<i>RMS<sub>fi</sub></i>
<i>Standard deviation</i>	<i>SD</i>	<i>SD<sub>fi</sub></i>
<i>Maximum amplitude</i>	-	<i>A<sub>fi</sub></i>
<i>Peak to peak amplitude</i>	<i>PP</i>	-
<i>Kurtosis</i>	<i>K</i>	<i>K<sub>fi</sub></i>
<i>Skewness</i>	<i>S</i>	<i>S<sub>fi</sub></i>
<i>Energy</i>	<i>E</i>	<i>E<sub>fi</sub></i>
<i>Entropy</i>	<i>SE</i>	<i>SE<sub>fi</sub></i>
<i>Mean</i>	<i>X</i>	<i>X<sub>fi</sub></i>
<i>Frequency of maximum</i>	-	<i>F<sub>fi</sub></i>

Where the superscript *fi* indicates the frequency range (*f1*, ..., *fn*)

Considering the models built by the TDA method to estimate *W/D* parameter in relation to *AE* signal features, Table 7-2 depicts the determination coefficient ( $R^2_{adj}$ ) of the regression models, the type III sum of squares [104] and the p-values for the significant characterization parameters. For both sapphire and zirconia materials, it can be observed that the obtained predictive models give very poor results in correlation to the parameter *W/D*. The model for sapphire expressed only 10.6% of the variability of the experimental data, and the model for zirconia expressed the 25.5 %. This implies that the signal feature extraction method in time domain (TDA) failed to achieve an adequate signal characterisation.

Table 7-2: Significant parameters of the sapphire and zirconia predictive models for the TDA method

Sapphire			Zirconia		
$R^2_{adj} = 10.6\%$			$R^2_{adj} = 25.25\%$		
Features	SS Type III	p-Value	Features	SS Type III	p-Value
K	4871	0.018	RMS	1611.5	0.001
Error	31942	-	E	949.6	0.010
-	-	-	Error	5066.6	-

The analysis of the goodness of fit to the experimental data of the TDA method is shown in Figure 7-2, which revealed that the TDA method failed to provide adequate signal feature extraction for the prediction of  $W/D$  parameter.

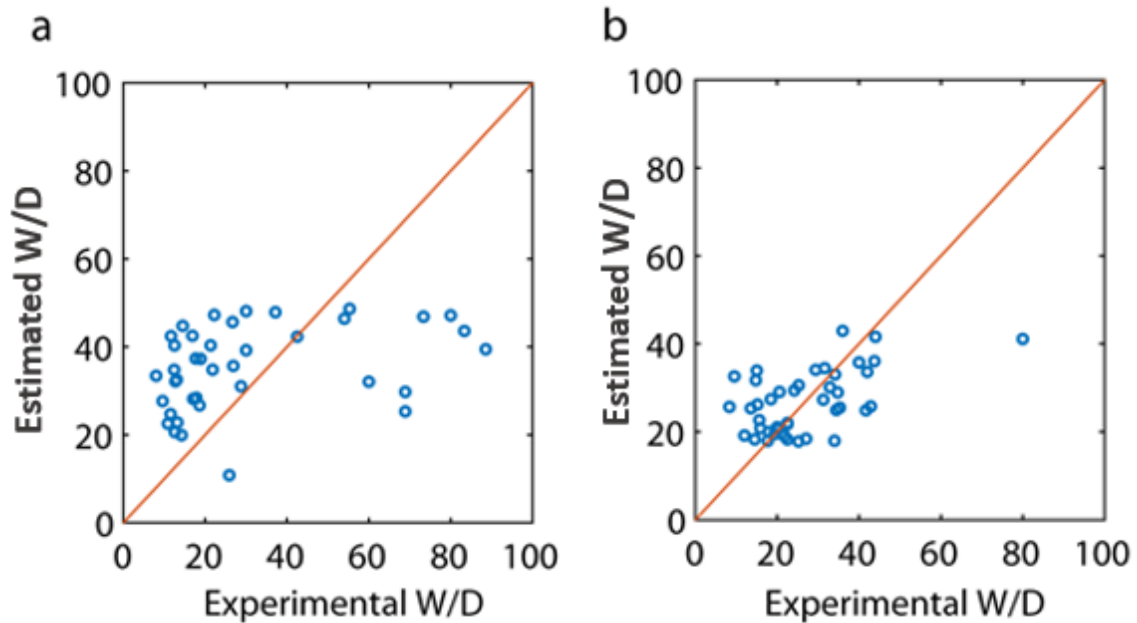


Figure 7-2: Estimated values vs experimental values of the parameter  $W/D$  for TDA method. a) Sapphire, b) Zirconia.

### 7.3.2 Frequency analysis (FFT)

In the machining process monitoring, Fourier transform analysis provides the information of the frequency spectrum of monitored signals. For the succession  $x[i]$  the discrete Fourier transform (DFT) was defined by (7-2):

$$X_k = \sum_{i=0}^{N-1} x_i e^{-j \left( \frac{2\pi ki}{N} \right)}, \quad k = 0, 1, 2, \dots, (N-1) \quad (7-2)$$

The main restriction of (7-2) is its high computational cost, due to the need for the calculus of  $N$  multiplications of the term  $x_i e^{-j(2\pi ki/N)}$  for each of the  $N$  values of  $X_k$ , in other words, this algorithm entails the calculation of approximately  $N^2$ . Thus, for high frequency sample signals, as acoustic emission signal is, the use of this algorithm may not be a suitable processing method. To overcome this drawback, the DFT is implemented by using the algorithm with the highest computational efficiency denominated fast Fourier transform (FFT), which reduces the number of operations to  $N \log_2 N$ .

Typical power spectrums of *AE* signal for both the sapphire and zirconia materials are shown in the top of Figure 7-3 with similar behaviours in all diamond scratch tests. The *AE* spectrum reaches the maximum amplitude at approximately 35 kHz. After that frequency, the power spectrum gradually decreases until around 400 kHz, then, a few feature peaks of power spectrum were found between 450 and 600 kHz.

According to the previous analysis, it can be seen that the relevant spectrum frequency range is around 0-600 kHz. The frequency analysis of *AE* signal was undertaken with a complete analysis of the bandwidth 0-600 kHz (see Figure 7-3). It should be noted, that the total bandwidth under analysis entails certain frequency ranges with significant information failing to be adequately characterized, thus, the bandwidth 0-600 kHz was discretized into six independent frequency ranges of 100 kHz each (Figure 7-3). Secondly, the analysis was focused on the lower frequencies due to the high power spectrum of this area. As shown in Figure 7-4, this analysis was assessed in the frequency range 0-200 kHz. To achieve a precise signal characterization at lower frequencies, each frequency range was fractioned into independent intervals of 10 kHz.

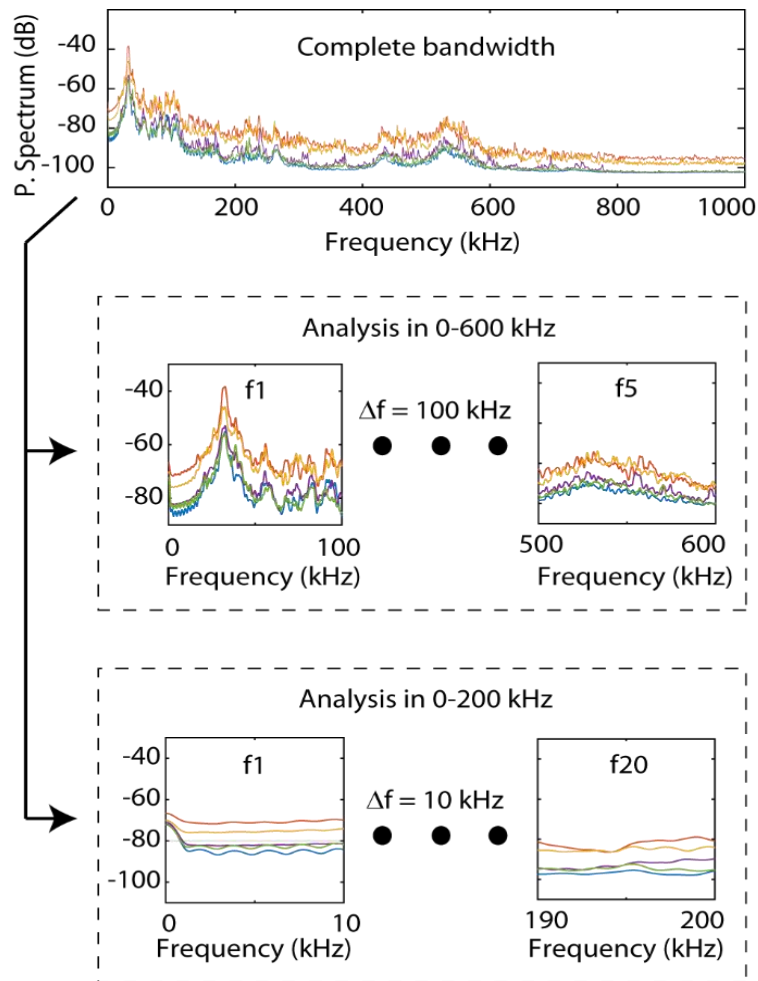


Figure 7-3: Frequency ranges for AE signal analysis

### 7.3.2.1 Analysis of frequency range 0-600 kHz:

The Table 7-3 depicts the results of the regression models for estimating  $W/D$  parameter by the processing of the AE signal in the bandwidth 0-600 kHz with FFT method, for both the sapphire and zirconia materials. Table 7-3 shows the determination coefficient ( $R^2_{adj}$ ), the frequency ranges, the type III sum of squares and the p-values for the significant characterization parameters.

Table 7-3: Significant parameters of the sapphire and zirconia predictive models for the FFT method in 0-600 kHz.

Sapphire			Zirconia		
$R^2_{adj} = 33.62 \%$			$R^2_{adj} = 18.52 \%$		
Features	SS Type III	p-Value	Features	SS Type III	p-Value
$X^{f2}$	1824	0.089	$X^{f1}$	901.6	0,016
$S^{f3}$	6218	0.003	$E^{f5}$	491.2	0.070
$SE^{f3}$	2982	0.031	Error	5522.9	-
$E^{f6}$	5957	0.003	-	-	-
Error	22051	-	-	-	-

As it was mentioned in Table 7-1, the superscript of the features indicates the frequency range of this variable, for example, the feature  $X^{f2}$  indicates the arithmetic mean of the FFT in the frequency range 100-200 kHz. It can be observed that both materials obtained predictive models with very poor results, having little impact on the parameter  $W/D$ . The model for sapphire explained the 33.62% of the variability of the experimental data, and the model for zirconia only the 18.52 %, which indicated a very poor correlation to the  $W/D$  parameter.

The analysis of the goodness of fit to the experimental data of the FFT method in the entire bandwidth is shown in Figure 7-4. The results were quite similar to TDA analysis, where the predictive models for both materials obtained poor results. The model for sapphire overestimated the data in most of the experimental data, and the model for zirconia obtained better results with homogeneous distribution, but with higher deviation in many data. This implies the analysis of the bandwidth 0-600 kHz in intervals of 100 kHz is not effective to extract significative information of  $AE$  signal correlated with  $W/D$  parameter.

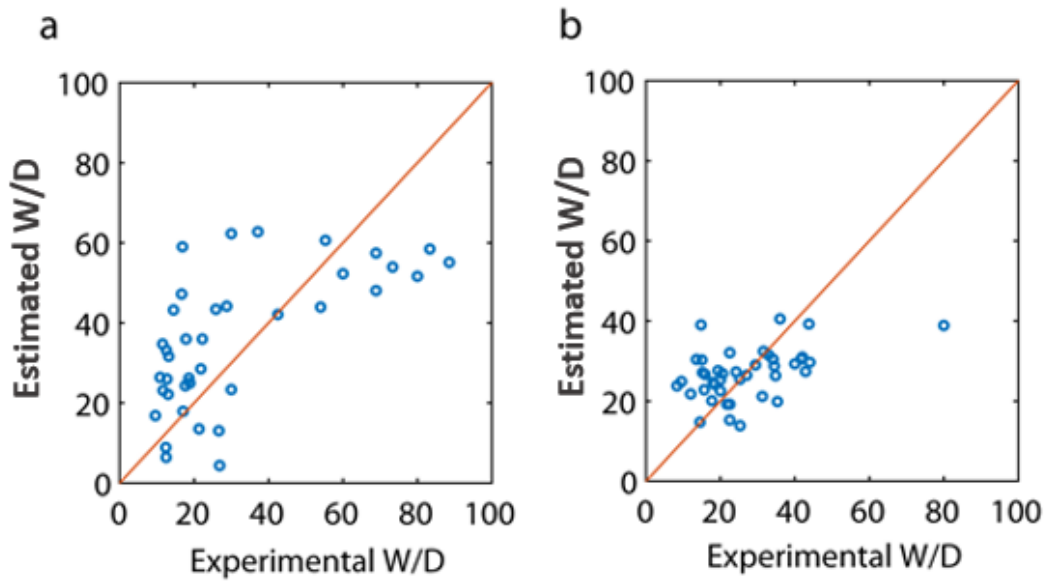


Figure 7-4: Estimated values vs experimental values of the parameter  $W/D$  for FFT method in 0-600 kHz. a) Sapphire, b) Zirconia.

### 7.3.2.2 Analysis of frequency range 0-200kHz:

Table 7-4 shows the significant features for the predictive models obtained in the frequency range 0-200 kHz. It can be observed that the determination coefficient for both models the sapphire and zirconia dramatically increase, with  $R^2_{adj}$  values of 95.84% and 90.07%, respectively. For the sapphire model, a broad number of the analysed frequency bands showed significant information correlated with the parameter  $W/D$ . The ranges  $f_4$  (30-40 kHz) provided the most significant feature of the model ( $A^{f_4}$ ) with the highest sum of square. This frequency range corresponded with the higher power spectrum of the  $AE$  signal. The next frequency bands providing high values of sum of square were in decreasing order  $f_9$  ( $S^{f_9}$ ),  $f_3$  ( $A^{f_3}$ ),  $f_{20}$  ( $SE^{f_{20}}$ ),  $f_{14}$  ( $K^{f_{14}}$ ),  $f_{16}$  ( $SE^{f_{16}}$ ). The rest of significant frequency ranges also provided information but to a lesser extent. For the model of zirconia, similar to sapphire, a broad number of the analysed frequency ranges provided information correlated with the  $W/D$  parameter. However, in contrast with the model for sapphire, higher differences in the sum of squares of the significant features were not found for zirconia; the maximum difference is reached in the range  $f_{16}$  ( $F^{f_{16}}$ ), with a value slightly higher than in the rest of the variables.

Table 7-4: Significant parameters of the sapphire and zirconia predictive models for the FFT method in 0-200 kHz.

Sapphire			Zirconia		
$R^2_{adj} = 95.48 \%$			$R^2_{adj} = 90.07 \%$		
Feat.	SS Type III	p-Value	Feat.	SS Type III	p-Value
$A^{f3}$	8779.6	0.000	$K^{f1}$	556.9	0.000
$S^{f3}$	876.8	0.000	$SE^{f2}$	166.3	0.005
$A^{f4}$	10797.7	0.000	$S^{f5}$	221.6	0.001
$X^{f5}$	302.9	0.011	$K^{f6}$	353.6	0.000
$A^{f6}$	2754.1	0.000	$F^{f6}$	169.7	0.004
$F^{f6}$	4189.0	0.000	$E^{f9}$	389.0	0.000
$SD^{f8}$	2140.2	0.000	$SD^{f10}$	493.6	0.000
$S^{f9}$	9021.8	0.000	$RMS^{f14}$	655.5	0.000
$K^{f11}$	3324.4	0.000	$X^{f14}$	922.0	0.000
$K^{f13}$	2149.6	0.000	$K^{f15}$	491.3	0.000
$K^{f14}$	6879.5	0.000	$F^{f15}$	176.4	0.004
$SE^{f16}$	5887.5	0.000	$F^{f16}$	1472.2	0.000
$A^{f17}$	883.9	0.000	$SD^{f19}$	824.3	0.000
$E^{f18}$	214.2	0.030	$A^{f20}$	366.8	0.000
$F^{f18}$	1570.6	0.000	$X^{f20}$	787.2	0.000
$SE^{f20}$	7163.6	0.000	$F^{f20}$	804.8	0.000
Error	1013.6	-	Error	431.6	-

The analysis of the correlations of the estimated data versus the experimental data for the FFT method in the 0-200 kHz frequency band (Figure 7-5) revealed the model for zirconia had an even distribution in all of the  $W/D$  parameter ranges, with no bias and a very strong correlation. The model obtained for sapphire, in spite of having higher determination coefficient than zirconia model, showed a higher deviation in all of the frequency ranges with under-estimation of  $W/D$  values between 10 and 20.

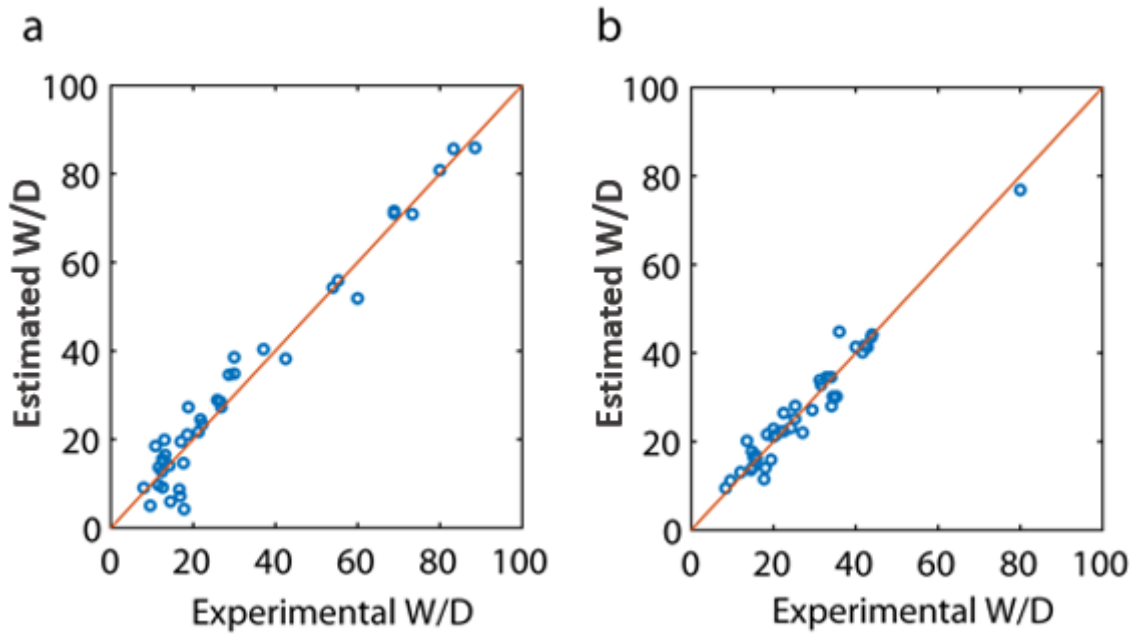


Figure 7-5: Estimated values vs experimental values of the parameter W/D for FFT method in 0-200 kHz. a) Sapphire. b) Zirconia.

According to the previous analysis, the bandwidth 0-200 kHz discretized in intervals of 10 kHz was the best methodology to obtain an optimal acoustic emission signal characterisation. This method provided an optimal correlation between the acoustic emission signal and the W/D parameter for both materials.

Finally, the AE signal in frequency domain is providing useful information for monitoring the surface creation in abrasive scratch experiment. The models with good correlation with W/D that could present abrasives form such as blunt or sharp, which could provide a good measure foundation for grinding wheel performance monitoring.

## 7.4 Summary

The online grinding surface creation monitoring was carried out by processing the acoustic emission signals in abrasive scratch experiments. The surface creation in each scratch was assessed by using the ratio Width/Depth (W/D) of the scratch profile of maximum depth.

The TDA signal processing method failed to obtain applicable signal feature extraction for both materials. For the FFT signal processing method, the analysis of different frequency ranges with suitable selection of the bandwidth is crucial to achieve an optimal signal feature extraction that could be able to correlate the acoustic emission signals with the ratio W/D. The analysis of the frequency range of 0-600 kHz did not provide good results due to the length of

the discretisation intervals (100 kHz) were too long, and the information of the AE signal could not be analysed adequately, leaving the significant information hidden in the signal appearance. The best bandwidth for acoustic emission signal relevant feature extraction was obtained at 0-200 kHz. The frequency range discretisation with intervals of 10 kHz enabled the isolation and location of signal ranges with effective information for the monitoring of the W/D parameter. Most of the 20 frequency intervals analysed in the bandwidth 0-200 kHz have a great impact indication on the W/D parameter.

## Chapter 8 Conclusion, recommendations and future work

### 8.1 Conclusion

A feasible classification method is proposed to enable the size and shape distribution of abrasives to be standardised for grinding dynamics analysis and simulation, which is beneficial to grinding performance prediction. By means of conducting microscopy measurement tests, an initial investigation was carried out on nine diamond loose abrasive samples followed by five types of bonded abrasive grits assessment in terms of the aspect ratio of width to length of the samples, the size distribution and the dominant shapes. It is found that only a few types of grit morphologic geometries dominate the grit population. A simplified geometrical model of the abrasive grits is then proposed based on these dominant geometries. The effect of grit shape on the cutting force was investigated experimentally on brittle materials (sapphire and zirconia) by means of scratching tests. Furthermore, online grinding surface creation monitoring was carried out by processing the acoustic emission signals in the abrasive scratch experiments.

The following conclusions are drawn from this research study.

- After the analysis of current methods used in abrasive machining research, it is suggested that the analysis of abrasive processing should focus on a set of dominant grit shapes rather than just single simplified geometry.
- These dominant shapes are ellipsoid, sphere, quadrilateral frustrum, quadrilateral pyramid and tetrahedron pyramid.
- To simplify the force modelling, only most typical grit cutting situations are analysed in considering their stress and strain condition. The common grit shape, sharp and blunt cutting edges are considered as key scenario and mimicked as round, pyramid and truncated pyramid.
- A simplified geometrical model of the abrasive grits is then proposed based on these dominant geometries.
- Through FEM simulations, it was found that the grit shape has a great impact on the cutting forces and the stress distribution on the surface contact region of the workpiece. The forces were the lowest in the case of the grit of a sharp pyramidal shape, while they are the highest in the case of the grit of a truncated pyramidal shape. Furthermore, a force model associating the cutting force and the shape proportion of the abrasives was established.

- By means of scratching tests, the effect of grit shape on the cutting force was investigated. It was concluded that the grit shape is an influential parameter. The proportion of different grit shapes has significant influence on grinding force. When the grits are sharper, the grinding forces are smaller. However, when the grits are blunt with flat or rounded edges, the cutting forces are higher.
- The force model and the experimental results emphasised the importance of taking into consideration the abrasive's shape as a significant parameter that influences the grinding process in general and particularly the grinding forces. This study will help in the design of optimized grinding wheels with regards to the topography and the grits morphology.
- By processing the acoustic emission signals in the abrasive scratch tests, the surface creation in each scratch was assessed by using the ratio width over depth,  $W/D$ , of the scratch profile. The TDA signal processing method failed to obtain applicable signal feature extraction. For the FFT signal processing method, the best bandwidth for acoustic emission signal relevant feature extraction was obtained at 0-200 kHz. The frequency range discretisation with intervals of 10 kHz enabled the isolation and location of signal ranges with effective information for the monitoring of the  $W/D$  parameter.

## 8.2 Contribution to knowledge

Throughout this thesis, the main achievements and main contribution to the knowledge are summarised here in bellow:

- Abrasive shape assessments: a set of new knowledge of micron diamond abrasives in terms of their shape was set up. Complex shapes that are difficult to characterise were assessed through image analysis and a shape classification of the abrasive grits is suggested focusing on a set of dominant shapes. Hence, an initial classification of 21 different shapes was established and then the classification was narrowed into only 5 to 6 dominants.
- A feasible test rig for multiple grits scratching tests was developed as well as a test rig for diamond wire saw.
- Force model: Based on the proportion of the dominant shapes in an abrasive sample a relationship was found linking the cutting force to the abrasive's shape and where the wight of different shapes on the force was emphasised.
- Acoustic emission: The acoustic emission signal in frequency domain has proven to be an applicable signal to monitor the surface creation in abrasive scratch experiments.

### **8.3 Recommendations and future work**

The study on the abrasive's assessment showed a lot of interesting facts. There are many ways to obtain information and data about grits, even for really fine grains able to reach 5  $\mu\text{m}$ . However, manual measurement of the shape and morphology of abrasive grits requires a lot of time to analyse a great number of grits and also introduces a subjectivity in the measures, for example when it comes to choosing a shape for a certain grit. Automation of the morphology measurements of abrasive grits is recommended as a next step that may solve the problem, by developing a program, which calculates and returns the morphology and various shape factors of a great number of grits.

The theoretical model proposed in this study takes into consideration only three main grit shapes; all dominated shape should be considered in the model to improve the model accuracy. This may help to get a better match between the simulation and the experimental tests results. Finally, monitoring the surface creation by acoustic emission could be extended for industrial applications in the grinding process.

## References

- [1] Metal Cutting Corporation, [Online]. Available: <https://learn.metalcutting.com/guides/precision-metal-grinding-finishing-touch-small-metal-parts>.
- [2] S. Kalpakjian, Manufacturing engineering and technology, Pearson, 2006.
- [3] K.-H. M. M. K. F. W. M. Brakhage, "Grinding wheel modeling: Development of a mathematical model," *MASCOT Proceedings-IMACS Series in Computational and Applied Mathematics*, 2013.
- [4] S. Kalpakjian, MANUFACTURING ENGINEERING AND TECHNOLOGY, Pearson, 2006.
- [5] S.F. Krar, A.F. Gill and P. Smid, Technology of Machine Tools, New York: Tata McGraw-Hill, 2008.
- [6] M.J. Jackson and B. Mills, "Materials Selection Applied to Vitrified Alumina & cBN Grinding Wheels," *Journals of Materials Processing Technology*, vol. 108, 2000.
- [7] M.P Hitchiner, S.B McSpadden and J.A Webster, "Evaluation of factors controlling CBN abrasive selection for vitrified bonded wheels," *Annals-Manufacturing Technology*, vol. 54, pp. 277-280, 2005.

- [8] M. S. Ranjan and C. Shankar, "Grinding Wheel Abrasive Material Selection Using Fuzzy TOPSIS Method," *Materials and Manufacturing Processes*, vol. 28, no. 4, 2013.
- [9] D. ZHANG, C. LI, D. JIA and Y. ZHANG, "Investigation into engineering ceramics grinding mechanism and the influential factors of the grinding force," pp. 19-34, 2014.
- [10] X. JING, S. MAITI and G. SUBHASH, "A new analytical model for estimation of scratch-induced damage in brittle solids," *Journal of the American Ceramic Society*, pp. 885-892, 2007.
- [11] Z. Li, F. ZHANG and X. LUO, "A new grinding force model for micro grinding RB-SiC ceramic with grinding wheel topography as an input," *Micromachines*, 2018.
- [12] M. SHAVVA and S. GRUBIY, "Cutting Forces Calculation at Diamond Grinding Of Brittle," *Applied Mechanics and Materials*, pp. 163-168, 2015.
- [13] X. Chen, "Machining Dynamics in Grinding Processes," in *Machining Dynamics. Springer Series in Advanced Manufacturing*, Springer, London, 2009.
- [14] K. Ono, "Analysis on the grinding force," *Bulletin of the Japan Society of Grinding Engineers*, pp. 19-22, 1961.
- [15] L. Li and J. Fu, "The analysis of grinding force mathematical model".
- [16] S. Malkin, "The wear of grinding wheels," vol. 93, no. 4.

- [17] Swanson, P. A. and Vetter, A. F., "The Measurement of Abrasive Particle Shape and Its Effect on Wear," vol. 28, no. 2, pp. 225-230, 1985.
- [18] Pellegrin, Dennis and Stachowiak, Gwidon, "Assessing the role of particle shape and scale in abrasion using 'sharpness analysis' Part II. Technique evaluation," vol. 253, 2002.
- [19] Pellegrin, Dennis, Corbin, Normand, Baldoni, Gary and Torrance, A.A., "Diamond particle shape: Its measurement and influence in abrasive wear," vol. 42, 2009.
- [20] I. D. Marinescu, M. Hitchiner, E. Uhlmann, W. B. Rowe and I. Inasaki, *Handbook of Machining with Grinding Wheels*, CRC Press, 2006.
- [21] D. V. De Pellegrin and G. W. Stachowiak, "Evaluating the Role of Particle Distribution and Shape in Two-Body Abrasion by Statistical Simulation," vol. 37, no. 3, pp. 255-270, 2004.
- [22] A. Torrance, "An explanation of the hardness differential needed for abrasion," vol. 68, 1981.
- [23] S. P.A. and V. A.F., "The measurement of abrasive particle shape and its effect on wear," vol. 28, 1985.
- [24] A. W. Momber and R. Kovacevic, "Classification and Characterization of Abrasive Materials," in *Principles of Abrasive Water Jet Machining*, Springer-Verlag London Limited, 1998.

- [25] D. Doman, A. Warkentin and R. Bauer, "A survey of recent grinding wheel topography models," Vols. 343-352, no. 46, 2006.
- [26] A. Darafon, A. Warkentin and R. Bauer, "3D metal removal simulation to determine uncut chip thickness, contact length and surface finish in grinding," *Int. J. Adv Manuf Technol*, no. 66, pp. 6-12, 2013.
- [27] M. Rasim, P. Mattfeld and F. Klocke, "Analysis of the grain shape influence on the chip formation in grinding," *Journal of Materials Processing Technology*, no. 226, pp. 60-68, 2015.
- [28] J. J. Coronado, "Effect of Abrasive Size on Wear," in *Abrasion Resistance of Materials*, In-Tech Publishers, 2012.
- [29] K. Aydiner, G. Aydın and I. Karakurt, "Effect of the abrasive grain size on the cutting performance of concrete in AWJ technology," *Technology*, vol. 13, no. 03, pp. 145-150, 2010.
- [30] A. C. Sparavigna, "The Invention of Carborundum, the Synthetic Silicon Carbide," Philica, 2018.
- [31] American National Standard Institute, "Procedure for Bulk Density of Abrasive Grain," 1992.
- [32] santo-abrasives.com, "Abeasive grain/ Grit size," [Online]. Available: <https://santo-abrasives.com/abrasive-grade-grit-size>.

- [33] S. Kröner and M.T. Doménech-Carbó, “Determination of minimum pixel resolution for shape analysis: proposal of a new data validation method for computerized images,” 2013.
- [34] W.J. Head and M.E. Harr, “The development of a model to predict the erosion of materials by natural contaminants,” vol. 15.
- [35] G. Petasyuk, “A system–analogue method of identification of geometric shape of the abrasive grain projection,” p. 277–287, 2016.
- [36] M.A. Verspui, P. van der Velden, G. de With and P.J. Slikkerveer, “Angularity determination of abrasive powders,” pp. 122-126, 1996.
- [37] G. S. D.V. De Pellegrin, “A new technique for measuring particle angularity using cone fit analysis,” pp. 109-119, 2001.
- [38] AZO Materials, “Particle Shape Characterization for Abrasives Manufacturers,” [Online]. Available: <https://www.azom.com/article.aspx?ArticleID=2811>.
- [39] R.S. Hahn , “On the mechanics of the grinding process under plunge cutconditions,” pp. 72-80, 1966.
- [40] T. T. Ö. Xun Chen, “Process Monitoring and Metrology for Single Grit Grinding Test Performance,” *Proceedings of the 17th International Conference on Automation & Computing*, 2011.

- [41] NIE Zhen-guo, WANG Gang, JIANG Feng and LIN Yong-lian, "Investigation of modeling on single grit grinding for martensitic stainless steel," *J. Cent. South Univ*, 2018.
- [42] Lin Tian, Yucan Fu, Jiuhua Xu, Haiyan Li and Wenfeng , "The influence of speed on material removal mechanism in high speed grinding with single grit," *International Journal of Machine Tools & Manufacture*, 2014.
- [43] T.-J. Chuang , S. Jahanmir and H.C. Tang, "inite element simulation of straight plunge grinding for advanced ceramics," pp. 1723-1733, 2003.
- [44] S. t. r. a. f. y. operation. [Online]. Available: <https://www.thefabricator.com/article/cuttingweldprep/selecting-the-right-abrasives-for-your-operation>.
- [45] Hockenull, B. S, Kopalinsky, E. M and Oxley, O. M., "Mechanical wear models for metallic surfaces in sliding contact," *Journal of Physics D: Applied Physics*, vol. 25, no. 01, 2000.
- [46] W. Lortz, "A model of the cutting mechanism in grinding," *Wear*, vol. 53, no. 01, pp. 115-128, 1979.
- [47] ASM International, "Brittle Materials: Principles," in *Metallographic Polishing*, [asminternational.org](http://asminternational.org), 2003.

- [48] Z. W. Zhong, "Ductile or Partial Ductile Mode Machining of Brittle Materials," vol. 21, no. 1, 2003.
- [49] E. K. AntwiKui and L. H. Wang, "A review on ductile mode cutting of brittle materials," vol. 13, no. 02, 2018.
- [50] B. W. Darvell, "Mechanical Testing," vol. 10, no. 01, 2018.
- [51] T. R. Shearer, "Grinding Brittle Materials," Aggressive Grinding Service, Inc, 2013.
- [52] Y. Ebina, W. Hang, L. Zhou, J. Shimizu, O. Teppey and H. Ojima, "Study on grinding processing of sapphire wafer," *Advanced Materials Research*, vol. 565, no. 22, pp. 22-27, 2012.
- [53] L. Xu and G. H. He, "Research on the Precision Grinding Process of Sapphire Lens," 2010.
- [54] S. P. Anand, N. Arunachala and L. Vijayaragh, "Study on grinding of pre-sintered zirconia using diamond wheel," *Materials and Manufacturing Processes*, vol. 33, no. 06, pp. 634-643, 2018.
- [55] M. R. I. a. S. T. Gaobo Xiao, "A Study of Mechanics in Brittle–Ductile Cutting Mode Transition," vol. 9, no. 49, 2018.

- [56] K. L. H. W. Elijah Kwabena ANTWI, “A review on ductile mode cutting of brittle materials,” vol. 13, no. 2.
- [57] E. Brinksmeier, J.C. Aurich, E. Govekar, C. Heinzl, H.W. Hoffmeister, F. Klocke, J. Peters, D. Rentsch , D.J. Stephenson, E. Ulmann, K. Weinert and M. Wittmann, “Advanced in Modeling and Simulation of Grinding Processes,” vol. 55, pp. 667-696, 2006.
- [58] A.O. Oluwajobi and X. Chen, “The fundamentals of modelling abrasive machining using molecular dynamics,” pp. 354-381, 2010.
- [59] Y. W. J. L. Q. Z. Jianguo Cao, “Study on the material removal process in ultrasonic-assisted grinding of SiC ceramics using smooth particle hydrodynamic (SPH) method,” vol. International Journal of Advanced Manufure Technology, 2016.
- [60] K. S. Vijay Kumar Mishra, “Empirical estimation of grinding specific forces and energy based on a modified Werner grinding model,” vol. 14th CIRP Conference on Modeling of Machining Operations, 2013.
- [61] J.M. Challen and P.L.B. Oxley, “An explanation of the different regimes of friction and wear using asperity deformation models,” pp. 229-243, 1978.
- [62] J.M. Challen and P.L.B. Oxley, “An Explanation for the Different Regimes of Friction and Wear Using Asperity Deformation Models,” vol. 53, pp. 229-243, 1979.

- [63] W. B. Rowe, *Principles of Modern Grinding Technology*, Elsevier Inc., 2nd Edition • 2014.
- [64] A.A. Torrance and T.R. Buckley, “A slip-line field model of abrasive wear,” *Wear* , pp. 35-45, 1995.
- [65] D. L. Logan, *A first course in the finite element method*, Brooks/Cole, 2002.
- [66] Y. U. Xiaolin, “Finite Element Analysis of Influence of Grinding Parameters on Grinding Force,” *International Conference on Electronic & Mechanical Engineering and Information Technology*, 2011.
- [67] Jianbo Dai, Honghua Su, Wenbo Zhou, Tengfei Yu, Wenfeng Ding, Quanli Zhang and Yihao Zheng, “Finite Element Implementation of the tension-shear coupled fracture criterion for numerical simulations of brittle-ductile transition in silicon carbide ceramic grinding,” *International Journal of Mechanical Sciences*, 2018.
- [68] Erhan Kayabasi, Savas Ozturk , Erdal Celik and Huseyin Kurt, “Determination of cutting parameters for silicon wafer with diamonds wire saw using an artificial neural network,” 2017.
- [69] Zi-Yu Zhanga, Bing Xiaoa, Duan-Zhi Duanb, Bo Wanga and Si-Xing Liuc, “Investigation on the brazing mechanism and machining performance of diamond wire saw based on Cu-Sn-Ti alloy,” in *International Journal of Refractory Metals & Hard Materials*, 2017.

- [70] Hsu, Ajay Gupta, Chao-Chang , A. Chen and Hsien-Wei, “Study on diamond wire wear, surface quality, and subsurface damage during multi-wire slicing of c-plane sapphire wafer,” in *The International Journal of Advanced Manufacturing Technology*, 2019.
- [71] S. C. Jain and S. S. Rathore, “Prediction of Cutting Performance of Diamond Wire Saw Machine in Quarrying of Marble: A Neural Network Approach,” 2011.
- [72] N. Ghaysari, M. Ataei, F. Sereshki and R. Mikaiel, “prediction of performance of diamond wire saw with respect to texture characteristics of rock,” 2012.
- [73] Shujuan Li, Jiabin Wang and Aofei Tang, “Force modeling of silicon monocrystal wire saw machining,” 2016.
- [74] Hardin and Craig William, “Fixed abrasive diamond wire saw slicing of single crystal sic wafers and wood,” 2003.
- [75] Ningchang Wang, Feng Jiang and Xipeng Xu, “Research on the machinability of A-plane sapphire under diamond wire sawing in different sawing directions,” 2019.
- [76] H. Wu, “Wire sawing technology: A state-of-the-art-review,” 2016.
- [77] Arkadeep Kumar, Steffi Kaminski, Shreyes N. Melkote and Chris Arcona, “Effect of wear of diamond wire on surface morphology, roughness,” 2016.

- [78] C. H. Lauro, L. C. Brandão, D. Baldo and R. A. Reis , “Monitoring and processing signal applied in machining processes - A review,” *Meas. J. Int. Meas. Confed.*, vol. 58, p. 73–86, 2014.
- [79] R. Teti, K. Jemielniak, G. O’Donnell and D. Dornf, “Advanced monitoring of machining operations,” *CIRP Ann. - Manuf. Technol*, vol. 59, p. 717–739, 2010.
- [80] A. Boaron and W. L. Weingaertner, “Dynamic in-process characterization method based on acoustic emission for topographic assessment of conventional grinding wheels,” *Wear*, 2018.
- [81] A. Arun, K. Rameshkumar, D. Unnikrishnan and A. Sumesh, “Tool Condition Monitoring of Cylindrical Grinding Process Using Acoustic Emission Sensor,” in *Materials Today: Proceedings*, 2018.
- [82] M. Siddhpura and R. Paurobally, “A review of chatter vibration research in turning,” *Int. J. Mach. Tools Manuf*, vol. 61, p. 27–47, 2012.
- [83] E. García Plaza, P. J. Núñez López and E. M. Beam, “Multi-sensor data fusion for real-time surface quality control in automated machining systems,” vol. 18, 2018.
- [84] E. García Plaza and P. J. Núñez López, “Application of the wavelet packet transform to vibration signals for surface roughness monitoring in CNC turning operations,” *Mech. Syst. Signal Process*, vol. 98, p. 902–919, 2018.

- [85] S. Karam and R. Teti, "Wavelet transform feature extraction for chip form recognition during carbon steel turning," vol. 12, p. 97–102, 2013.
- [86] Q. Liu, X. Chen and N. Gindy, "Investigation of acoustic emission signals under a simulative environment of grinding burn," *Int. J. Mach. Tools Manuf*, 2006.
- [87] Q. Liu, X. Chen and N. Gindy, "Fuzzy pattern recognition of AE signals for grinding burn," 2005.
- [88] E. García Plaza and P. J. Núñez López, "Surface roughness monitoring by singular spectrum analysis of vibration signals," vol. 84, 2017.
- [89] T. W. Liao, C. F. Ting, J. Qu and P. J. Blau, "A wavelet-based methodology for grinding wheel condition monitoring," 2007.
- [90] E. García Plaza and P. J. Núñez López, "Analysis of cutting force signals by wavelet packet transform for surface roughness monitoring in CNC turning," vol. 98, 2018.
- [91] K. Wegener, H. W. Hoffmeister, B. Karpuschewski, F. Kuster, W. C. Hahmann and M. Rabiey, "Conditioning and monitoring of grinding wheels," vol. 60, 2011.
- [92] D. T. Nguyen, S. Yin, Q. Tang, P. X. Son and L. A. Duc, "Online monitoring of surface roughness and grinding wheel wear when grinding Ti-6Al-4V titanium alloy using ANFIS-GPR hybrid algorithm and Taguchi analysis," vol. 55, 2018.

- [93] J. Tang, J. Du and Y. Chen, “Modeling and experimental study of grinding forces in surface grinding,” vol. 209, 2009.
- [94] D. E. Lee, I. Hwang, C. M. O. Valente, J. F. G. Oliveira and D. A. Dornfeld, “Precision manufacturing process monitoring with acoustic emission,” vol. 46, p. 176–188, 2006.
- [95] T. W. Liao, “Feature extraction and selection from acoustic emission signals with an application in grinding wheel condition monitoring,” 2010.
- [96] N. H. Chiu and Y. Y. Guao, “State classification of CBN grinding with support vector machine,” vol. 201, p. 601–605, 2008.
- [97] E. A. Dias, F. B. Pereira, S. L. M. Ribeiro Filho and L. C. Brandão, “Monitoring of through-feed centreless grinding processes with acoustic emission signals,” 2016.
- [98] Kröner, S, and , “Determination of minimum pixel resolution for shape analysis: proposal of a new data validation method for computerized images,” *Powder Technol*, vol. 245, p. 297–313, 2013.
- [99] Leica application suite (LAS), “handbook,” 2010. [Online]. Available: <http://www.leicamicrosystems.com>.
- [100] L. A. Blunt and X. Jiang, *Advanced Techniques for Assessment Surface topography: Development of a Basis for 3D Surface Texture Standards*, “ Surfstand.”London ; Sterling, VA: Kogan Page Science, 2003.

- [101] T. Soong, *Probability and Statistics for Engineers and Scientists*, Chichester: John Wiley&Sons, 2004.
- [102] N. V. Baidakova and T. N. Orlova, "Influence of Abrasive Grain Geometrical Characteristics on the Grinding Quality," vol. 206, 2017.
- [103] Savvides, N. and Bell, T.J., "Hardness and elastic modulus of diamond and diamond-like carbon films," vol. 228, 1993.
- [104] G. E. P. Box, J. S. Hunter and W. G. Hunter, *Statistics for experimenters : design, innovation, and discovery*, Wiley-Interscience, 2005.
- [105] S. Black, *Principles of engineering manufacture*, Halsted Press, 1996.
- [106] B. S. Linke, "A review on properties of abrasive grits and grit selection," *International Journal of Abrasive Technology*, vol. 07, no. 01, pp. 46-58, 2015.
- [107] M. Lianjie, Y. Aibing, W. Jia, L. Chen and W. Fengwen, "Finite element simulation of grinding performance and grain shapes in grinding superalloy-inconel," 2015.
- [108] F. Podczeczek, "A shape factor to assess the shape of particles using image analysis," vol. 93, no. 1, pp. 47-53, 1997.
- [109] D. E. Lee, I. Hwang, C. M. O. Valente and J. F. G. Ol, "Precision manufacturing process monitoring with acoustic emission," vol. 46 pp, no. 2, p. 176–188, 2006.

- [110] W. E. Keck, "Process of separating valuable materials from grinding dusts and sludges". U.S. Patent US45100042A, 1947.
- [111] The-Crankshaft Publishing, "FEM for Beams," [Online]. Available: <http://what-when-how.com/the-finite-element-method/fem-for-beams-finite-element-method-part-2/>. [Accessed 2019].
- [112] M. Wu, N. D. Corbin, S. E. Fox, T. Ellingson and L. A. Carman, "High permeability grinding wheels". United States Patent 5,738,697, 1998.
- [113] M. R. Cox and M. Budhu, "A practical approach to grain shape quantification," *Engineering Geology*, vol. 96, pp. 1-16, 2008.
- [114] M. Rasim, P. Mattfeld and F. Klocke, "Analysis of the grain shape influence on the chip formation in grinding," *Journal of Materials Processing Technology*, vol. 226, pp. 60-68, 2015.
- [115] C. Sun, S. Xiu, Qingliang Li, Jingyu Wang and Yu Zhao, "Research on the embossment phenomenon of disc grinding by workpiece's removal rate," *Archives of civil and mechanical engineering*, 2019.
- [116] L. Cao, "Research on Cutting Technology of Underwater Diamond Wire Saw," 2008.
- [117] M.J. Jackson and B. Mills, "Materials selection applied to vitrified alumina and CBN grinding wheels," *Journal of Materials Processing Technology*, vol. 108, 2000.

- [118] P. Werner and T. Tawakoli, "Advance in high efficiency deep grinding," 1988.
- [119] J. Russ, The Image Processing Handbook, 2nd ed., CRC Press.
- [120] Metal Cutting Corporation, 19 February 2019. [Online]. Available: <https://learn.metalcutting.com/guides/precision-metal-grinding-finishing-touch-small-metal-parts>. [Accessed 19 October 2019].
- [121] C. G. S. Malkin, "Thermal Analysis of Grinding," vol. 56, no. 2, 2007.
- [122] I. D. M. Guoxu Yin, "A Heat Transfer Model of Grinding Process Based on Energy Partition Analysis and Grinding Fluid Cooling Application," 2017.
- [123] R. D. L. Vijayaraghavan, "Theoretical analysis of thermal profile and heat transfer in grinding," vol. 8, no. 1, 2013.

## Appendixes

### Appendix – A: Leica microscope



## Appendix – B: Diamond wire saw test rig drawing

ITEM NO.	PART NUMBER	DESCRIPTION	QTY.
1	base		1
2	adaptive plate		1
3	chuck		1
4	Female flange		1
5	male flange		1
6	motor		1
7	Bearing base		1
8	bearing base support		1
9	2721T3		2
10	motor_base		1
11	Sample		1
12	v_frame_tige		4
13	h_frame_tigel		2
14	h_frame_tige2		2
15	guide pine		1
16	wire holder		1
17	B18.2.3.2M - Formed hexscrew, M10x1.5x30 --30WN		1
18	B18.2.2M - Plain washer, 10 mm, wide		1
19	dynamometre		1
20	bolt		1
21	312x1.00	Lee Spring LE-031 D8	1
22	threaded bar		1
23	pulley_tige		1
24	pulley		2
25	traverse		2
26	v_wire		1
27	B18.2.2M - Plain washer, 12 mm, narrow		2
28	B18.2.3.2M - Formed hexscrew, M12x1.75x90 --30WN		2
29	WeightWire		1
30	BalanceWeight		1
31	B18.2.4.6M - Heavy hex nut, M12x1.75 --WN		1
32	TensionWheel		2
33	TensionWheelPin		2
34	DiamondWire		1
35	BS EN ISO - 4161 - M20 - N		1
36	bush		1
37	BushHolder		1
38	BushHolderColumn		1
39	B18.3.1M - 12 x 1.75 x 65 Hex SHCS -- 36NHX		2
40	Rectangular section spring washer BS 4464 - 12 (Type B)		2
41	B18.2.3.9M - Heavy hex flange screw, M14 x 2.0 x 40 --40N		2
42	B18.2.2M - Plain washer, 14 mm, regular		2
43	B18.2.4.1M - Hex nut, Style 1, M4 x 0.7 --D-N		8
44	AM B18.6.7M 4x25-23.6-N		4
45	AM B18.6.7M 4x16-14.6-N		4

**Technical Drawing: Diamond saw test rig**

**Dimensions:**  
 - Motor assembly width: 410  
 - Total rig width: 948.23  
 - Rig height: 790

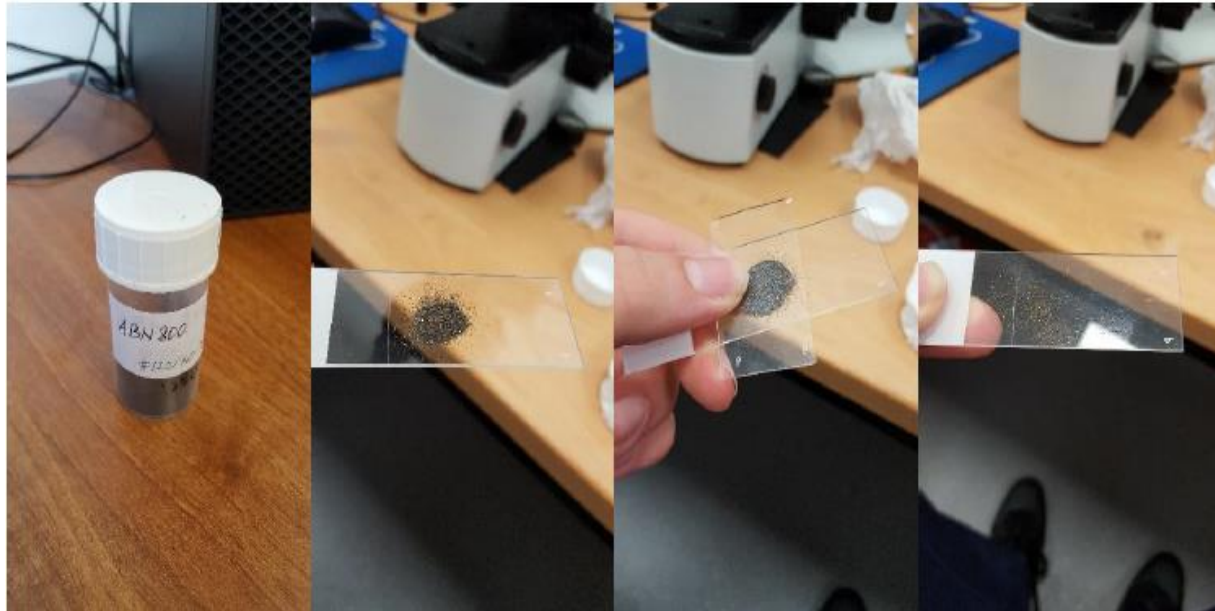
**Callouts:** 1, 2, 3, 4, 5, 6, 7, 8, 10, 11, 12, 14, 15, 16, 21, 23, 24, 25, 26, 28, 29, 30, 31, 32, 33, 35, 36, 37, 38, 41, 42, 43, 44, 45

**Title Block:**  
 DIAMOND SAW TEST RIG  
 DRAWN BY: [ ]  
 CHECKED BY: [ ]  
 DATE: [ ]  
 SCALE: 1:1  
 SHEET 1 OF 1

### Appendix – C.1: Samples of the loose abrasives



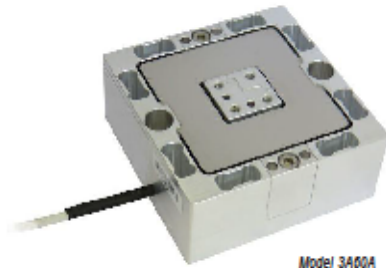
### Appendix – C.2: Preparation of the loose abrasives for measurements



## Appendix – D.1: Interface’s 3A60A 3-Axis Load Cell

**The Leader in Force Measurement**

**interface**  
ADVANCED FORCE MEASUREMENT



Model 3A60A

### Model 3A Series 3-Axis Load Cell

- 3-Axis – Fx Fy Fz; Independent Bridges
- 20N to 500kN Force Range
- Compact Size
- Low Crosstalk
- Temperature Compensated

Interface’s 3-axis load cell measures forces simultaneously in 3 mutually perpendicular axes: X, Y, and Z - tension and compression. Each axis provides a unique mV/V output and requires no mathematical manipulation. The 3-axis load cell is built to minimize eccentric loading effects and crosstalk between axes.

The 3A Series 3-axis load cell is ideally suited to many industrial and scientific applications, such as aerospace, robotics, automotive and medical research (orthopaedics and biomechanical).

The load cell is provided in various capacity ranges and sizes with each of the three axes providing the same capacity.

We are happy to work with your design needs – providing a custom design if warranted for varying capacities (between X-Y and Z), higher temperature capability, or OEM/private labelling if needed.

### Accessories

BSC4A 4-Channel Analog Amplifier

BSC4D 4-Channel USB Digital Amplifier

### Capacity Comparison

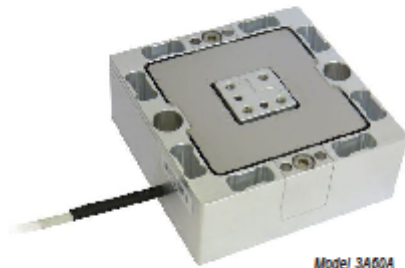
Model	Capacity (N)	Material
3A60a	20	Aluminum
	50	
	100	
	200	Stainless
	500	
3A120	50	Aluminum
	100	
	200	
	500	
	1K	
	1K	Stainless
	2K	
3A160	5K	Nickel Plated Steel
	2K	
	10K	
	20K	
	50K	
3A300	50K	Nickel Plated Steel
	100K	
	200K	
3A400	500K	Nickel Plated Steel

### Wiring

	Description	Wire Color	37-PIN D-Sub	16-PIN M23
Shield	Shield	Shield	1	N/C
X-Axis	+ Excitation	Brown	20	2
	- Excitation	White	27	1
	+ Output	Green	22	3
	- Output	Yellow	25	4
Y-Axis	+ Excitation	Pink	2	6
	- Excitation	Gray	9	5
	+ Output	Blue	4	7
	- Output	Red	7	8
Z-Axis	+ Excitation	Purple	11	10
	- Excitation	Black	18	9
	+ Output	Orange	13	11
	- Output	Transparent	16	12
3A60A	+ Output	Gray/Pink	13	11
	- Output	Red/Blue	16	12
3A120, 3A160, 3A300, & 3A400	+ Output	Gray/Pink	13	11
	- Output	Red/Blue	16	12

**interface**  
ADVANCED FORCE MEASUREMENT

Interface Force Measurements Ltd. • Unit 19 Wellington Business Pk, Dukes Ride, Crowthorne, Berkshire RG45 6LS UK  
• Phone: +44 (0)1344 776666 • Fax: +44(0)1344 774765 • E-mail: [Info@interface.uk.com](mailto:Info@interface.uk.com) • [www.interfaceforce.com](http://www.interfaceforce.com) •

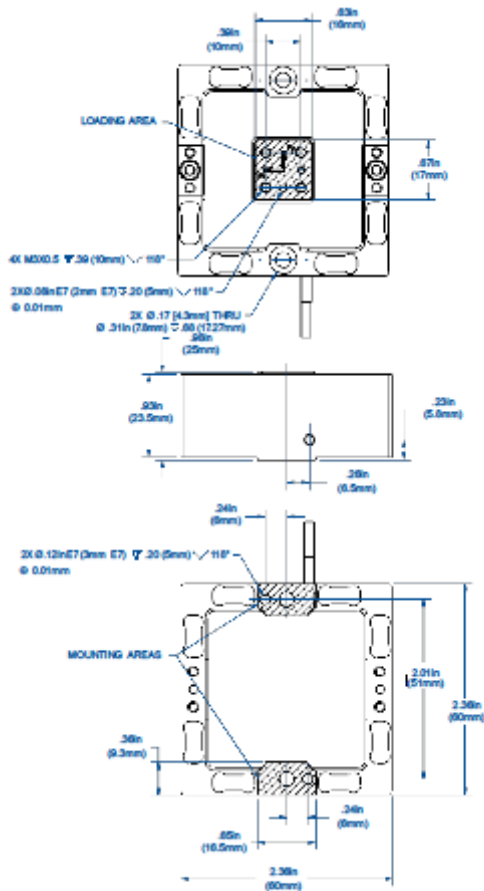


Model 3A60A

### Model 3A60A 3-Axis Load Cell

The 3A60A is a new and improved version of the original 3A60 with revised mounting holes and extended capacity ranges. The 3A60A is NOT backward compatible with the old 3A60.

#### Dimensions

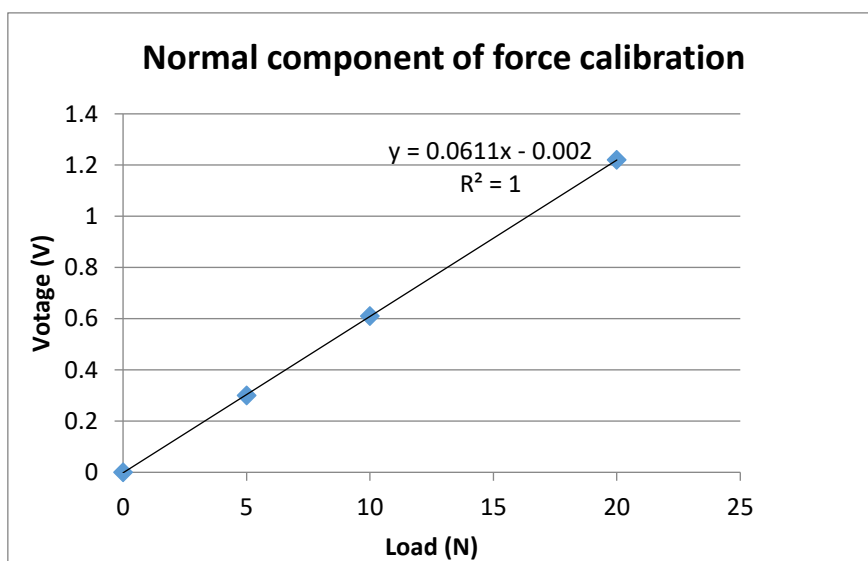
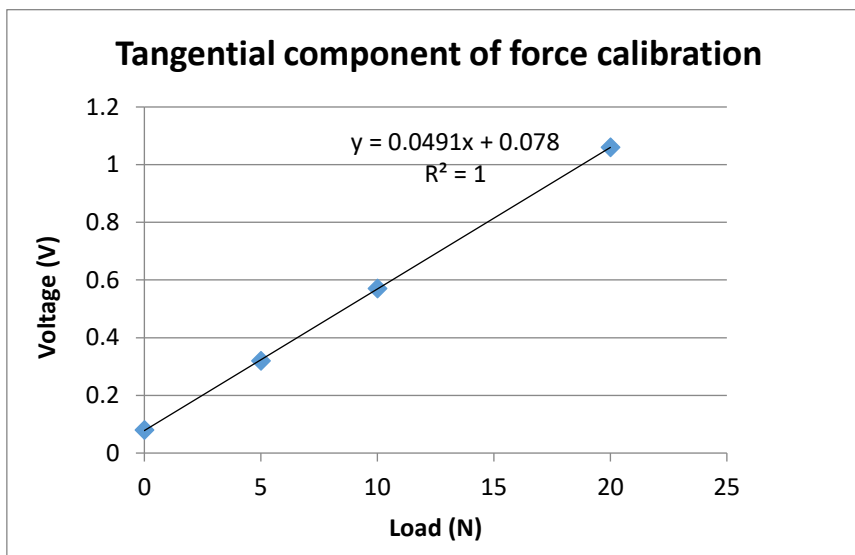
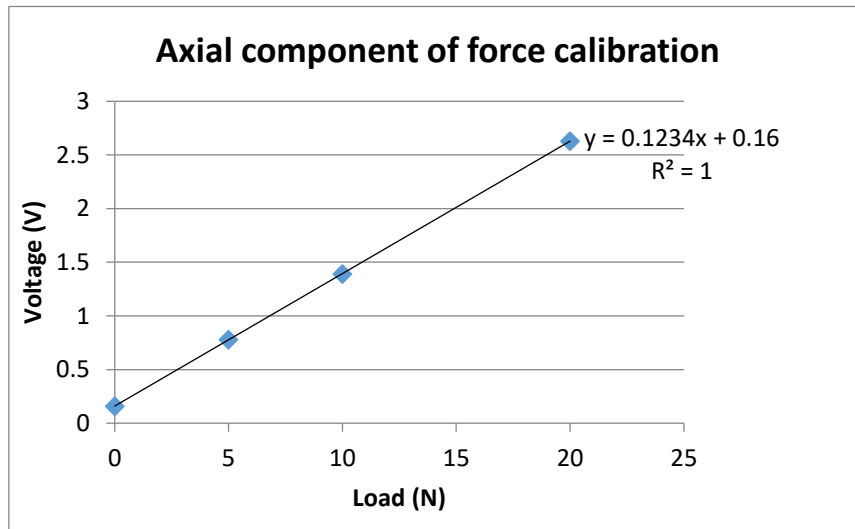


#### Specifications

ACCURACY (Max. Error*)		
Nonlinearity - %FS	±0.2	
Hysteresis - %FS	±0.02	
Creep (30 min) - %	±0.1	
MECHANICAL DATA		
Rated Capacity (FS) - N	10	20 50 100 200 500
Material	Aluminum	Stainless
Deflection - Fx, Fy - mm	0.1	
Deflection - Fz - mm	0.15	
Total Weight - kg	.110	0.2
Safe Overload - %RO	150	
Ultimate Overload - %RO	300	
Protection Level	IP 54	
ELECTRICAL DATA		
Rated Output (Nom.) - mV/V	±0.5	
Max. Excitation Voltage - V	10	
Zero balance - mW/V	0.1	
Input resistance, x/y axis - Ω	395 ±5	375 ±5
Output resistance, z axis - Ω	355 ±5	
Insulation Resistance - Ω	> 5 × 10 <sup>9</sup>	
Electrical Connection	3m Cable with 37-PIN Connector. Includes Mate	
TEMPERATURE		
Operating Range - °C	-10 to 85	
Compensated Range - °C	-10 to 70	
Effect on zero - %RO / °C	± 0.02	
Effect on output - % / °C	± 0.02	
ECCENTRICITY AND MOMENT*		
Allowable moment - Nm	5	10
Crosstalk: xy / yx - %	± 2	
Crosstalk: zx/y - %	± 2	
Crosstalk: x/y/z - %	± 2	
Eccentric Load Sensitivity - %FS @ 20mm	± 1	

\*Nominal

## Appendix – D.2: Interface’s 3A60A 3-Axis Load Cell calibration



## Appendix – D.2: Honeywell S beam load cell

**Honeywell**

### **Model 127**

#### **Load Cell**



#### **DESCRIPTION**

The Model 127 load cells combines both a compact form and high precision to offer a superior tension force transducer. The one-piece S-shaped design achieves a maximum non-linearity of 0.03 % full scale for load ranges of 50 kg and 100 kg.

#### **FEATURES**

- 50 kg, 100 kg range
- $\pm 0.03$  % FS accuracy
- Built-in overload resistance
- One-piece, nickel-plated alloy steel construction
- Integral cable
- Cost efficient

# Model 127

## PERFORMANCE SPECIFICATIONS

Characteristic	Measure
Load ranges <sup>2</sup>	50 kg, 100 kg
Accuracy	±0.03 % full scale
Output	3.0 mV/V
Creep (max.)	±0.03 % full scale (30 minutes)

## ENVIRONMENTAL SPECIFICATIONS

Characteristic	Measure
Temperature, operating	-30 °C to 70 °C [-22 °F to 158 °F]
Temperature, compensated	-20 °C to 55 °C [-4 °F to 131 °F]
Temperature effect, zero	±0.03 % full scale/10 °C
Temperature effect, span	±0.03 % full scale/10 °C
Protection class	IP67

## ELECTRICAL SPECIFICATIONS

Characteristic	Measure
Strain gage type	Bonded foil
Excitation (acceptable)	10 Vdc to 12 Vdc
Excitation (max.)	15 Vdc
Insulation resistance	≥ 5000 mOhm
Bridge resistance (tolerance) - Input resistance	400 ohm ±10 ohm (nominal)
Bridge resistance (tolerance) - Output resistance	352 ohm ±2 ohm (nominal)
Zero balance (tolerance)	±1 % full scale
Electrical termination (std)	5 m [16.40 ft] flying leads

## MECHANICAL SPECIFICATIONS

Characteristic	Measure
Maximum allowable load	150 % full scale <sup>1</sup>
Material	Nickel plated alloy steel

## WIRING CODES

Cable	
Red	(+) supply
Black	(-) supply
Green	(+) output
White	(-) output
Large Black	Shield

## RANGE CODES

Range codes	Range
LF	50 kg
LH	100 kg

## MOUNTING DIMENSIONS

